REFERENCE ONLY

UNIVERSITY OF LONDON THESIS

Degree PhD Year 2006 Name of Author HUNG-O

CHAOTIC ~~HAMILTONIAN~~ QUANTUM RATCHETS AND FILTERS WITH COLD ATOMS IN OPTICAL LATTICES: PROPERTIES OF FLOQUET STATES

Gwang-ok Hur

A thesis submitted to
THE UNIVERSITY OF LONDON
for the degree of
DOCTOR OF PHILOSOPHY

University College London

July 2005

ProQuest LLC
789 East Eisenhower Parkway
P.O. Box 1346
Ann Arbor, MI 48106-1346

We are designed to explore.

ABSTRACT

The δ-kicked rotor is a paradigm of quantum chaos. Its realisation with clouds of cold atoms in pulsed optical lattices demonstrated the well-known quantum chaos phenomenon of 'dynamical localisation'. In those experiments by several groups world-wide, the δ-kicks were applied at equal time intervals. However, recent theoretical and experimental work by the cold atom group at UCL [Monteiro *et al* 2002, Jonckheere *et al* 2003, Jones *et al* 2004] showed that novel quantum and classical dynamics arises if the atomic cloud is pulsed with repeating sequences of unequally spaced kicks. In Monteiro *et al* 2002 it was found that the energy absorption rates depend on the momentum of the atoms relative to the optical lattice; hence a type of chaotic ratchet was proposed. In Jonckheere *et al* and Jones *et al*, a possible mechanism for selecting atoms according to their momenta (velocity filter) was investigated.

The aim of this thesis was to study the properties of the underlying eigenvalues and eigenstates. Despite the unequally-spaced kicks, these systems are still time-periodic, so we in fact investigated the Floquet states, which are eigenstates of $U(T)$, the one-period time evolution operator. The Floquet states and corresponding eigenvalues were obtained by diagonalising a matrix representation of the operator $U(T)$.

It was found that the form of the eigenstates enables us to analyse qualitatively the atomic momentum probability distributions, $N(p)$ measured experimentally. In particular, the momentum width of the individual eigenstates varies strongly with $< p >$ as expected from the theoretical and ex-

perimental results obtained previously. In addition, at specific $< p >$ close to values which in the experiment yield directed motion (ratchet transport), the probability distribution of the individual Floquet states is asymmetric, mirroring the asymmetric $N(p)$ measured in clouds of cesium atoms.

In the penultimate chapter, the spectral fluctuations (eigenvalue statistics) are investigated for one particular system, the double-delta kicked rotor. We computed Nearest Neighbour Spacing (NNS) distributions as well as the number variances (Σ_2 statistics). We find that even in regimes where the corresponding classical dynamics are fully chaotic, the statistics are, unexpectedly, intermediate between fully chaotic (GOE) and fully regular (Poisson). It is argued that they are analogous to the critical statistics seen in the Anderson metal-insulator transition.

ACKNOWLEDGEMENTS

As the completion of my PhD has finally come to an end, I would like to thank my supervisor, Prof. Tania Monteiro, for her valuable guidance and support. I would also like to thank Dr. Charles Creffield for helpful discussions and comments regarding my thesis.

I thank Dr. Thibaut Jonckheere for such a great attitude and patience in the discussions during which I gained much knowledge about coding and quantum mechanics. Although it was short period of time, it was the right time when I needed it the most. I also thank Dr. Roman Tolchenov for helping me with the coding. He is such an excellent programmer and saved a great mount of time in my PhD. I also thank Mischa Stocklin and Dr. Phil Jones in the Laser Cooling group for their collaboration. I would like to thank all members of the TAMPA group, especially colleagues in the room, A7, where I have been working. I thank to Dr. Nicholas Grindle for proofreading my thesis.

I thank my friends who I have met in London for helping me to escape from loneliness. I thank all my friends in Korea who constantly encouraged me to carry on and not to give up. Especially, I thank Dr. Sung Woo Kim for his treatment and support since I came to London. My most special thanks goes to my mother for her constant prayer and encouragement over the phone. Without them, I could not have got through all the way to this moment.

CONTENTS

List of Figures

List of Tables

CHAPTER 1

Introduction

The roots of chaos theory go back to about 1900. It first appeared when Henri Poincaré was trying to solve the so-called three-body problem, three astronomical bodies under mutual gravitational attraction. He could not find an analytic solution so, instead, he plotted the orbits in phase space. His examination of the trajectories led to the discovery of chaos. Following the discovery, some studies on the topic of nonlinear dynamics were carried out by many scientists, for example, the three body problem by Birkhoff, turbulence and astronomical problems by Kolmogorov and radio engineering by Cartwright and Littlewood. However, the study of chaos theory involves nontrivial computer work requiring huge CPU for repeating calculation of simple mathematical formulae.

Rapid progress in chaos theory was made from the mid 1950's, when computers with large capacity became available. Thanks to fast calculations by computers another major work was achieved by Edward Lorenz. While he was running his weather simulation, he made a surprising discovery that

small changes in initial conditions produced large changes in the long term outcome, which is now called the 'butterfly effect'.

1.1 Classical and quantum chaos

1.1.1 Classical chaos

As mentioned above, classical chaos is very sensitive to initial conditions, hence the long time dynamics is unpredictable. Chaotic phenomena in the macroscopic world have been observed in many areas, such as pendulums, the growth of populations and planetary dynamics. The classical dynamics of chaotic systems can be investigated by using deterministic equations of motion.

For Hamiltonian systems, the equations of motion of a particle with position coordinates q_i and momentum coordinates p_i can be expressed by:

$$\begin{aligned} \dot{q}_i &= \frac{\partial H}{\partial p_i} \\ \dot{p}_i &= -\frac{\partial H}{\partial q_i} \end{aligned} \tag{1.1}$$

for $1 \leq i \leq d$, where d is the number of degrees of freedom and H is the Hamiltonian function.

Classical Hamiltonian dynamics can be split into two limiting forms: the regular motion of integrable systems and the irregular motion of chaotic systems (there can be a intermediate system with mixed phase space). The primary example of the integrable motion is the harmonic oscillator, while a periodically driven pendulum can display chaotic motion. The behaviour of a classical system can be distinguished in terms of trajectories: in the chaotic case, two neighbouring trajectories diverge exponentially with time.

The rate of divergence is the Lyapunov exponent λ, i.e. the distance between trajectories increases as $e^{\lambda t}$.

1.1.2 Quantum chaos

In general, the study of quantum mechanical systems, whose counter-parts are classically chaotic is termed 'quantum chaos'. In other words, quantum chaos is the subject of how chaos in classical systems manifests itself in quantum systems.

In studies of the transition between regular and (classically) chaotic system, the Kolmogorov-Arnold-Moser(KAM) theorem specifies how a typical regular system becomes chaotic when a perturbation is introduced (more details follow). On the other hand, quantum chaos is concerned with establishing the relation between chaotic systems and quantum systems, according to Bohr's correspondence principle: classical mechanics must be contained in quantum mechanics in the limit where the de Broglie wavelength ($\lambda = \frac{h}{p}$, where h and p are the Planck constant and momentum respectively) is very small, $< 1\mathring{A}$ (or, equivalently, in the limit of $\hbar \to 0$). However, as far as a trajectory is concerned, in quantum mechanics, the uncertainty principle, $\Delta x \Delta p \geq \frac{1}{2}\hbar$, implies that one cannot associate a single particle classical trajectory with the motion of a quantum particle. Furthermore, if a wave packet is constructed with the eigenfunctions of a time independent Hamiltonian, i.e. by a superposition of eigenfunctions, it shows quasi-periodic behaviour (if the spectrum is discrete), unlike the classical case. After a certain time, known as 'break time', the quantum dynamics shows quasi-periodicity.

Hence, in contrast to classical chaos, quantum mechanically irregular motion cannot be characterised by extreme sensitivity to tiny changes of initial

condition. Due to the unitarity of quantum mechanics (the evolution operator $U(t',t)$ is a linear unitary operator), the overlap of two wave functions remains time independent, i.e. $|<\phi(t')|\psi(t')>|^2 = |<\phi(t)|\psi(t)>|^2$ under the same Hamiltonian for wave function ϕ and ψ.

However, there are certain quantum phenomena which appear only if the corresponding classical counterpart is chaotic, for example, the statistical properties of the quantum spectra. The statistics of energy levels are typically described by random matrix theory when the classical counterpart is chaotic, while it shows a Poissonian statistics when the classical dynamics is regular, i.e. completely integrable. For classically integrable systems, energy levels tend to cluster. The typical distribution of the spacings of neighbouring levels follows an exponential form, $P(s) = \exp(-s)$. The levels behave as if they are uncorrelated. However, for classically non-integrable systems with chaotic phase space the energy levels are correlated and crossings are strongly resisted. There are three universal degrees of level repulsions: linear, quadratic and quartic ($P(s) \sim s^\beta$ for $s \to 0$ with β=1,2 or 4) depending on their symmetries. Briefly, systems with time reversal show linear level repulsion, while those without time reversal symmetry have β=2, quadratic level repulsion. The strongest level repulsion is seen with β=4 for systems with time reversal symmetry and an additional spin-$\frac{1}{2}$ interaction.

Another example is the phenomenon of 'dynamical localisation' (DL), the so called quantum suppression of chaotic diffusion. This has been extensively studied in periodically driven or kicked systems (see chapters 2 and 3). For time-periodic systems, the eigenvalues and eigenvectors of the time evolution operator (Floquet states) play a role analogous to the eigenvalues and eigenvectors of the Hamiltonian in a time independent system. The time evolution is also quasi-periodic. This has experimentally interesting consequences. For

example, it has been found experimentally [20] that a cloud of cold atoms in a pulsed standing wave of light can only absorb energy up to a 'break time'. This was a realisation of the 'quantum kicked rotor' (QKR).

Experiments and theoretical investigations at UCL showed that if one breaks the spatial and temporal symmetries, this yields novel dynamics. It was found that one could exploit this to generate ratchet motion [40] and atom filters [43]. Both the ratchet and filter dynamics involve time periodic systems and hence Floquet states.

The aim of this thesis is to interpret and shed further light on the systems studied in [43, 57] by investigating the corresponding Floquet states and their eigenvalues, i.e. 'quasi-energies'.

In chapter 2, a review of the standard map and quantum kicked rotor is given. The basis of Floquet theory and the phenomenon of dynamical localisation are also introduced.

In chapter 3, an introduction to the Hamiltonian chaotic ratchets studied theoretically and experimentally at UCL is given. This chapter includes an account of the experimental set up and observations at UCL.

In chapter 4, the atom filter and its best experimental realisation for the 2δ or double delta kicked rotor are described. The classical and quantum numerical results for the energy and momenta of atomic clouds in pulsed optical lattices are presented. These are compared with analytical formulae obtained for the classical diffusion correlations [58]. The experimental results are also presented in this chapter.

In chapter 5, the properties of Floquet states for those two systems described in chapter 3 and 4 are explored. A study of their localisation properties is used to analyse the ratchet currents and the variations in energy absorbed as a function of the initial momentum of the wave packet (relative

to the lattice).

In chapter 6, the statistical properties of the eigenvalues for the 2δ-kicked rotor are investigated. A brief introduction of the universality of the random matrix theory and the band random matrix theory for the localised quantum dynamical systems is given. The investigations are performed by obtaining the number variance statistics and the nearest neighbouring spacing distributions of the eigenvalues of the system.

In chapter 7, conclusions with a brief summary of the completed work in this thesis are given. Possible applications and further directions are also discussed.

CHAPTER 2

The standard map

This thesis presents a number of numerical and experimental results obtained from two systems: the perturbed-period and 2δ-kicked rotor system, which are slightly modified from the well known standard kicked rotor model. It is therefore necessary to start with introducing the standard map. Since Casati *et al* [3] in 1979 first introduced the standard mapping to describe the kicked rotor model, this model now is known to be a good model to investigate dynamical chaos both classically and quantum mechanically. In fact, the standard mapping in the classically chaotic dynamics is a basic model for understanding some of the concepts of quantum chaos. This chapter thus describes the classical kicked rotor model as well as the quantum one, and also a very important feature, dynamical localisation, which only occurs quantum mechanically. It has been proved [1] that dynamical localisation is related to Anderson localisation in solid state physics. In the later part, some experimental developments follow. Briefly, therefore, this chapter includes:

- the classical and quantum kicked rotor system, including the standard map,

dynamical localisation, link to Anderson localisation

• experimental observations of the kicked rotor.

2.1 The kicked rotor system

2.1.1 The classical kicked rotor

The kicked rotor is one of the most widely and thoroughly studied chaotic systems, both classically and quantum mechanically. To begin with, let us consider a one dimensional rotor subject to a periodic train of delta kicks, $\sum_n \delta(t/T - n)$. The Hamiltonian for the system is given by:

$$H(L, \theta, t) = \frac{L^2}{2I} + k \cos\theta \sum_n \delta(t/T - n) \tag{2.1}$$

The first term describes the rotation of a pendulum with angular momentum L, and moment of inertia I. The second term describes periodic kicks with a period T by a pulsed potential of k. The equations of motion are given by:

$$\begin{aligned} \dot{L} &= -\frac{\partial H}{\partial \theta} = k \sin\theta \sum_n \delta(t/T - n), \\ \dot{\theta} &= \frac{\partial H}{\partial L} = \frac{L}{I} \end{aligned} \tag{2.2}$$

The evolution of the system with time can be divided into two periods of motion: a free evolution part and a kick part. As L changes discontinuously at each kick, the system can be translated into a discrete mapping. If L_n, θ_n are the values of the variables just before the nth kick, then L_{n+1} and θ_{n+1} which are just after the nth kick take the values:

$$\begin{aligned} \theta_{n+1} &= \theta_n + l_{n+1} \\ l_{n+1} &= l_n + K \sin\theta_n \end{aligned} \tag{2.3}$$

where $l_n = \frac{L_n T}{I}$ is the scaled angular momentum and the stochasticity parameter, $K = \frac{kT^2}{I}$, describes the strength of the kick in dimensionless units. This is the well known Chirikov's *standard map* [4] and shows the transition of a Hamiltonian system from regular to chaotic behaviour when changing one control parameter K. It is important that this mapping cannot be solved analytically, so one can only obtain information on the system (l_n and θ_n) by iterating the map itself.

One valuable way of extracting information from this procedure is to construct the Poincaré surface of section (SOS). The angle variable θ is periodic in 2π, but the angular momentum l is unbounded. In this thesis, I and T are considered to be normalised to one so that $k = K$. Figure 2.1 shows Poincaré surface of section of the map for different values of K (in the figure, l and θ are replaced by p and x respectively).

For small $K \leq 0.3$, the rotor behaves regularly for most of the initial values of l and θ. The motion proceeds on invariant tori, which appear as horizontal or elliptical curves or islands. These tori are known as KAM tori (named after Kolmogorov (1954), Arnold (1963) and Moser (1962), who postulated and proved that for systems perturbed from integrable ones, invariant curves continue to exist for most initial conditions). These KAM tori exist for small K and represent impenetrable barriers to diffusion. As increasing K, the tori are destroyed and become cantori (broken KAM tori). The deforming process starts from the straight horizontal line (occupied for $K = 0$), $p = 2\pi R$, where R is the rotation number and is given by

$$R = \lim_{m\to\infty} \frac{1}{2\pi m} \sum_{n=1}^{m} p_n. \tag{2.4}$$

With increasing K more and more tori break up, chaotic regions emerge between still existing KAM tori, then eventually, the last invariant torus

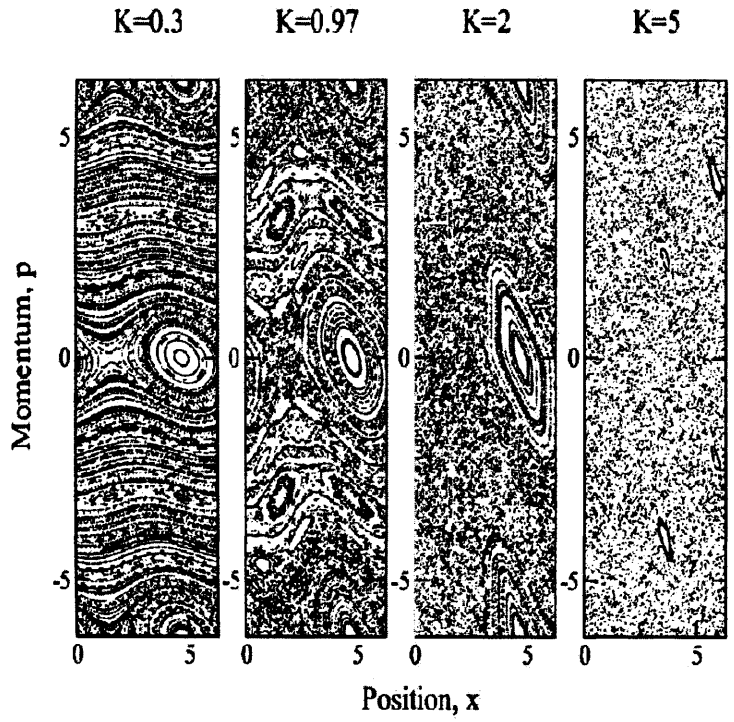

Figure 2.1: Poincaré surface of sections with increasing kick strength for the standard map.

breaks at a critical value of K_c=0.9716.... This last torus corresponds to the 'golden mean', $R = \frac{\sqrt{5}-1}{2}$, which is considered to be, in some sense, the most irrational number. However, there are still regular regions in the form of islands in the phase space. As K increases, eventually, the majority of the phase space becomes chaotic for $K \geq 5$. After the critical value K_c, where the last KAM tori are destroyed, the motion in phase space becomes diffusive and the energy of the system grows indefinitely. If the initial conditions are chosen within the chaotic regions, the trajectories will expand through all phase space. Full details of the KAM theorem can be obtained from [5].

Consider an ensemble of M rotors with initial conditions $(\theta_0^{(m)}, l_0^{(m)})$, where $m = 1, 2, ...M$. The average kinetic energy before nth kick can be written as

$$\bar{E}_n = \frac{l_n^2}{2} = \frac{1}{2M}\sum_{m=1}^{M}\left[l_n^{(m)}\right]^2 \tag{2.5}$$

The averaged energy from kick to kick can be obtained as follows

$$\begin{aligned}
\bar{E}_{n+1} &= \frac{1}{2M}\sum_{m=1}^{M} {l_{n+1}^{(m)}}^2 \\
&= \frac{1}{2M}\sum_{m=1}^{M}\left[l_n^{(m)} + K\sin(\theta_n^{(m)})\right]^2 \\
&= \frac{1}{2M}\sum_{m=1}^{M}\left[{l_n^{(m)}}^2 + 2Kl_n^{(m)}\sin(\theta_n^{(m)}) + K^2\sin^2(\theta_n^{(m)})\right]
\end{aligned} \tag{2.6}$$

If we assumed that $l_n^{(m)}$ and $\theta_n^{(m)}$ are uncorrelated with zero average, then the above equation can be approximated as

$$\bar{E}_{n+1} \simeq \bar{E}_n + \frac{1}{4}K^2 \tag{2.7}$$

Thus, the growth rate of the average energy can be described by

$$\bar{E}_n = D_{ql}n \tag{2.8}$$

with the quasi-linear diffusion constant D_{ql} given by

$$D_{ql}(K) \simeq \frac{K^2}{4}, \tag{2.9}$$

where n indicates the number of kicks. The quasi-linear approximation is sufficient when K is very large. In [6, 7, 8], Rechester *et al* evaluated a few low-order correction terms, which was shown to be

$$D(K) = \frac{K^2}{2}[\frac{1}{2} - J_2(K) - J_1^2(K) + J_2^2(K) + J_3^2(K)] \tag{2.10}$$

The ratio D/D_{ql} oscillates as a function of K and decays as $1/\sqrt{K}$. In this thesis, we will see that these higher order correction terms play a very important role when we introduce a perturbation in the kick period.

2.1.2 The quantum kicked rotor

The quantum Hamiltonian of the classical kicked rotor is obtained by replacing L by $\frac{\hbar}{i}\frac{\partial}{\partial\theta}$. We thus have

$$\hat{H} = \frac{\hat{L}^2}{2I} + \epsilon_0 \cos\theta \sum_n \delta(t/T - n) \tag{2.11}$$

where $\hat{L}$ is the quantum angular momentum, I is moment of inertia and ϵ_0 is the kick strength. In analogy to the classical case, the quantum Hamiltonian can be solved by means of constructing a mapping, and here, the mapping operator is the time evolution operator of the rotor over one period T. The time dependent Schrödinger equation is defined as

$$i\hbar\frac{\partial\psi(t)}{\partial t} = \hat{H}\psi(t). \tag{2.12}$$

The general solution for time independent Hamiltonian is given by

$$\psi(t) = e^{-i\hat{H}t/\hbar}\psi(t_0). \tag{2.13}$$

This implies that if we know the state vector $\psi(t_0)$, $\psi(t)$ is determined at all time t. Thus, an evolution operator is defined by

$$|\psi(t)>=\hat{U}(t,t_0)|\psi(t_0)> \tag{2.14}$$

This operator is unitary, i.e. $U^{\dagger}U = I$. If a Hamiltonian is time independent, then

$$\hat{U}(t,t_0) = e^{-i\hat{H}t/\hbar} \tag{2.15}$$

while for a time dependent Hamiltonian,

$$\hat{U}(t,t_0) = \hat{T}e^{-i/\hbar\int_{t_0}^{t}\hat{H}(t')dt'} \tag{2.16}$$

where $\hat{T}$ is a time ordering operator. For the quantum δ-kicked rotor, the evolution operator can be separated into a 'kick' part and 'free' evolution part,

$$\hat{U}(t,t_0) = \hat{U}_{free}\hat{U}_{kick} \tag{2.17}$$

Each part can be written as

$$\hat{U}_{free} = e^{-i\hat{L}^2T/2I\hbar} \tag{2.18}$$

$$\hat{U}_{kick} = e^{-i\epsilon_0\cos\theta T/\hbar} \tag{2.19}$$

Introducing the dimensionless angular momentum $\hat{l}$ according to $\hat{L} = \hat{l}\hbar$ and the dimensionless control parameters $\tau = \hbar T/I$, $k = \epsilon_0 T/\hbar$, the evolution operator can now be written as

$$\hat{U} = e^{-i\frac{\tau\hat{l}^2}{2}}e^{-ik\cos\theta} \tag{2.20}$$

The classical analogue of the quantum mapping (2.20) obtained from Eqn. 2.3 is

$$\begin{aligned} l_{n+1} &= l_n + k\sin\theta_n \\ \theta_{n+1} &= \theta_n + \tau l_{n+1} \end{aligned} \tag{2.21}$$

Changing variables to $p = \tau l$, it can be written as in the classical standard map

$$\begin{aligned} p_{n+1} &= p_n + K \sin\theta_n \\ \theta_{n+1} &= \theta_n + p_{n+1} \end{aligned} \tag{2.22}$$

where now $K = k\tau$. From this relation, a classical kicked rotor characterised by the single parameter K can be associated with a quantum kicked rotor characterised by the two parameters k and τ.

A simple rotor wave function ψ_0 at time $t = 0$ can be expanded in the complete set of angular momentum eigenstates, i.e.,

$$\psi_0 = \sum_l A_l^{(0)} |l> \tag{2.23}$$

where the angular momentum eigenstates $|l>$ are given in θ representation,

$$< \theta|l >= \frac{1}{\sqrt{2\pi}} e^{il\theta} \tag{2.24}$$

The matrix elements are given by:

$$< m|\hat{U}|l >= \frac{1}{2\pi} \int_0^{2\pi} e^{-im\theta} \hat{U} e^{il\theta} d\theta \tag{2.25}$$

Putting the evolution operator obtained earlier, it becomes:

$$< m|\hat{U}|l >= \frac{1}{2\pi} \int_0^{2\pi} e^{-im\theta} e^{-i\frac{\tau l^2}{2}} e^{-ik\cos\theta} e^{il\theta} d\theta \tag{2.26}$$

By using the Bessel function, it can be written as

$$J_{|l-m|} = \frac{1}{2\pi} \int_0^{2\pi} d\theta e^{i(l-m)\theta} e^{-ik\cos\theta} \tag{2.27}$$

The matrix elements of $\hat{U}$ are now given by

$$U_{lm} \equiv < l|\hat{U}|m >= i^{l-m} e^{-i\frac{\tau l^2}{2}} J_{|l-m|}(k) \tag{2.28}$$

Therefore, the *nth* iteration of the wave function ψ_0, ψ_n, can be obtained via their expansion amplitudes by simple matrix multiplication according to

$$A_l^{(n+1)} = \sum_m U_{lm} A_m^{(n)} \tag{2.29}$$

In analogy to the classical kicked rotor, the mean kinetic energy of the kicked rotor is given by

$$< E_n >=< \psi_n | \frac{\hat{l}^2}{2} | \psi_n >= \frac{1}{2} \sum_l l^2 |A_l^{(n)}|^2 \tag{2.30}$$

Fig. 2.2 illustrates the mean energy growth in the classically chaotic regime for three different cases, $\tau = \pi/3$ and 1 for the quantum cases and $K = 5$ for the classical case. The quantum control parameters are chosen to be τ=1 and k=5 corresponding to the classical parameter $K = k\tau$=5 in the chaotic regime. Both the classical and quantum rotor start at t=0 with l=0. Here, two very interesting features were observed in the line a and b. Firstly, the line a corresponds to a quantum resonance. When τ is a rational multiple of π, quadratic energy growth with kick number is observed. Quantum resonance in the kicked rotor was first analysed by Izrailev and Shepelyanskii in 1979 [10, 11]. This effect can be understood by considering the free evolution between kicks, $U_{free} = e^{-i\frac{\tau l^2}{2}}$, where l is an integer. If τ is a rational multiple of π, the phase is not randomised between consecutive kicks, for example, for $\tau = 4\pi$, U_{free}=1 meaning that the system experiences no evolution at all between kicks. Hence, the effect of the kicks accumulates consecutively. Secondly, dynamical localisation was observed for τ=1 (line b). The dynamical localisation manifests the suppression of the quantum energy growth while the classical energy grows diffusively (line c) as seen in the figure. This is a purely quantum effect and so important that we discuss it in detail in the following section.

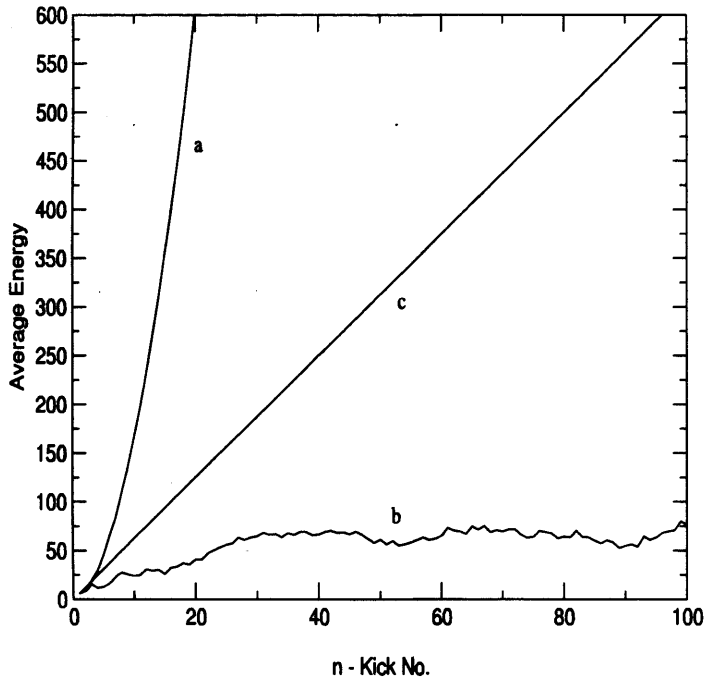

Figure 2.2: Energy vs time for the standard kicked rotor. Classical (c) and quantum cases (a and b) are shown. The line a displays the effect of quantum resonance while the line b shows well known dynamical localisation, where energy growth is suppressed due to an effect of a destructive phase interference. On the other hand, the classical energy (line c) grows linearly [9].

2.1.3 Dynamical localisation

It is understood that dynamical localisation arises from destructive quantum interference, which freezes the wave function spreading in momentum space after the 'break time' t^*, where the quantum energy growth deviates from the classical energy growth: the quantum energy grows as the classical energy does until the quantum energy growth is arrested by the effect of the dynamical localisation. Dynamical localisation is characterised in terms of the localisation length of the momentum distribution. The localisation length defines how fast the momentum falls off exponentially after the wave function becomes frozen in momentum space. The localisation of the quantum rotor wave function in angular momentum space can be plotted by the absolute squares of the time averaged expansion amplitudes of the rotor wave function over the angular momentum basis, i.e.,

$$N_l = \frac{1}{M}\sum_{n=1}^{M} |A_l^{(n)}|^2 \tag{2.31}$$

The average is over the first N kicks. Then, the localisation is approximately described by

$$N_l \sim e^{-2|l|/L} \tag{2.32}$$

here, L indicates the localisation length (see figure 2.3). Shepelyansky in [12] found the relation between the localisation length L and the classical diffusion rate and the break time, $L \sim D/\hbar$ and $t^* \sim L/\hbar$. The dynamical localisation does not rely on the detail of the Hamiltonian but on the time periodicity i.e., the Hamiltonian must be time periodic. Deviation from exact periodicity or an external perturbation destroys dynamical localisation and classical behaviour is regained (see [26]).

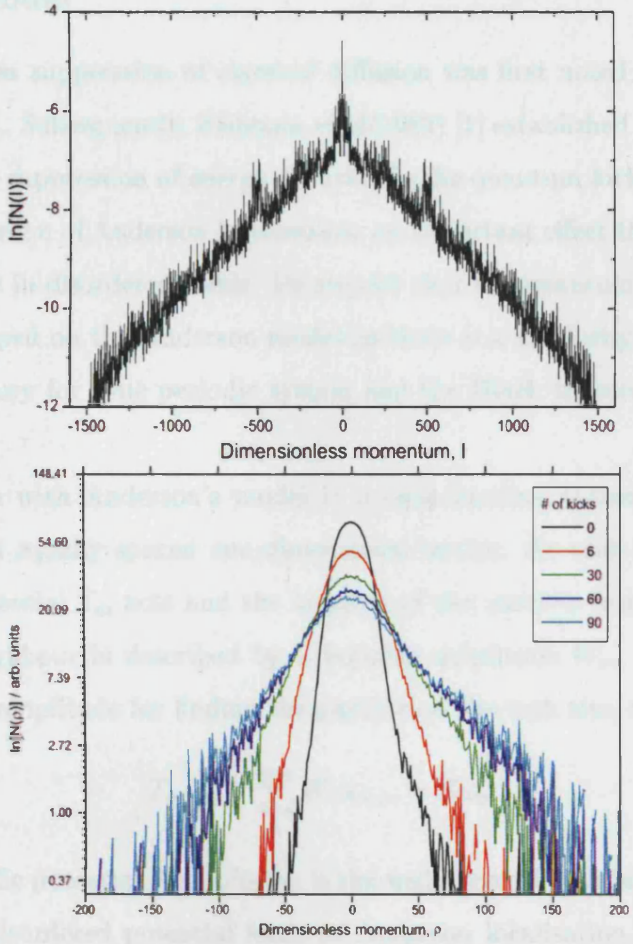

Figure 2.3: Numerical (top) and experimental results (bottom) of dynamical localisation in the kicked rotor. Note the characteristic triangular shape of the natural logarithm of the momentum distribution - the hallmark of dynamical localisation for K=5(top) and K=3.4(bottom). The experimental results were obtained by the Laser cooling group at UCL. Courtesy of Goonasekera [63].

2.1.4 The kicked rotor as a variant of the Anderson model

The quantum suppression of classical diffusion was first noted by Casati *et al* (1979) [3]. Subsequently, Fishman *et al*(1982) [1] established a connection between the suppression of energy diffusion in the quantum kicked rotor and the phenomenon of Anderson localisation, an important effect that limits the conductance in disordered solids. He showed that the quantum kicked rotor can be mapped on the Anderson model as there is a similarity between the Floquet theory for time periodic system and the Bloch theorem for spatial periodicity.

To begin with Anderson's model in a tight binding system, consider a particle in a equally spaced one dimensional lattice. At each lattice site a random potential T_m acts and the hopping of the particle from one site to its r-th neighbour is described by a hopping amplitude W_r. If u_m is the probability amplitude for finding the particle on the mth site, then we have

$$T_m u_m + \sum_r W_r u_{m+r} = E u_m \tag{2.33}$$

For a periodic potential, the solution is the well known Bloch function, while a random disordered potential leads to Anderson localisation. In order to establish the relation between Anderson's hopping model and the kicked rotor, we start with a time periodic Hamiltonian. The evolution operator that evolves the wave function by one period of time T, is defined by

$$\hat{U}\psi(\theta, t) = \psi(\theta, t + T) \tag{2.34}$$

For the Hamiltonian for the quantum standard kicked rotor, the evolution operator takes the form over one period T in rescaled unit (here, for simplicity,

$\hbar$=1 and T=1),

$$\hat{U}\psi(\theta,t) = \psi(\theta,t+1) \tag{2.35}$$

$$\hat{U} = e^{-i\hat{H}_0}e^{-iV(\theta)} \tag{2.36}$$

$$\hat{H}_0 = \frac{\hat{p}^2}{2} \tag{2.37}$$

$$V(\theta) = k\cos(\theta) \tag{2.38}$$

The time evolution of the wave function can be expanded in terms of quasi-energy states $\psi_\omega(\theta,t)$, i.e.

$$\psi(\theta,t) = \sum_\omega A_\omega \psi_\omega(\theta,t), \tag{2.39}$$

where A_ω are constant that are determined from the initial state $\psi(\theta,t=0)$. The quasi-energy states are the eigenstates of the quasi-energy operator (the time evolution operator).

$$\hat{U}\psi_\omega(\theta,t) = e^{-i\omega}\psi_\omega(\theta,t) \tag{2.40}$$

The phase ω is termed the quasi-energy and is real since $\hat{U}$ is unitary. ψ_ω are the Floquet states in time, the eigenstates of a time periodic system. Floquet theory is described in chapter 5 in great detail. The form can be written in the following way

$$\psi_\omega(\theta,t) = e^{-i\omega t}u_\omega(\theta,t) \tag{2.41}$$

where u_ω is periodic in time with the same periodicity as the Hamiltonian, i.e, $u_\omega(\theta,t) = u_\omega(\theta,t+1)$. These states are orthogonal.

Now, an equation for the projections of the quasi-energy states on the angular momentum states can be derived. Let u_ω^+ and u_ω^- be the values of u_ω just before and after a kick respectively. The corresponding values of the

wave function are $\psi_\omega^\pm = e^{-i\omega t}u_\omega^\pm$. Between two consecutive kicks at times t and $t+1$, the free evolution part is given by

$$\psi_\omega^-(\theta, t+1) = e^{-iH_0}\psi_\omega^+(\theta, t) \tag{2.42}$$

with 2.41 this leads to

$$u_\omega^-(\theta, t+1) = e^{i(\omega - H_0)}u_\omega^+(\theta, t) \tag{2.43}$$

Projecting on a state of angular momentum l, one finds

$$u_l^- = e^{(\omega - l^2/2)}u_l^+ \tag{2.44}$$

where $u_l^\pm = < l|u_\omega^\pm(\theta, t) >$ and $H_0|l> = \frac{p^2}{2}|l> = \frac{l^2\hbar^2}{2}|l> = \frac{l^2}{2}|l>$.

At each kicking, a simple phase shift occurs. Hence, it is easily dealt with in the θ presentation (as shown in [13, 2]).

$$u^+(\theta) = e^{-iV(\theta)}u^-(\theta) \tag{2.45}$$

Substituting

$$e^{-iV(\theta)} = \frac{1 + iW(\theta)}{1 - iW(\theta)} \tag{2.46}$$

where $W(\theta) = -\tan(V(\theta)/2)$.

From those equations above, one can obtain (as shown [13, 2])

$$(1 - iW(\theta))\bar{u}(\theta) = e^{i(\omega - H_0)}(1 + iW(\theta))\bar{u}(\theta) \tag{2.47}$$

where

$$\bar{u}(\theta) = \frac{1}{2}[u^+(\theta) + u^-(\theta)] \tag{2.48}$$

This can be expressed in the following way

$$T_l\bar{u}_l + \sum_r W_{l-r}\bar{u}_r = 0 \tag{2.49}$$

$$T_l = \tan\left[\frac{1}{2}(\omega - l^2/2)\right] \tag{2.50}$$

where $\bar{u}_l$ and W_l are the projections of $\bar{u}(\theta)$ and $W(\theta)$ on the angular momentum states, while W_{l-r} are the hopping matrix elements. The relation between the Anderson's hopping model and the kicked rotor is now established. However, there is a subtle difference between the kicked rotor and the Anderson model due to the fact that T_l in the equation 2.50 is not completely random but 'pseudo-random'. However, all numerical evidence has shown that a pseudo-random sequence also leads to localisation [13, 14].

2.2 Experimental observations for the kicked rotor

As the experiments carried out at UCL are described in chapters 3 and 4 with the relevant system, here the experimental realisation for the kicked rotor and the following developments are briefly introduced.

The first experimental realisation of dynamical localisation was achieved by the Raizen group in Texas University, [16] following a suggestion by Graham *et al* [15]. The work was performed with sodium atoms in a standing wave of light (known as an optical lattice). The atoms were cooled to $\sim \mu$K and trapped in a magneto-optical trap (see chapter 3 for more details). The Raizen group first used a periodically driven rotor but the following year, Robinson *et al* in the same group showed further experimental realisation of momentum transfer, in comparison with the underlying classical phase space portraits and the quantum Floquet analysis by using sodium atoms subject to pulsed optical lattice. As the delta kick is not achievable experimentally, a very narrow width of pulse was used. Figure 2.4 shows the clear evidence of the dynamical localisation and characteristic triangle shape of the localised

momentum distribution on a logarithmic scale. The works on the dynamical localisation of ultra-cold sodium atoms are summarised in [20].

In 1998, the group changed to cesium atoms in the kicked rotor experimental setup and investigated the effect of noise on the dynamical localisation [21]. The effect of noise on dynamical localisation is also investigated in [22, 23, 25, 26]. Klappauf *et al* [27] reported the transport properties of the kicked rotor and the dependence of the average energy growth as a function of the kick strength, for which classical diffusion was previously explored by Rechester and White [6, 7]. Experimental observations of related phenomena have been achieved in similar systems, such as quantum resonance and chaos-assisted tunnelling by using cold atoms in a driven optical lattice [28, 29, 24]. Furthermore, other important experiments on quantum accelerator modes have been made by a group at Oxford University [30, 31, 32, 33, 34]. Further details are omitted as our system does not involve such aspects (quantum resonances, chaos-assisted tunnelling and accelerator modes), which are beyond the scope of this thesis.

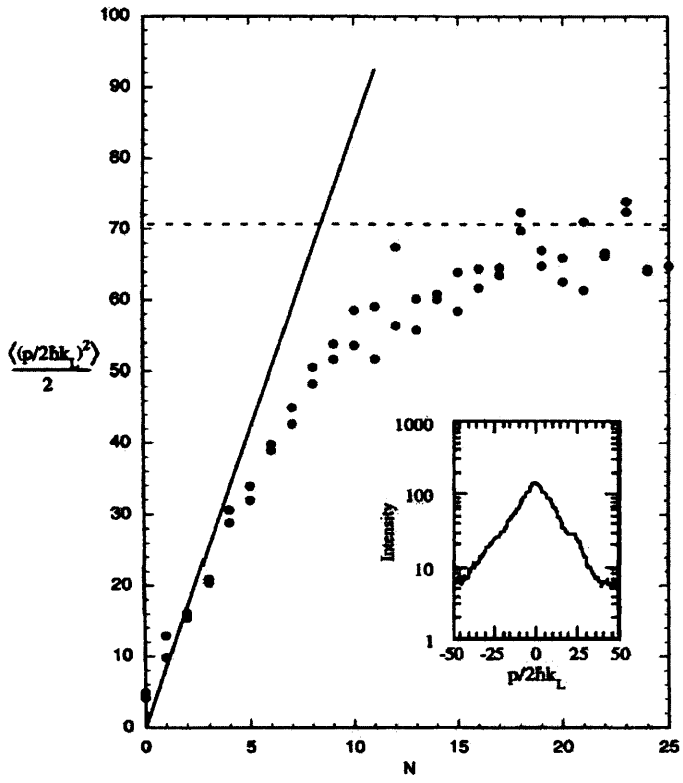

Figure 2.4: Experimental realisation of the dynamical localisation for the quantum kicked rotor, from [19]. The inset shows an experimental measurement of the exponential momentum distribution on a logarithmic scale.

CHAPTER 3

Ratchet with perturbed kicks

Recently, the system with cold atoms in optical lattices subject to cycles of unequally-spaced pulses has been explored both theoretically and experimentally by the quantum chaos and laser cooling group at UCL [40, 43, 45]. A chaotic quantum ratchet mechanism and a filtering effect were identified in the theoretical studies as a result of small perturbations in the kick-period. These 'perturbed-period' kicked rotors (KR) were implemented experimentally by the laser cooling group. This chapter describes the classical and quantum mechanical analysis of the perturbed-period QKR systems and of the corresponding experimental results. The contents of this chapter include:

- a brief explanation of the ratchet and the filtering effect,
- the theoretical analysis and illustration of numerical results of the perturbed-period QKR,
- a brief review of the experimental set up at UCL,
- experimental observations of the rocking ratchet.

3.1 Ratchet and filtering effect

3.1.1 Ratchet

In a theoretical study, the perturbed-period KR was found to yield a ratchet-current even in the chaotic regime [40, 43]. This was unexpected in a chaotic Hamiltonian system, since to date only mixed phase-space ratchet mechanisms had been investigated [46, 47, 48]. A ratchet is a spatially periodic device with broken time-reversal symmetry which generates motion in one direction. An important condition for non trivial ratchet dynamics is the absence of net bias: in other words the time and space-averaged force equals zero. Most of the extensive ratchet literature deals with dissipative or Brownian ratchets [39] and comparatively little theoretical work has been undertaken on Hamiltonian ratchets, which are dissipation and noise-free.

To explain the ratchet effect one often quotes the ratchet and pawl model from Feynman [36]. Feynman used this model to illustrate the second law of thermodynamics, verifying that when the system of each compartment is in thermodynamic equilibrium no work can be extracted from the system (see figure 3.10). But if the system is not in thermodynamic equilibrium, then the asymmetric nature of the ratchet transforms the random fluctuations of the system into work.

Quantum mechanically a ratchet has been used to generate a current in the absence of net force. A quantum kicked rotor (QKR) system with asymmetric potential wells resembles the teeth of the ratchet, in other words, a ratchet effect occurs when the spatial and temporal symmetry is broken in a periodical dynamic system. Therefore, the study of ratchets includes the investigation of transport in the area of quantum transport. However, it

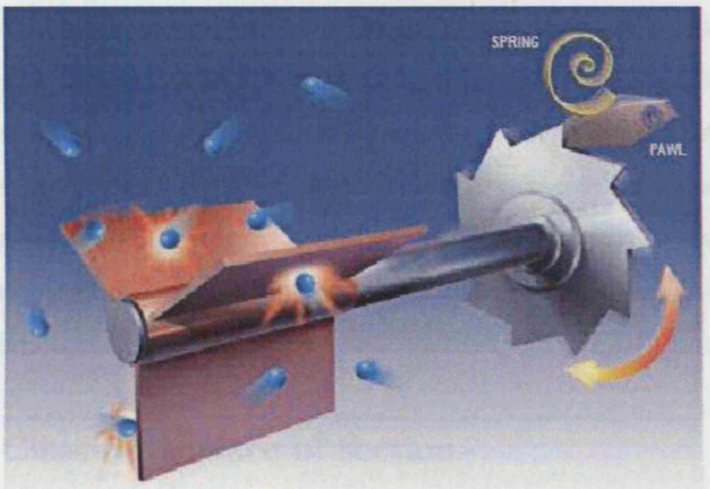

Figure 3.1: The Smoluchowski-Feynman Ratchet. Courtesy of [35].

should be noted that there is a special set of systems which do not exhibit directed transport in the presence of broken spatial symmetry and thermal equilibrium. For a full review, see [37, 38, 39].

The quantum chaos group at UCL previously investigated a ratchet effect using quantum kicked rotor with chirped double well potential (cdw-QKR) with initially fully chaotic regime [40]. It was verified numerically that the system shows the ratchet effect arising from asymmetric dynamical localisation. Following the study of the chaotic Hamiltonian ratchet using cdw-QKR, the group introduced a new 'rocking' potential term into the sinusoidal potential kick in the form of $V(x) = K\cos x + Ax(-1)^j$, where j is the kick number. (In fact, this system was introduced by Chen *et al* [44], who investigated classical dynamics in the regular regime.) As investigated in [43], this system demonstrates the directed transport along with other similarities

to the double well ratchet (eg, asymmetric DL and hence the ratchet current). One of the great advantages of using this system is that it is simpler to study analytically and to implement experimentally than the double well case. The experiments observing the directed transport have been carried out by the laser cooling group at UCL [56, 45]. A brief experimental description and observations of the ratchet system follows in the second section of this chapter.

3.1.2 Classical surface of section

The classical dynamics of the perturbed-period kicked rotor system is given by a 2-kick map:

$$\begin{aligned} x_j &= x_{j-1} + p_j T_1 \\ p_{j+1} &= p_j - V'(x_j) \\ x_{j+1} &= x_j + p_{j+1} T_2 \\ p_{j+2} &= p_{j+1} - V'(x_{j+1}) \end{aligned}$$

For the perturbed-period KR, $T_1 = 1 + \epsilon$ and $T_2 = 1 - \epsilon$, where $\epsilon \ll 1$. Hence, all we have done is to slightly perturb the kicking period about its mean. Note that this system is time-periodic, with period $T_{tot} = T_1 + T_2 = 2$. The Hamiltonian is given by

$$H = \frac{p^2}{2} + V(x) \sum_{n=0}^{\infty} [\delta(t - nT_{tot}) + \delta(t - nT_1)] \tag{3.1}$$

As in the standard map, a sinusoidal potential $K \cos x$ is considered. However, in order to break spatio-temporal symmetries to obtain a ratchet current (see below), a 'rocking' linear potential of strength A is added. As shown earlier, the general form of the potential is $V(x) = K \cos x + Ax(-1)^j$,

where j is the kick number. In experimental implementations of this system, the rocking linear term is obtained by means of an accelerated lattice [45].

The case $A = \pi/2$ is particularly interesting and Fig 3.2 presents the surface of section obtained from the classical map. Parameters are ϵ=0.3, A=$\pi/2$ and the kick strength K= 0.5, 1, 2 respectively. It is clearly seen that the phase space is asymmetric about momentum p=0, and this asymmetry explains the net current produced due to asymmetric diffusion of the ensemble of particles (evolving in the chaotic region).

It has been found [43] that the diffusion constant for the rocking ratchet system is given by

$$D \simeq \frac{K^2}{2}\left[1 - 2J_2(K)\cos(2p_0\epsilon - A) - (J_1(K))^2 \cdots\right]. \qquad (3.2)$$

This implies that atoms with positive momenta will absorb energies at different rates from those with momenta of the same magnitude but moving in the opposite direction. Hence, even if the initial mean-momentum is zero, the diffusion will lead to non-zero momentum current, $< p >$. The asymmetric diffusion represents a sort of chaotic ratchet (using the definition of a ratchet as a spatially periodic device which produces current in the absence of a net bias). This type of chaotic directed motion was first identified in a kicked asymmetric double-well potential [40, 41] which has somewhat more complicated diffusion behaviour: the ratchet mechanism (of a 2-kick asymmetric diffusion correlation) is present there too but is generally weaker (relative to the uncorrelated diffusion) and less easy to investigate since the mathematical form of the diffusion correlations is rather complex. Below, we describe quantum calculations intended to improve the analysis of the experimental results for the system.

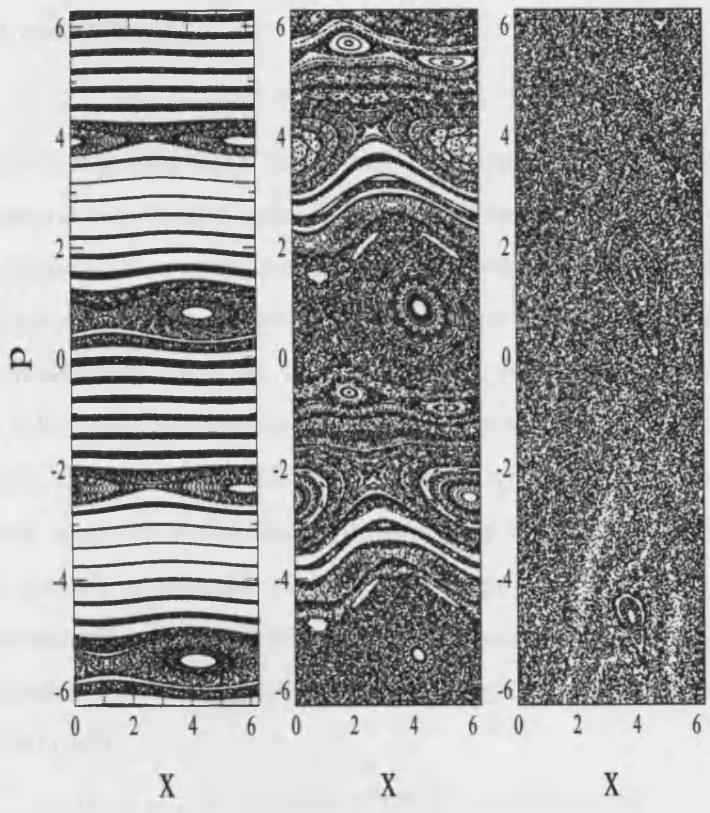

Figure 3.2: Classical surface of section for rocking ratchet, ϵ=0.3 A=$\pi/2$, K=0.5, 1, 2 from left to right respectively.

3.1.3 Quantum theory and results

For periodically δ-kicked systems, the quantum time evolution operator for one period, $U(T)$, allows a fast numerical calculation of the time-evolution of an initial wave-packet. Just as in their classical analogs, we have a 'quantum map' that can be iterated:

$$\psi(t+T) = U(T)\psi(t) \tag{3.3}$$

There are two standard methods for implementing this quantum map. One is a split-operator technique using Fast-Fourier transforms. In the other, the time evolution operator over one period $U(T)$ is represented as a matrix in a basis of plane waves $|l+q>$ where l takes integer number and q is a quasi-momentum and is in the range $-1/2 : 1/2$; the quasi-momentum is required since the cold atom experiments [20] were performed on an optical lattice, which unlike the QKR does not have ratational symmetry , and so initially an ensemble of atoms is distributed *continuously* in momentum. The latter one is particularly straightforward if the periodic kick is a δ kick. For the 2-kick systems, where one period consists of T_1 and T_2, i.e. $T = T_1 + T_2$, the matrix elements for the evolution operator for a given q, U^q over one period, $< n|U^q|l >= i^{n-l}\, e^{-i[(T_1(l+q)^2\hbar/2]} \sum e^{-i[T_2(j+qa)^2\hbar/2]}$ take the form [43]:

$$< n|U^q|l >= i^{n-l}\, e^{-i[(T_1(l+q)^2\hbar/2]} \sum_j e^{-i[T_2(j+qa)^2\hbar/2]} J_{l-j+ka}\left(\frac{K}{\hbar}\right) \times J_{j-n-ka}\left(\frac{K}{\hbar}\right) \tag{3.4}$$

where ka indicates an integer number, i.e., $ka = int(A)$ and qa indicates a fractional number, i.e., $qa = A - ka$. Note that in this system although the one-kick operators $U(T_1)$ or $U(T_2)$ do not conserve quasi-momentum, the full 2-kick operator does. In consequence, as for the standard QKR, each q is considered independently.

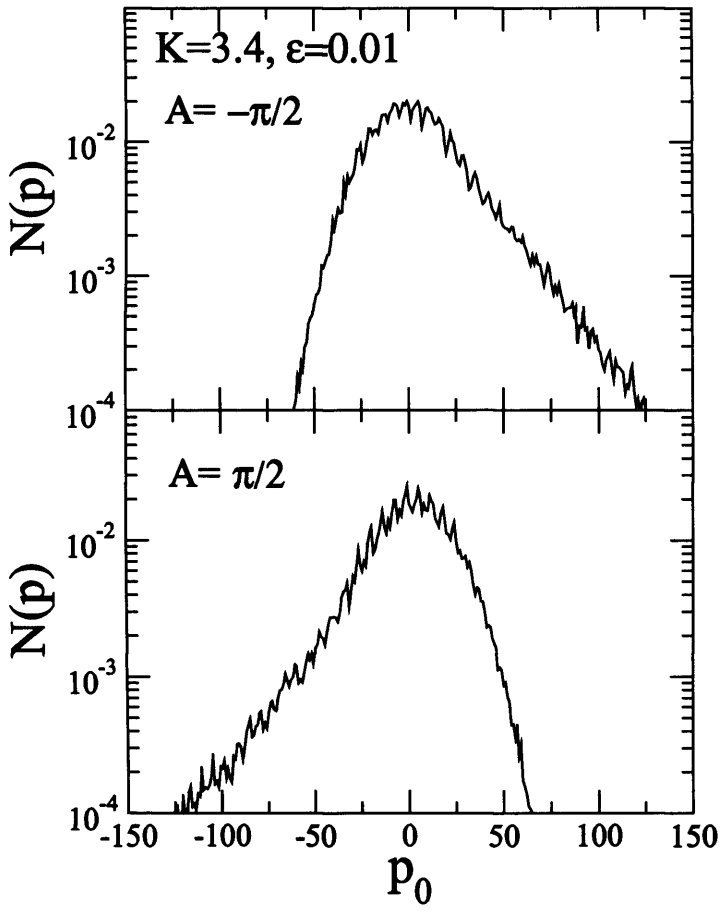

Figure 3.3: The figure plots the momentum probability distribution $N(p)$. It shows asymmetric momentum distribution about p_0=0. This means there is a net current, $< p - p_0 >$. Parameters are K=3.4, $\hbar$=1, ϵ=0.01. Asymmetry is reversed by changing the sign of A, the amplitude of the rocking potential.

For the standard QKR, there is no transport due to symmetric dynamical localisation in (unbounded) momentum space, in other words, the average momentum distribution $N(p)$ is zero. However, when small perturbations in time with broken spatial symmetry are applied to kicking, a ratchet current occurs due to asymmetric (about $< p >=0$) spreading of a quantum wave packet in momentum space. This occurs before the break time and is a direct consequence of asymmetric classical diffusion. Fig. 3.3 clearly shows the asymmetric momentum distribution of the atom cloud initially started at p_0=0. It also illustrates the effect of changing the sign of A. The significance of altering the sign of A is attributed to the rocking potential involving alternating impulses $-V'(x) = K \sin x \pm A$. In fact, the distinction (as may be ascertained from the form of the classical diffusion) is between the case where an impulse $K \sin x + A$ precedes free evolution for a time interval $T_1 = 1 + \epsilon$ (obviously followed by an impulse $K \sin x - A$ and interval $T_2 = 1 - \epsilon$) and the separate case where an impulse $K \sin x - A$ precedes free evolution for a time-interval $T_1 = 1 + \epsilon$ and so forth (which corresponds to a current with the same magnitude but of opposite sign).

Fig. 3.4 shows the average energy spread as a function of initial momentum after 60 kicks. The Figure illustrates the case of $A = 0.01\pi$ (solid line) and of $A = \pi/2$ (dotted line). In both cases, the period is π/ϵ. This results from the form of $\cos(2p_0\epsilon - A)$ in the classical two kick correlation. This also describes the filtering effect which is presented in the next section.

3.1.4 Filtering effect and Husimi representations

As already mentioned, the paper by Jonckheere *et al* [43] found numerically that for a cloud of atoms under delta-kicking with a sinusoidal potential

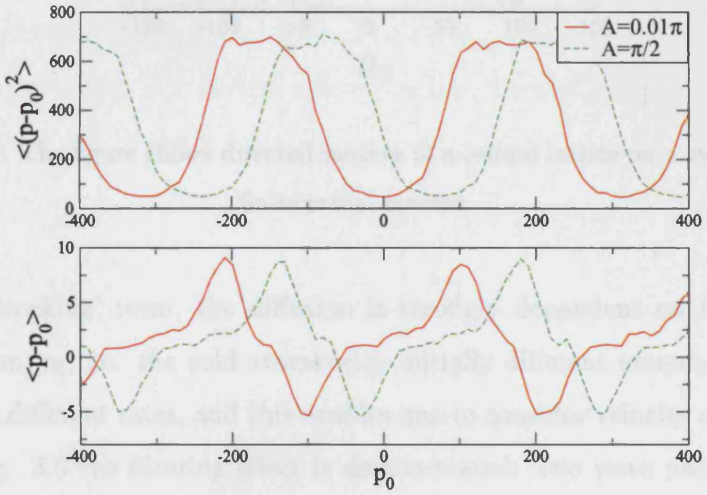

Figure 3.4: The top panel shows average energy spread as a function of initial momentum while the one below shows the current oscillating periodically. Two lines are illustrated with $A = \pi/2$ (dotted line) and $A = 0.01\pi$ (solid line). Parameters are K=3.4, $\hbar$=1, ϵ=0.01. The width of the initial wave packet, β, is 0.25 in momentum space.

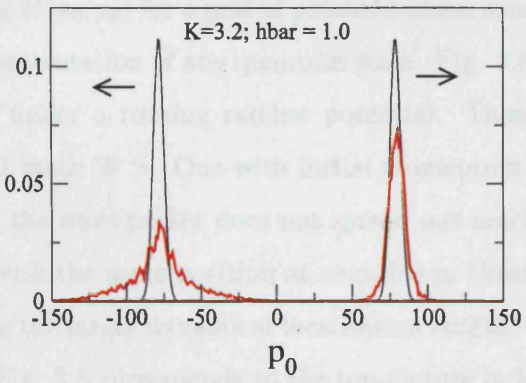

Figure 3.5: The figure shows directed motion in a pulsed lattice on a system with finite initial current

and the 'rocking' term, the diffusion is strongly dependent on the initial momentum, p_0, i.e. the cold atoms with initially different momenta absorb energy at different rates, and this enables one to consider velocity selection.

In Fig. 3.5 the filtering effect is demonstrated: two wave packets after 50 pairs of kicks are moving in opposite directions to each other. The initial wave packets are centred at $\pm p_0$, with $4\epsilon p_0 = \pi$. The figure shows that the wave packet moving right remains almost the same while the other is strongly dispersed. The Husimi distribution is a quantum quasi-probability distribution allowing direct comparison with classical phase space distributions. $H(x_0, p_0)$ is evaluated by calculating the overlap of the quantum state $|\Psi(x)>$ with a minimum uncertainty wave packet (coherent state) on the point [61, 62].

$$H(x_0, p_0) = | < \Psi(x)|\Phi(x, x_0, p_0) > |^2 \tag{3.5}$$

where Φ is a Gaussian wave packet in our case,

$$\Phi_G(x; x_0, p_0) = \frac{1}{\sqrt{2\pi}\sigma} e^{-\frac{(x-x_0)^2}{2\sigma^2} + \frac{ip_0 x}{\hbar}} \tag{3.6}$$

By calculating $H(x_0, p_0)$ for a grid of points in phase space, we can obtain a phase space representation of any quantum state. Fig. 3.6 shows two wave packets evolving under a rocking ratchet potential. These are overlapped with the coherent state $|\Phi>$. One with initial momentum at $p_0 = +(\pi/4\epsilon)$ (top) shows that the wave packet does not spread out much in phase space, while the other with the same position at negative p_0 (bottom) spreads out widely, indicating the larger dynamical localisation length. The wave packet moving right in Fig. 3.5 corresponds to the top picture in Fig. 3.6 while the other corresponds to the bottom.

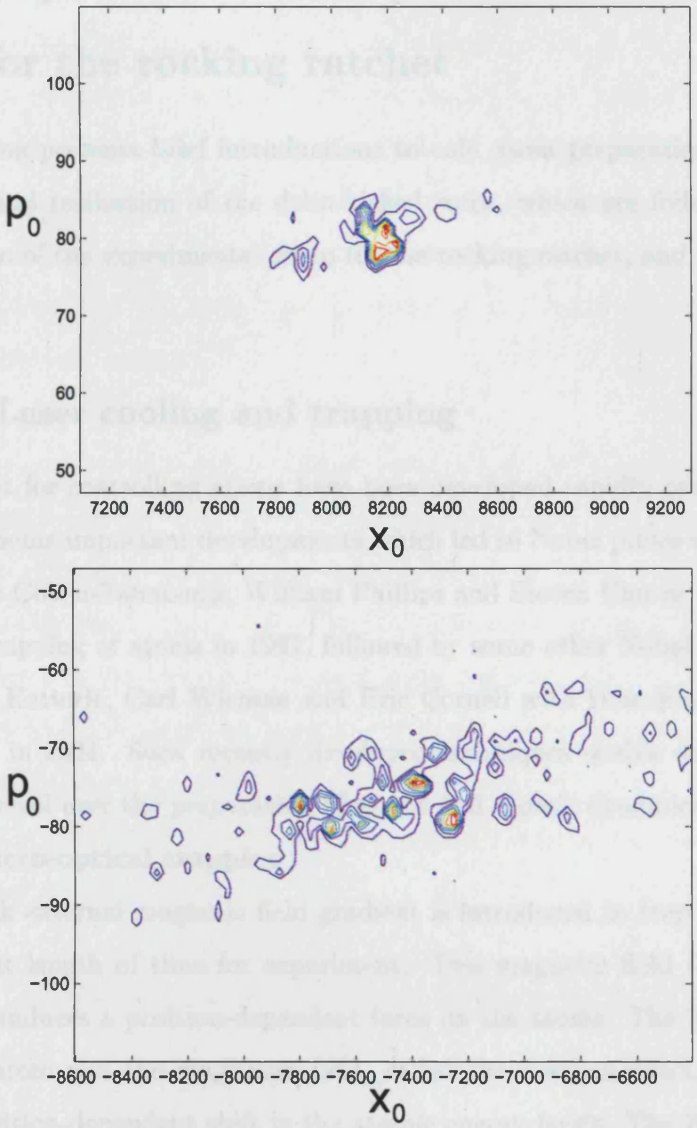

Figure 3.6: Husimis of two wave packets with $\hbar$=1, A=$\pi/2$, K=3.4, ϵ=0.01 and 50 pairs of kicks (i.e., after saturation). The initial wave packets are centred at $p_0 = 78.5$ for the top and $p_0 = -78.5$ for the bottom.

3.2 Experimental description and observations for the rocking ratchet

This section presents brief introductions to cold atom preparation and the experimental realisation of the delta-kicked rotor, which are followed by a description of the experimental setup for the rocking ratchet, and the observations.

3.2.1 Laser cooling and trapping

Techniques for controlling atoms have been developed rapidly over the last decades. Some important developments which led to Nobel prizes were made by Claude Cohen-Tannoudji, William Phillips and Steven Chu in laser cooling and trapping of atoms in 1997, followed by some other Nobel laureates, Wolfgang Ketterle, Carl Wieman and Eric Cornell with Bose-Einstein condensation in 2001. Such recently developed techniques enable detailed coherent control over the preparation of atoms and atomic dynamics.

Magneto-optical trapping

A weak external magnetic field gradient is introduced to trap atoms for a sufficient length of time for experiment. This magnetic field ($\mathbf{B}=b_Z\hat{z}$ in Fig. 3.7) induces a position-dependent force on the atoms. The interaction between atom and the magnetics field, called the Zeeman effect, causes a small, position-dependent shift in the atomic energy levels. The Zeeman effect splits the first excited state of the atom into three sub-levels, $M_J = 0, \pm 1$ during the transition for a $J_g = 0 \rightarrow J_e = 1$ (see Fig. 3.7). (Note that the $J = 0 \rightarrow 1$ transition is used as a simple example. The real atom has the transition $F = 4 \rightarrow 5$.) When the atoms are illuminated by circularly po-

larised light, transitions can be driven between the sub-levels for $\Delta M = \pm 1$. For two circularly polarised beams counter-propagating in the z-direction, atoms with positive z-coordinates will see the $M_J = -1$ level shifted closer to resonance, scatter more σ^- photons than σ^+ photons and be pushed towards the origin. In the same way, the atoms with negative z-coordinates will be pushed towards z=0. Sisyphus cooling is used to lower the atomic temperatures, then, the atoms can be confined in a small volume of space (with a diameter $\sim mm$).

Sisyphus cooling

Sisyphus cooling enables us to cool atoms (about 10^{-9}K) down to micro-Kelvin temperatures. This gives better efficiency than the Doppler cooling, first proposed by Hänsch and Schawlow [60] in 1975. The schematic cooling mechanism is depicted in Fig 3.8. The atom climbing up a hill is pumped down to the potential minima of the other ground state sub-level. The atomic kinetic energy lost is greater than the energy from the light field in each pumping event. This process continues until the atoms become localised in the potential wells. These trapped cold atoms can be very precisely manipulated and measured.

3.2.2 Experimental realisation of the delta-kicked rotor

The cold atom realisation of the delta-kicked rotor(DKR) is mostly used to study chaotic dynamics as it is simple and easy to implement experimentally. The behaviour of an atom confined in a one dimensional optical lattice is considered. Pulsing this 1-D optical lattice over very short time intervals simulates the delta-kicking.

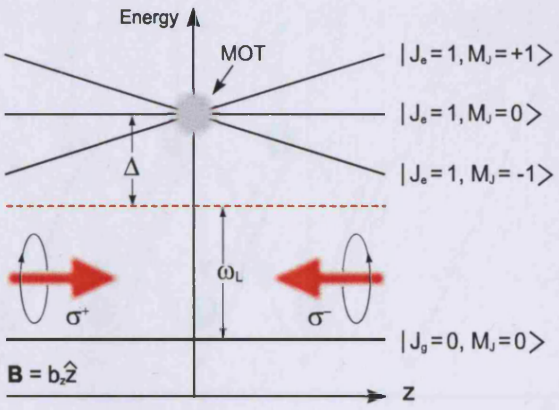

Figure 3.7: The confining effect of the magnetic field in a Magneto-optical trap. Courtesy of Goonasekera [63].

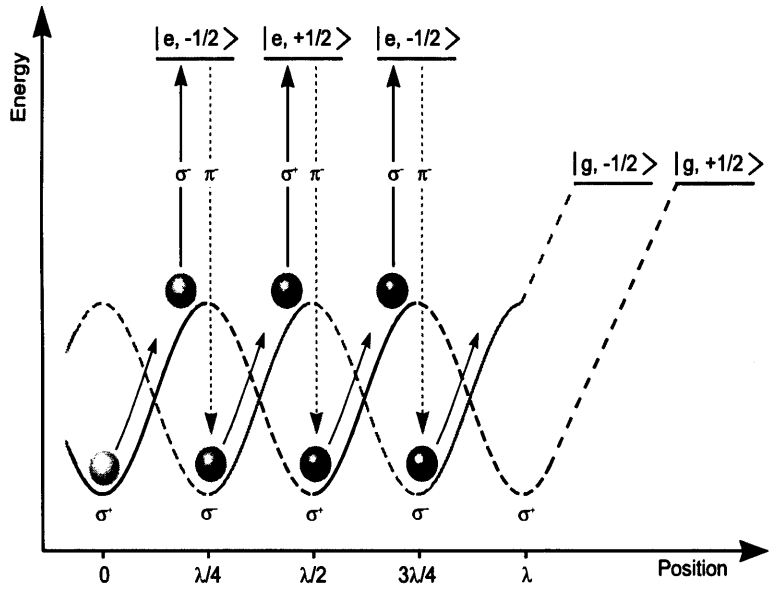

Figure 3.8: The figure shows the process of Sisyphus cooling, as an example, for $J_g = \frac{1}{2} \rightarrow J_e = \frac{3}{2}$ transition in an optical lattice. An atom climbs up a potential hill, the photon absorbed has a lower frequency than the emitted photon. This ensures a loss in atomic kinetic energy. This process continues until the atom becomes trapped near the minimum of the potential well. Courtesy of Goonasekera [63].

The Hamiltonian H is given as a function of position, momentum and time rather than angular momentum and angle as done for the driven rotor.

$$H = \frac{p^2}{2M} + V_0 \cos(2k_L x)\Sigma_n f(t - nT) \tag{3.7}$$

where V_0 is the potential depth, M is the atomic mass, k_L is the laser wavevector and the last term describes a train of integer n square pulses of width t_p separated by a period T. $f(t)$ is a pulse centred around $t = 0$ of width t_p. It is important that $t_p \ll T$ should be ensured to simulate the delta kicking and to avoid the momentum boundary, which confines the atomic diffusion within a certain range of momenta, $\rho_b = \pm 2\pi \frac{t_p}{T}$ and changes the dynamics from those of the QKR. The effect of the momentum boundary for the kicked rotor using cold atoms in optical lattices is shown in [65, 66].

The theoretical analysis in this thesis uses a dimensionless Hamiltonian allowing the system to be described by a small number of parameters, which could be independently varied. The Hamiltonian can be rescaled using the following transformations [20]:

$$\begin{aligned} 2k_L x &\rightarrow x' \\ \frac{2k_L T}{M} p &\rightarrow p' \\ \frac{t}{T} &\rightarrow \tau \\ \frac{8V_0}{\hbar}\omega_r T^2 &\rightarrow k \\ \frac{4k_L^2 T^2/M}{H} &\rightarrow H', \end{aligned} \tag{3.8}$$

where $\omega_r = \hbar k_L^2/2M$ is the atomic recoil frequency. Therefore, the Hamiltonian for the standard kicked rotor is obtained as

$$H' = \frac{p'^2}{2} + k\cos(x')\ \Sigma_n f(\tau - n) \tag{3.9}$$

By considering the commutator $[x', p']=i\hbar'$, the scaled Planck constant becomes $\hbar' = 8\omega_r T$.

3.2.3 Experiments and the results for the ratchet at UCL

As mentioned, for cold atom preparation, the atoms are cooled and trapped in standing wave of light (optical lattice) created by the interference pattern between several laser beams. The experiments at UCL use a simple far-detuned, 1D lattice formed by two counter propagating beams [54, 55]. To investigate the ratchet, an additional linear potential was required.

Directed transport due to asymmetric momentum diffusion can be generated simply by breaking the temporal symmetry of the delta kicked rotor [56] and a two-period kick sequence with a small perturbation between pairs are employed and studied in [53]. The rocking linear potential taken for the experiment is

$$V(x) = K\cos x + Ax(-1)^n \tag{3.10}$$

where n is the kick number, and the diffusion rate becomes

$$D(p_0) \simeq K^2/2[1/2 - J_1(K)^2 - J_2(K)\cos(2p_0\epsilon - A)]. \tag{3.11}$$

For experimental realisation of directed transport, the experimental group at UCL used the moving lattice technique to control the initial atomic momentum p_0. The group introduced a small frequency difference, Δf, between the lattice beams to form a 1-D travelling interference pattern in the laboratory frame. The cesium atoms are first trapped and cooled to $6\mu K$ by using MOT then, loaded into far-detuned optical lattice being pulsed to simulate delta kicks. The atoms remain stationary in the laboratory frame but have

a non zero initial momentum ρ_{L0} in the moving lattice frame. The moving lattice can be controlled by changing the magnitude of Δf.

For the ratchet experiment, the moving lattice apparatus is adjusted to include a linear potential gradient, A (see Eqn. 3.10): two beams move at a constant speed $\lambda\Delta f$. A frequency difference $2\Delta f$ introduced between two beams, which are overlapped to produce kicking potential, causes the interference pattern. $\lambda\Delta f$ has constant velocity when Δf is constant. However, the accelerating lattices can be achieved by varying the frequency difference which changes with time ($\Delta f(t)$) to one lattice beam. The acceleration is given as $a = \frac{\lambda}{2}\frac{d\Delta f(t)}{dt}$. Then, the Hamiltonian in the accelerating frame is

$$H = \frac{p^2}{2M} + V_0 \cos(2k_L x)\Sigma_n f((t - nT_{tot}) + (t - nT_1)) + Max \qquad (3.12)$$

where x and p are variables in the accelerating frame. The rocking potential gradient is now given by $A = 2k_L a T t_p$. Linearly ramping $\Delta f(t)$ by an amount of ν over one period T corresponds to a linear acceleration $a = \lambda\nu/2T$ and thus a linear potential gradient of $A = 2\pi\nu t_p$. The sign of A can be changed by accelerating the lattice in the opposite direction. More details are given in [68].

Fig. 3.9 shows three momentum distributions for $A = -\pi/2$, 0, $\pi/2$, obtained with cesium atoms in [45]. The top figure illustrates the changes of distribution depending on the sign of A and the bottom figure shows the first moment of the distribution for $A = -\pi/2$ and $\pi/2$. Fig. 3.10 shows the same experimental momentum distributions in the separate plots for $A = \pm\pi/2$ in order to compare with the numerical results in Fig. 3.3. (It should be noted that the value ρ in the experimental descriptions is equivalent to momentum p in the theoretical descriptions.) From all those figures, it is clearly seen that the origin of the non-zero momentum current is the asymmetric momen-

tum distribution, and changing the sign of A reverses the asymmetry. Note that the experimental range of $K \simeq 2.6 - 3.4$ does correspond to a classical surface of section with some islands. However, classical quantities such as the average energy are very accurately given by diffusion rates (with 2- and 3-kick corrections). The essential mechanism is asymmetric chaotic diffusion: similar behaviour was found at larger K in [40] in regimes where there are no visible classical islands (but for which experiments are not available); hence, in the analysis of this type of ratchet, the presence (or otherwise) of small stable islands is immaterial. What is important, though, is that since the asymmetric diffusion term is $2J_2(K)\cos(2p_0\epsilon - A)$, we need $J_2(K) \neq 0$. Thus, the much-studied (for the standard map) parameter value $K = 5$ does *not* produce asymmetry since $J_2(5) \simeq 0$. Values of $K \simeq 2.5 - 3.5$, $\hbar = 1/4 - 1$, on the other hand, turned out to be experimentally convenient and produced the strongest asymmetries.

Fig. 3.11 shows a plot of the experimental ratchet current (due to the asymmetric momentum diffusion) obtained in [45] using distributions $N(p - p_0)$ of cold cesium atoms with $p_0 = 0$, in an optical lattice pulsed with unequal periods. The momentum distribution is essentially unchanged after about 60 kicks; the plotted values correspond to about $T = 200$ kicks, hence well after dynamical localisation. Full details are given in [45]. By employing an accelerated lattice, the experiment simulated an effective rocking potential with a given value of A. The current (the first moment of each localised distribution $I = \langle p - p_0 \rangle$) was then calculated, and plotted as a function of A in Fig. 3.11.

As one can see in Fig. 3.11, the ratchet current oscillates sinusoidally, i.e. $I \propto \sin(2p_0\epsilon - A)$. This can be qualitatively understood from the form of the classical 2-kick momentum-diffusion correction (Eq. 3.2) $C_2 =$

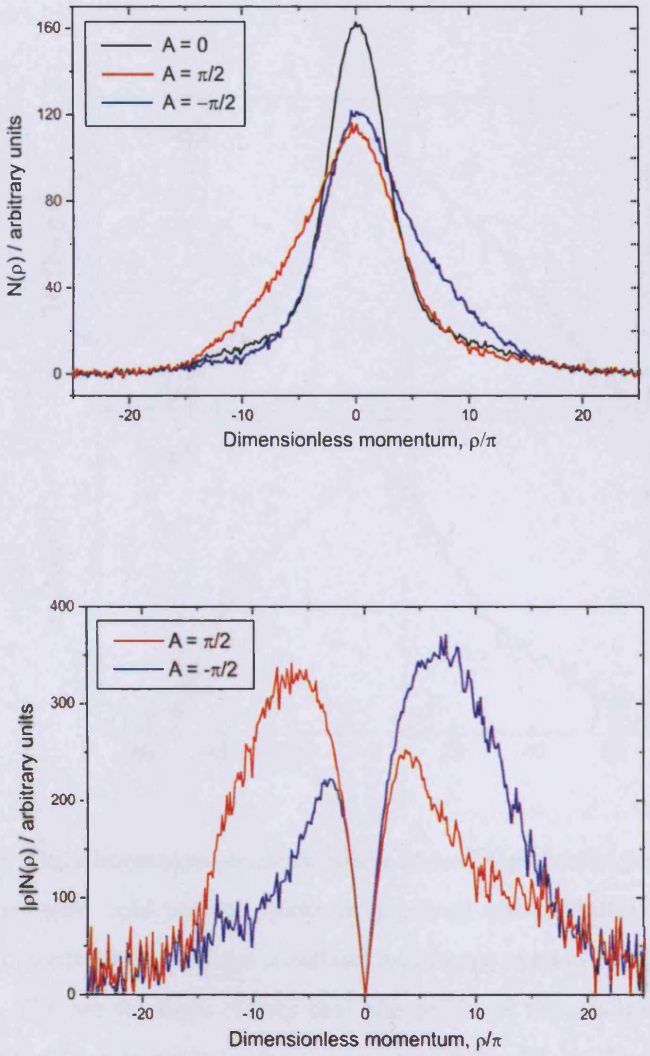

Figure 3.9: The top picture shows the effect of altering the rocking potential term A for K=2.6, a small perturbation of ϵ=1/16. The momentum distributions are is symmetric for A=0 but asymmetric for both $A = \pi/2$ and $-\pi/2$, causing opposite direction of transport. The bottom figure shows the first moment of the atomic momentum distribution $|\rho|N(\rho)$ for the momentum profiles above. The difference in magnitude of asymmetry for both $\pm A$ is almost equal. Courtesy of Goonasekera [63].

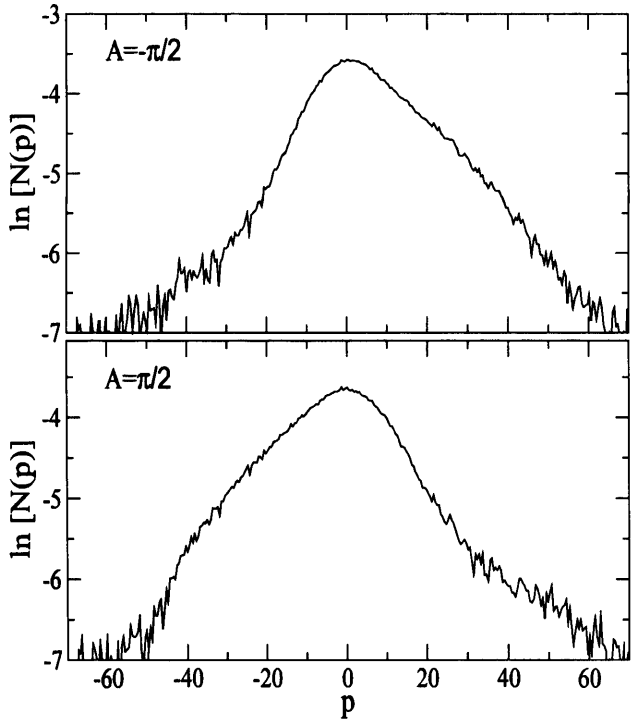

Figure 3.10: Experimental momentum distributions $N(p)$ for the perturbed-period KR obtained with cold cesium atoms in a pulsed optical lattice for $K = 2.6$, $\epsilon = 1/16$. The distributions have localised, and hence remain essentially constant with time. The results show clearly that the origin of the net non-zero value of $\langle p \rangle$ obtained at long times is in the asymmetry of the DL profiles. As expected, the asymmetry is also reversed by changing the sign of A, the amplitude of the rocking potential. Courtesy of Jones *et al* [64].

$-K^2 J_2(K)\cos(2p_0\epsilon - A)$. If we set $p_0 = 0$, as in the experiment, then for a very small momentum displacement δp, the differential absorption of energy for particles moving to the left $\delta p < 0$ or right $\delta p > 0$ is proportional to the gradient $\frac{\partial C_2}{\partial p_0} \propto K^2 \sin(2p_0\epsilon - A)$. An analytical form for the classical current was derived previously [43]. An asymptotic (small ϵ) approximation for the ratchet current is given by $I \simeq \frac{J_2(K)}{\epsilon} \sin(2p_0\epsilon - A)$, implying the maximal classical current is $I_{max} \sim \frac{J_2(K)}{\epsilon}$.

The results in Fig. 3.11 correspond to $K = 2.6$, $\epsilon = 1/16$ and $\hbar = 1$ (note that in re-scaled units $\hbar = 8\omega_R T$, where ω_R is the Rabi frequency). This effective value of Planck's constant may be varied: in the experiments, the range $\hbar \simeq 1/4 \rightarrow 1$ was investigated. For these values of K and ϵ, we estimate $I_{max} \sim \frac{J_2(K)}{\epsilon} \simeq 8$, about twice the observed value. This is not unreasonable as $\epsilon = 1/16$ is not so small and we neglect higher-order corrections to the classical current. The experiments in [45] indeed indicate that halving ϵ almost doubles the maximal current. Note that changing the sign of ϵ implies a current reversal.

Of course, it is clear that a non-zero and persistent constant ratchet-current is also obtained classically. It was found in [40] that asymmetric diffusion accumulates only on a timescale $t_r \sim 1/(K\epsilon)^2$ (termed the 'ratchet time' in [40]). Note that $I_{max} \sim \frac{J_2(K)}{\epsilon}$ implies that $I_{max} \rightarrow \infty$ as $\epsilon \rightarrow 0$ (see [43, 68]), but in that case $t_r \rightarrow \infty$ and so the final value of the current is never reached. (i.e., the ratchet effect requires both $\epsilon > 0$ and $A \neq 0$. Although $\epsilon \rightarrow 0$ seems to imply that a ratchet current will occur, the timescale for this to manifest goes to infinity and over finite timescales the current averages to zero.)

For the (unbounded) chaotic system studied here, the acquired momentum asymmetry is never lost. For a bounded ('compact phase-space') system,

such asymmetries would vanish on a long time-scale, since the distribution of a fully chaotic system would eventually become uniform. For this reason, until recently, it was argued that a fully chaotic system could not generate directed motion. So, although as shown in [40], the fully chaotic classical system can keep a constant current for long times, practical implementation is less interesting since the average kinetic energy of the ensemble grows linearly with time and without limit. Hence, this type of chaotic ratchet is of most interest as a *quantum* rather than a *classical* ratchet since in the quantum case DL halts the diffusion and 'freezes-in' the asymmetry, without the need for classical barriers like tori. Further investigation of the quantum perturbed-period KR was fulfilled by using Floquet states and is described in chapter 5.

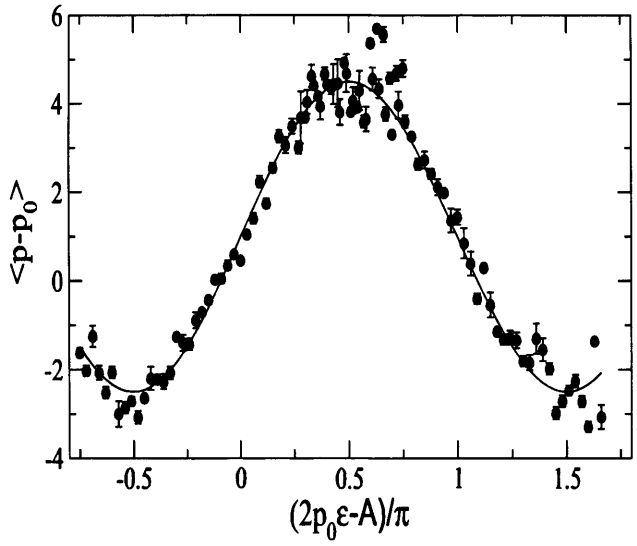

Figure 3.11: Experimental values of the momentum current $I = \langle p - p_0 \rangle$, for the perturbed-period KR, obtained with cold cesium atoms in a pulsed optical lattice for $K = 2.6$, $\epsilon = 1/16$. The solid line is a best-fit to the data, showing that the current oscillates sinusoidally as $I \propto \sin(2p_0\epsilon - A)$. Courtesy of Jones *et al* [45].

CHAPTER 4

2δ-KR and velocity selection

In this chapter, we use the term '2δ-KR' to describe the dynamics of a cloud of atoms experiencing a set of sinusoidal potential kicks in sequence of long-short time intervals. Alternatively, the atoms are kicked with pairs of closely spaced kicks. The main physical findings described here are a momentum trapping effect (and thus an enhanced momentum filtering effect) and a reversal of the energy absorption curve as the kicking strength, K, increases. Thus, this chapter includes:

- classical analysis in terms of long range correlations, and the experimental results
- quantum analysis, including DL with a staircase effect and a reversal of the energy absorption depending on the kicking strength, K
- discussion of the best conditions for velocity selection.

4.1 Classical dynamics

4.1.1 2δ-KR and classical mapping

In the previous chapter, we analysed the ratchet and filtering effect by introducing both a linear rocking term into the sinusoidal potential kick and a small perturbation into the kick separations in the standard δ kicked system. Here, we report on the extreme limit of changing the kick separation which has been termed the double δ-KR or 2δ-KR: a cloud of atoms is exposed to a periodic sequence of *pairs* of closely spaced kicks. As in the usual realisation of the δ-KR, an ensemble of particles initially evolving from initial momentum, p_0, is kicked periodically, with period T, by a sinusoidal potential given by

$$V(x,t) = K\cos x \sum_n [\delta(t-nT) + \delta(t-nT+\epsilon)] \tag{4.1}$$

The momenta of given particles change with time under the potential kicks, i.e., $\Delta p_N = \Sigma_{i=1}^{N} K \sin x_i$. The average energy of the ensemble initially grows diffusively; $< (p_N - p_0)^2 >=< (\Delta p_N)^2 >= DN$, where D is the momentum diffusion rate.

The diffusive behaviour was found to be remarkably different from that seen in the perturbed-period KR. It was shown in [43] that 2-kick correlations yield local corrections to the diffusion, D $\equiv D(p_0,t)$. However, we discovered new corrections for the 2δ-KR. These appear in families correlating all kicks. These corrections are individually very weak, but accumulate with time and become dominant after a long time. A brief description of the new correlations follow in the next section. It is instructive to consider a simple physical picture in order to understand how the trapping regions are produced. For particles for which $\pm p_0\epsilon = (2n+1)\pi, n = 0, 1, 2..$ experiencing

kicks of the form $-V'(x) = K \sin x$, consecutive kicks will be out of phase and will each cancel the previous kick. This cancellation means that particles become trapped at these momenta. Conversely, for $\pm\epsilon p_0 = 2n\pi$, a series of near identical kicks produces initially rapid energy growth. The following experimental results show good agreement. We begin the investigation of 2δ-KR with a classical analysis. The classical map of the 2δ-kicked particle system is given by iterations of the following equations:

$$\begin{aligned} x_{j+1} &= x_j + p_j\tau \\ p_{j+1} &= p_j + K \sin x_{j+1} \\ x_{j+2} &= x_{j+1} + p_{j+1}\epsilon \\ p_{j+2} &= p_{j+1} + K \sin x_{j+2} \end{aligned}$$

Here, unlike T_1 and T_2 in the perturbed-period KR, τ is $2 - \epsilon$, defined as the long interval between successive pairs of kicks, while ϵ is defined as the very short time interval between two kicks in a pair. Fig. 4.1 illustrates the surface of section for K=7, ϵ=0.05. It clearly shows the trapping regions for which the momenta $p\epsilon \simeq \pm(2n+1)\pi$, n=0, 1, 2...

4.2 Experimental results on the double kick system

Double kicks

As defined in the beginning of this chapter, the double kick system is a sequence of pair of kicks with a short time interval, ϵ in between and these pairs are separated by a long time interval $\tau = T - \epsilon \simeq T$. Experimentally,

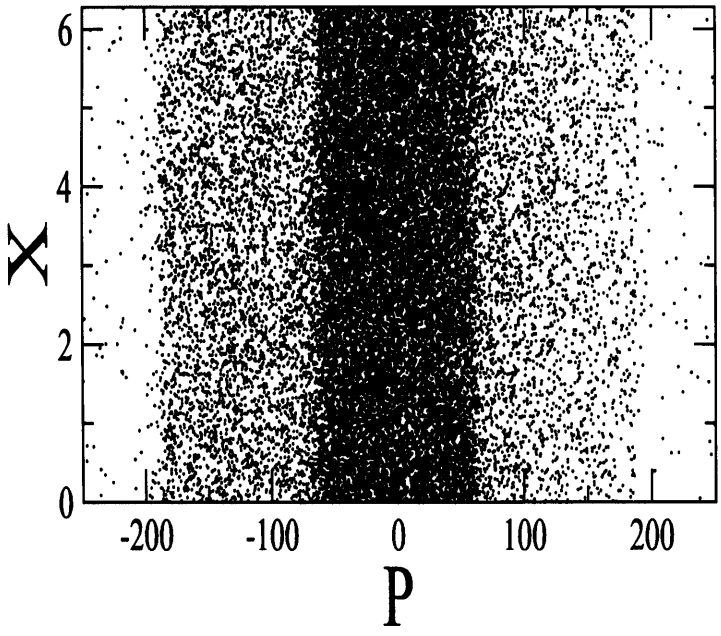

Figure 4.1: Classical surface of section for 2δ-KR, ϵ=0.05, K=7. A cloud of atoms is initially prepared with P=0. The sos demonstrates the trapping regions for which the momenta $p\epsilon \simeq \pm(2n+1)\pi$.

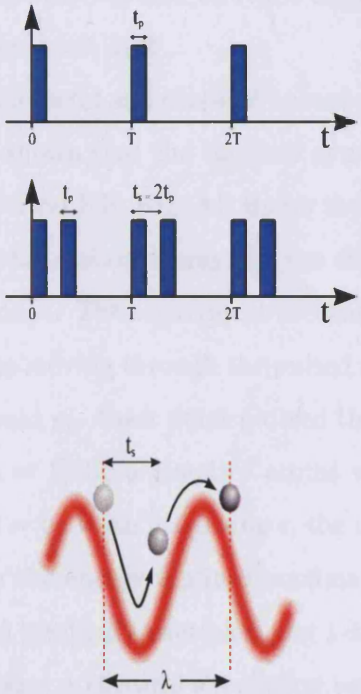

Figure 4.2: The top figure shows a 'double kicks' sequence. Pairs of pulses of duration t_p are separated by t_s and period $T \gg t_s$. The bottom figure shows a semi-classical picture of the atom motion in a 1-D potential. The atom moves a half wavelength $\lambda/2$ between kicks. The separation between kicks is t_s=$2t_p$. Thus, the combined kick strength of each pair gives zero over one period. Courtesy of Goonasekera [63]

instead of delta kicks, the pulses have a width of t_p and are separated by t_s. Fig. 4.2 is shown for the case of $t_s = 2t_p$. Then, the short time interval is achieved by making t_s/T small, i.e., $T \gg t_s$. Figure 4.2 shows that the first kick is cancelled by the following kick and this effect produces the trapping region at $p\epsilon = (2n+1)\pi$, n=0, 1, 2 ...

A study of the experimental and classical behaviour of the 2δ-KR was carried out in [57]. It was shown that the classical dynamics is very different to that of the perturbed-period KR. Fig. 4.3 shows the experimental results for the 2δ-KR realisation with cesium atoms and the classical energy absorption curves are superposed on it. The experiment measured the energy of a series of clouds of $\sim 10^6$ atoms moving through the pulsed optical lattice with varying average drift momenta p_0. Each point plotted the energy absorbed (after 100 kicks, $K = 3.3$, $\hbar = 1$) by a cloud of atoms with average momentum $\bar{p} = p_0$ at initial time, $t = 0$. With increasing ϵ, the minima corresponding to the trapping regions in the energy flip into maxima as a long-ranged family of classical correlations gradually overtakes the 1-kick classical correlation. The dashed lines represent a classical simulation using 100,000 particles, all with momenta p_0 at $t = 0$, and K within the range $3.3 \pm 10\%$. At very short times, the chaotic diffusion comprises an uncorrelated diffusion term $K^2/2$ and one dominant 1-kick correction. It was also found that one can approximate the growth in the mean energy with time t by the simple expression $\langle (p - p_0)^2 \rangle \simeq K^2 t[1 + \cos p_0 \epsilon]$ (see the next section). Fig. 4.3(a) shows the experimental results for cesium atoms which are localised in this regime of very short times. For Fig. 4.3(a), the simple expression given above gives an excellent fit to the experiment, if we take $t \sim t^*$, where t^* is the break-time. This regime corresponds to $t^* \ll 1/(K\epsilon)^2$.

However, a more detailed study of the classical correlations showed that

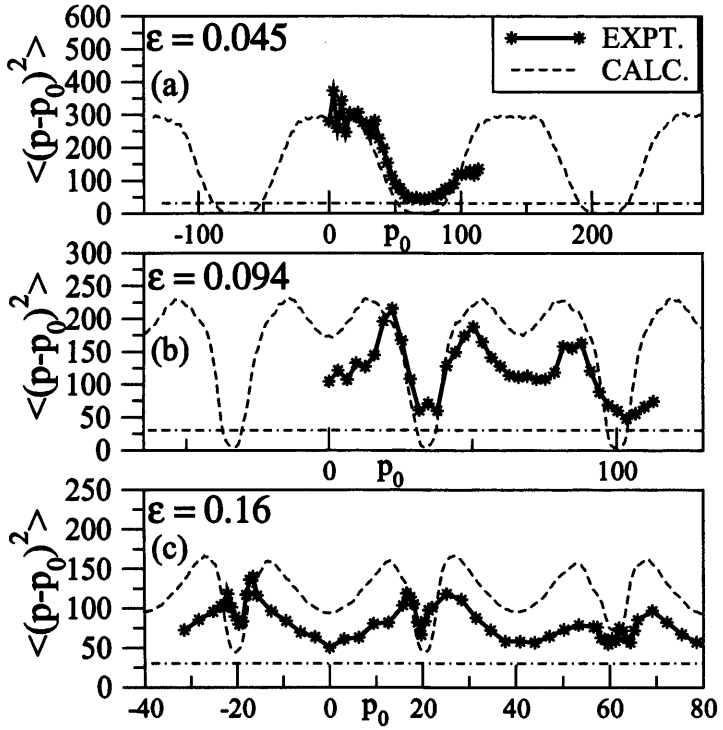

Figure 4.3: Experimental results for the 2δ-KR realisation with cesium atoms. Each data point (star) shows the energy absorbed (after 100 kicks, $K = 3.3$, $\hbar = 1$) by a cloud of atoms with average momentum $p = p_0$ (relative to the optical lattice) at initial time, $t = 0$. **(a)** shows the regime, $t^* \ll t_1 \simeq 1/(K\epsilon)^2$, where a one-kick correlation is the dominant correction to the classical diffusion. Here, atoms prepared near the trapping regions $p_0\epsilon \sim (2n+1)\pi$ remain trapped. **(b)** for the regime $t^* \sim 1/(K\epsilon)^2$ shows the inverted peaks of the Poisson correlation terms analysed in [57], which determine the momentum trapping very close to the resonant condition ($p_0\epsilon = (2n+1)\pi$). **(c)** shows the regime where $t^* > 1/(K\epsilon)^2$, dominated by correlation family C_{G1}, but sharp inverted peaks due to the Poisson correlations are still visible. Courtesy of Jones *et al* [66].

for later times, a new type of correction appeared. Families of long-ranged, or 'Global' correlations, which coupled *all* kicks, appeared. Here, new terms, Poisson family, C_1 and C_{G1} are mentioned briefly in order to describe the experimental results. Further mathematical description follows in the next section but full details can be found in [58, 59]. These corrections are individually very weak, but accumulate to eventually dominate the diffusive process. One family (termed the 'Poisson family' in [58]) was shown to lead to well-localised, inverted peaks in the energy absorption at values of $p_0 \simeq (2n+1)\pi/\epsilon$, where $n = 0, 1, 2....$ These values of p_0 correspond to trapping regions in phase-space. (At low values of K, structures corresponding to islands and broken phase-space barriers are evident.) However there is no need to investigate detailed transport through this complex mixed phase-space structure, as the correlations give us a generic and quantitative handle on the energy diffusion with time.

On the other hand, in the intermediate regime dominated by the Poisson correlations, atoms prepared outside the trapping regions rapidly diffuse across the regions between them, while particles prepared in the trapping regions remain there. This regime occurs for $t^* \sim 1/(K\epsilon)^2$ and corresponds approximately to the experimental results shown in Fig. 4.3(b).

Finally, at the longest timescales, the C_{G1} correction plays a very important role in energy diffusion. The C_{G1} correction arises from a long-ranged global-correlation family. C_{G1} results in an oscillation of the form $-\cos p_0\epsilon$ and becomes dominant at the longest timescales. The oscillation is of the same period as the 1-kick correlation, but is of *opposite* sign. This means that at the longest timescales, the minima in energy absorption shown in Fig. 4.3(a) become maxima in energy absorption; and vice-versa: the maxima become minima. Fig. 4.3(c) shows experiments tending towards this regime.

The inverted peaks of the Poisson family are still in evidence, but a $-\cos p_0\epsilon$ oscillation is clearly superposed. This is a somewhat counter-intuitive result since it implies that atoms initially prepared in the momentum trapping regions are the ones which at long times, for $t^* \gg 1/(K\epsilon)^2$, will absorb the most energy (there are no further reversals of this behaviour at even longer times).

More experimental results similar to Fig. 4.3 are shown in Fig. 4.4 and 4.5. Fig. 4.4 demonstrates the (experimental) energy absorption as a function of initial momentum by varying the short intervals ϵ between a pair of kicks. $t_s = 1.5t_p, 2t_p, 3t_p, 4t_p$ correspond to $\epsilon = 0.047, 0.063, 0.125, 0.156$ respectively. Figure 4.5 shows the current $< p >$ as a function of initial momentum for the corresponding values in Fig. 4.4. The characteristic sawtooth shape is clearly shown for $t_s = 4t_p$. As will be shown in the following section, this shape resembles the results from the quantum numerical calculation.

4.2.1 Mathematical analysis of long range correlations

Fig. 4.6 shows the comparison between the classical calculations at K=7, ϵ=0.05, with the analytical calculations from the formulae for the correlations in the diffusive process. As briefly mentioned in the previous section, three new correction terms are introduced to explain the behaviour observed in Fig. 4.3 and Fig. 4.6.

Mathematical analysis begins with considering the standard case. It is well known that for the standard map, to the lowest order of approximation, the classical diffusion at consecutive kicks is uncorrelated and evolves with time as a 'random walk'. It gives rise to the so called 'quasi-linear' approx-

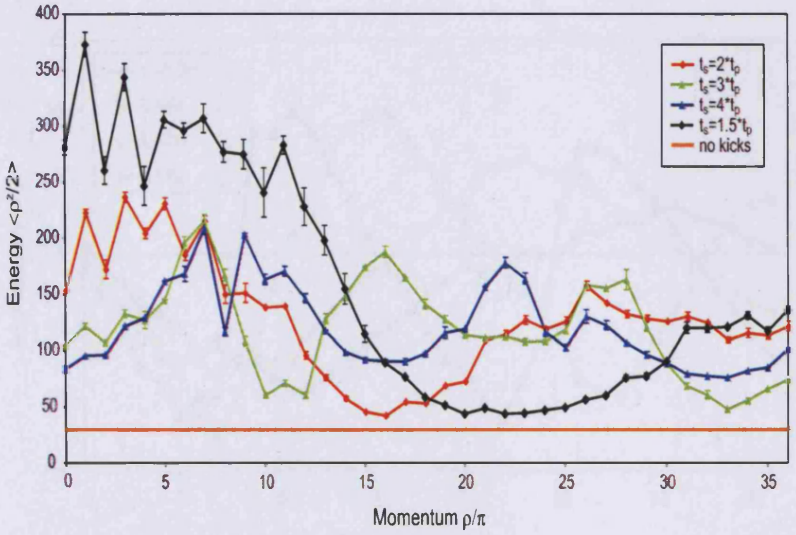

Figure 4.4: Experimental results of the energy absorption as a function of initial momentum for $\epsilon = 0.047$ ($t_s = 1.5t_p$), 0.063, 0.125, 0.156 ($t_s = 4t_p$). It shows that the position of the first minimum at $\rho \simeq \pi/\epsilon$ moves to lower ρ as ϵ increases. Courtesy of Goonasekera [63].

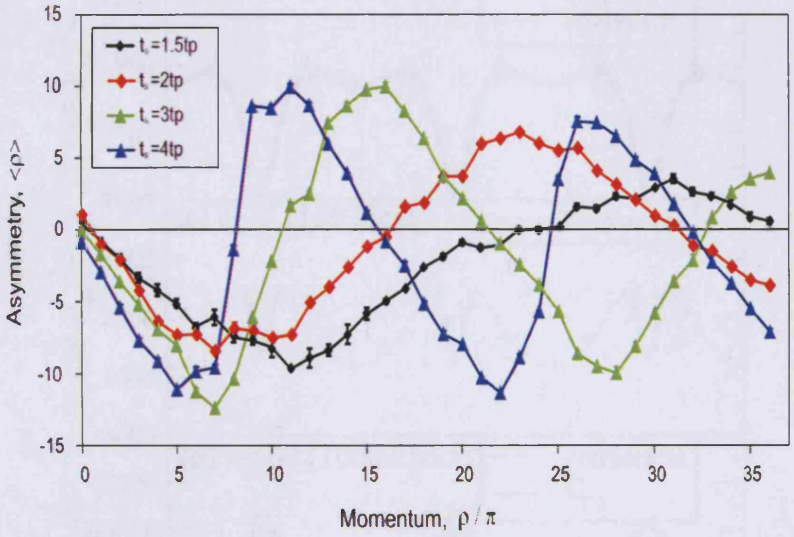

Figure 4.5: Experimental results of the momentum asymmetry as a function of initial momentum for corresponding values in Figure 4.4. Courtesy of Goonasekera [63].

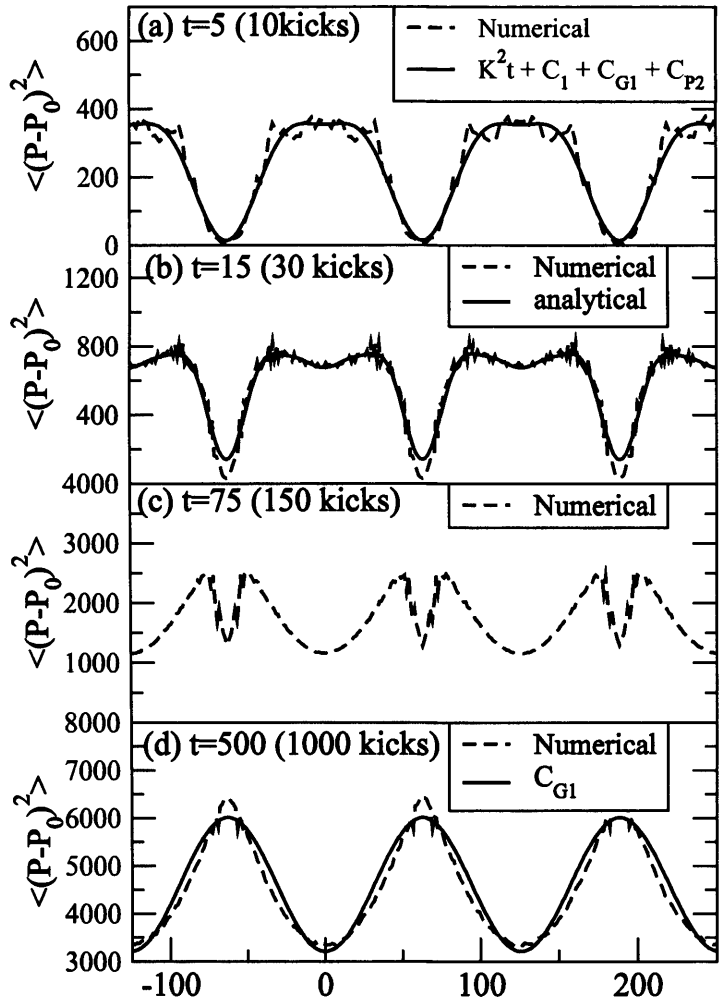

Figure 4.6: The figure was obtained from an ensemble of 10^5 classical particles initially evolving with $p = p_0$ at $t = 0$. The classical energy curves are calculated numerically (dashed lines) and superposed with analytical results obtained for the diffusion (solid lines). K=7, ϵ=0.05 are used in every figure but the number of kicks varies. Courtesy of Stocklin *et al* [58].

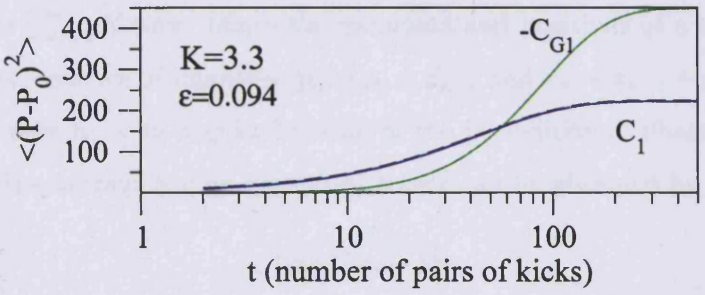

Figure 4.7: The figure shows that the kick-to-kick correction C_1 is overtaken by the global long-ranged correlation C_{G1} with an increasing number of kicks. At short times, C_1 grows linearly, while C_{G1} grows quadratically. Courtesy of Stocklin *et al* [58].

imation for the diffusion rate, $D_0 \simeq K^2/4$. However, correlations arising through the sequence of consecutive kicks give non trivial corrections to the diffusion rate. These corrections have been measured experimentally with cold cesium atoms in pulsed optical lattices [27]. The main correction to the standard map is the 2-kick correlation and was obtained by Rechester and White in 1980 [6].

The derivation of the classical diffusion rate for 2δ-KR was obtained by considering the corresponding derivation of the standard KR in [6, 7, 8]. To begin with, consider an ensemble of particles with the probability distribution $G(x_0, p_0, 0)$ at time t=0. A new probability distribution after time t is then given as $G(x_t, p_t, t)$, by following all the classical trajectories and noting that the standard map is 2π-periodic in position x.

$$\begin{aligned} G(x_t,p_t,t) &= \sum_{n_t=-\infty}^{\infty} \cdots \sum_{n_1=-\infty}^{\infty} \int_0^{2\pi} dx_0 dp_0 G(x_0,p_0,0) \int_0^{2\pi} dx_t \cdots \int_0^{2\pi} dx_1 \delta(p_t - p_0 - S_{t-1}) \\ &\times \delta(x_t - x_{t-1} - p_0 - S_{t-1} + 2\pi n_t) \cdots \delta(x_1 - x_0 - p_0 - S_0 + 2\pi n_1) \end{aligned} \tag{4.2}$$

where $S_l = \sum_{j=0}^{l} K \sin x_j$ (since the momenta and positions of a trajectory evolve by a sequence of impulses: $p_n = p_0 + S_{n-1}$ and $x_n = x_{n-1} + p_0 + S_{n-1}$. The sums over $n_1 \cdots n_t$ appear because of the periodicity of phase space in $x_1 \cdots x_t$. The average energy growth at time t can be obtained by

$$< (\Delta p_t)^2 >= Dt, \tag{4.3}$$

where D is given by

$$D = \lim_{t\to\infty} \frac{1}{t} < (p_t - p_0)^2 >, \tag{4.4}$$

and hence

$$< (\Delta p_t)^2 >= \int_0^{2\pi} dx_t \int_{-\infty}^{\infty} dp_t G(x_t, p_t, t)(p_t - p_0)^2. \tag{4.5}$$

The initial condition is taken as $G(x_0, p_0, 0) = \frac{1}{2\pi}\delta(p - p_0)$ and using the Poisson sum formula (the Fourier transform), $\sum_n \delta(y + 2\pi n) = \frac{1}{2\pi}\sum_m e^{imy}$, D can be written as

$$D = \lim_{t\to\infty} \frac{1}{t} \sum_{m_t=-\infty}^{\infty} \cdots \sum_{m_1=-\infty}^{\infty} \prod_{i=0}^{t} \int_0^{2\pi} \frac{dx_i}{2\pi} (S_{t-1})^2 \exp \sum_{j=1}^{t} im_j(x_j - x_{j-1} - p_0 - S_{j-1}) \tag{4.6}$$

For the 2δ-KR, the evolution of momentum is in terms of pairs of kicks, S takes on the form $S_t^{(2)} = \sum_{m=1}^{t} \sum_{r=1}^{2} K \sin x_m^{(r)}$. The superscripts (1) and (2) indicate the first and second kick in the pair and t denotes the number of pairs of kicks. For the final momentum distribution at the second kick in the jth pair, D becomes

$$\begin{aligned} < (\Delta p_t)^2 >= & \sum_{m_t^{(1,2)}=-\infty}^{\infty} \cdots \sum_{m_1^{(1,2)}=-\infty}^{\infty} \int_0^{2\pi} \frac{dx_t^{(1,2)}}{2\pi} \cdots \int_0^{2\pi} \frac{dx_1^{(1,2)}}{2\pi} \\ & \times (S_t^{(2)}) \prod_{j=1}^{t} e^{im_j^{(2)}[x_j^{(2)} - x_j^{(1)} - \epsilon(p_0 + S_j^{(1)})]} e^{im_j^{(1)}[x_j^{(1)} - x_j^{(2)} - \tau(p_0 + S_{j-1}^{(2)})]} \end{aligned} \tag{4.7}$$

Significant contributions to the classical diffusion rate are only obtained from $|m_j| = 1$ (or $m_j = \pm 1$) in Eqn. 4.7. The 1-kick correlation C_1 is obtained by setting any one of the $m_j^{(2)} = \pm 1$ (all others are zero): for $m_j^{(2)} = \pm 1$ the correlation involves $\cos p_0 \epsilon$ and Bessel functions of argument $K\epsilon$ while for $m_j^{(1)} = \pm 1$ the correlation involves $\cos p_0 \tau$ and Bessel functions of argument $K\tau$. As $\tau \gg \epsilon$, the latter case results both in a decaying J_0 summation and fast oscillations with p_0. Thus, it is reasonable to set all $m_j^{(1)} = 0$. Now we consider the $2K^2 \sin x_j^{(2)} \sin x_j^{(1)}$ term in $(S_t^{(2)})^2 = K^2 \Sigma_{i,j} \sin x_i \sin x_j$. Then C_1 is given by:

$$C_1(p_0, t) = K^2 \cos p_0 \epsilon [J_0(K\epsilon) - J_2(K\epsilon)] \times \sum_{j=1}^{t} (J_0(K\epsilon))^{2j-2} \qquad (4.8)$$

This correction was neglected for the standard map and all other previously studied δ-kicked systems but is now important for the 2δ-KR. It should be emphasised that C_1 is a function of t, ϵ and K but is *independent* of τ (as will be shown in the next section). For short times, C_1 grows linearly with time and saturates after a time, $t \sim \frac{10}{(K\epsilon)^2}$. Therefore, for short times it can be approximated to $C_1 \simeq K^2 t \cos p_0 \epsilon$.

However, both the experiment and the numerical calculation show the reversal of this energy diffusion at long times. It is found that this reversal is due to new 'Global' correlation terms, which appear in families correlating all kicks. Each correlation is individually weak but many such terms of equal strength accumulates with time and eventually the global correlation becomes dominant at long times. This new correction can be obtained by setting $m_j^{(2)} = \pm 1$ once again but considering all the correction terms $2K^2 \Sigma_{j,i} \sin x_j^{(2)} \sin x_i^{(r)}$ in the $(S_t^{(2)})^2$ summation (r=1, 2, $i < j$ but otherwise arbitrary). As a result, the net contribution of this 'Global' correlation

family is (see [58, 59])

$$C_{G1}(p_0,t) = -2K^2 \cos p_0\epsilon J_1^2(K\epsilon) \times \sum_{j=1}^{t}(2j-2)(J_0(K\epsilon))^{2j-3} \qquad (4.9)$$

$2j-2$ indicates the number of kicks up to $j-1$ pairs which precede the jth kick pair. Each term, representing the correlation between the second kick in the jth pair and a kick in any preceding pair, is negligible compared to C_1, but C_{G1} increases quadratically with time and saturates to a value almost twice that of C_1 at long times (see Fig. 4.7). Note that C_{G1} is of opposite sign to C_1, implying the gradual dephasing of the resonant effects of C_1 at $p_0\epsilon \sim (2n+1)\pi$, n=1, 2... Thus, the energy absorption is maximal for particles initially prepared at $p_0\epsilon \simeq \pm(2n+1)\pi$ at long times.

An interesting regime is shown in Fig. 4.6 (b), where $C_1 \sim C_{G1}$. Most of the $\cos p_0\epsilon$ correction is cancelled and a series of narrow dips is exposed in the energy curve. These dips originate from the Poisson sum formula for cosine terms $\Sigma_n(-1)^n \cos np_0\epsilon = \Sigma_m \delta(p_0\epsilon - (2m+1)\pi)$, which yields peaks at these momenta. The Poisson terms are obtained by setting more than one $m_j^{(2)}$ coefficient to ± 1. These terms come in two families analogous to C_1 and C_{G1}, depending on which type of sine product is considered.

$$C_{pn}(p_0,t) \propto K^2 \cos(np_0\epsilon)F_n(t)\prod_m J_1^2(mK\epsilon). \qquad (4.10)$$

$F_n(t)$ is a time function which grows as $\sim t^n$ for C_{pn} and $\sim t^{n+1}$ for C_{pn}^G. For each individual Poisson term, the limits on m depend on the values of n and m_j (see [59]). In general, for every order n, the 'Global' type C_{pn}^G terms eventually become more dominant than their regular Poisson partners, but as n increases, the terms become less significant. It is important to mention that at the same order, C_{pn} and C_{pn}^G are always of opposite sign and these signs

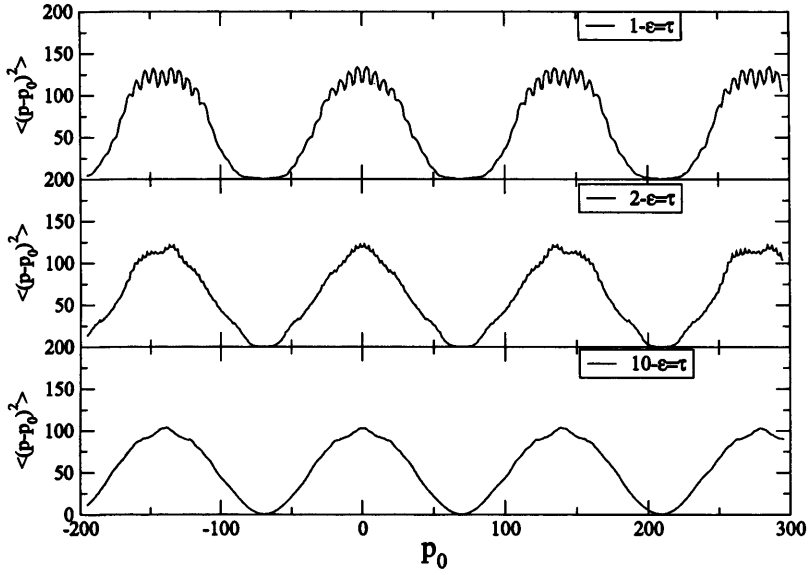

Figure 4.8: The figure demonstrates the insensitivity of the classical diffusion to the value of τ. All three plots have the same period, $2\pi/\epsilon \simeq 68$. Parameters used are K=3.3, $\hbar$=1. 10 pairs of kicks are applied.

alternate with increasing orders, as predicted by the Poisson sum formula. For each n, the global correlation always dominates at long times. For the full mathematical details, see [58, 59].

4.2.2 Insensitivity of τ

Some numerical simulations were conducted by changing the value of τ in the regime where $t^* \ll 1/(K\epsilon)^2$ (C_1 correction dominates). Figure 4.8 demonstrates the insensitivity of the classical diffusion to the value of τ. As mentioned in the previous section, any τ dependent correlations are negligible in the correction terms. The values of τ in Fig. 4.8 are $1-\epsilon$, $2-\epsilon$ and $10-\epsilon$, where ϵ=0.045. It is clearly seen that the changes are of order $\sim 10\%$. τ acts

as a randomising term and so it is important that $\tau \gg \epsilon$. Its actual value is not important in our system.

4.3 Quantum numerical results corresponding to experiments

The classical analysis revealed that there are three distinct classical diffusive regimes occurring at three timescales. It is expected that the corresponding *quantum* behaviour will depend on which regime is dominant when dynamical localisation arrests the quantum momentum diffusion. In this section, we display some plots obtained by quantum numerical calculations.

As predicted, they show the same behaviour as seen in classical dynamics. Two plots in Fig. 4.9 show the average energy spread (top) and the corresponding current (bottom) along with initial momentum, p_0. Parameters used are K=15, $\hbar$=1, ϵ=0.05 and the number of kick pairs varies. The panels from top to bottom in each plot are obtained with 5 pairs, 15 pairs and 1,000 pairs of kicks respectively. In the top (a), the trapping regions are noticeable at $p_0\epsilon = \pm(2n+1)\pi$ where n=0, 1, 2... As the number of kicks increases, the energy absorption becomes faster in those trapping regions than those regions at $p_0\epsilon = \pm 2n\pi$, which are maximal at short times (5 pairs of kicks) and eventually reversed after many kicks (1,000 kick pairs in the figure), i.e. it follows the same trend as the classical behaviour. The bottom graph shows the corresponding current in saw-tooth shape, and it is clearly seen that the magnitude of current becomes bigger as the number of kicks increases. The same behaviour is seen in Fig. 4.10 with the same parameters of $\hbar$=1, ϵ=0.05 but, instead of the number of kicks, the kick strength K, now,

varies over 3, 7 and 15 respectively. The explanation can be found in [58]: for the double kicked system, the new correction terms are taken into account, which yield $< (p - p_0)^2 >= K^2 t + C_1 + C_{G1} + C_{p2}$ and each correction term gives a different contribution associated with $t^* \sim 1/(K\epsilon)^2$. In addition, we can see the current changes dramatically in Fig. 4.10 from (a) to (c). This is proportional to the changes in the energy absorption, $< (p - p_0)^2 >$.

4.3.1 Dynamical localisation for the 2δ-KR

Like the dynamical localisation for the perturbed-period KR described shown in chapter 3, the momentum distribution for the 2δ-KR is frozen in momentum space after break-time t^*. But here, a 'staircase' effect is observed due to the trapping effect, which means that the system initially diffuses rapidly until it reaches a momentum-trapping region $P_n = (2n+1)/\epsilon$ and slows down. After escaping from this region, diffusion speeds up again until it encounters the next trap. Figure 4.11 clearly shows this effect.

As $\hbar$ is increased, the height of the steps increases. Therefore, transport through the trapping barriers becomes more difficult. Fig. 4.12 shows the relation between $\hbar$ and the step size. To a good approximation, the step-size, denoted as $2d$, can be considered as a measure of the localisation length since $N(p) \sim \exp(-|p|/\ell)$, where ℓ (here) is localisation length. Looking at Fig. 4.11, the localisation length can be estimated by dividing a period of $2\pi/\epsilon$ (the width of one step) by the step-size $2d$ (step-height). Thus, we have $2d \sim 1/\ell$ (more details follow in chapter 6). Our numerical calculation found that the step-height $2d$ behaves as a power law: $2d \propto \hbar^{-3/4}$. This differs from the case of single kicks where L $\propto \hbar^{-1}$ [69]. This staircase effect due to the trapping regions led us to probe a new spectral behaviour in energy level

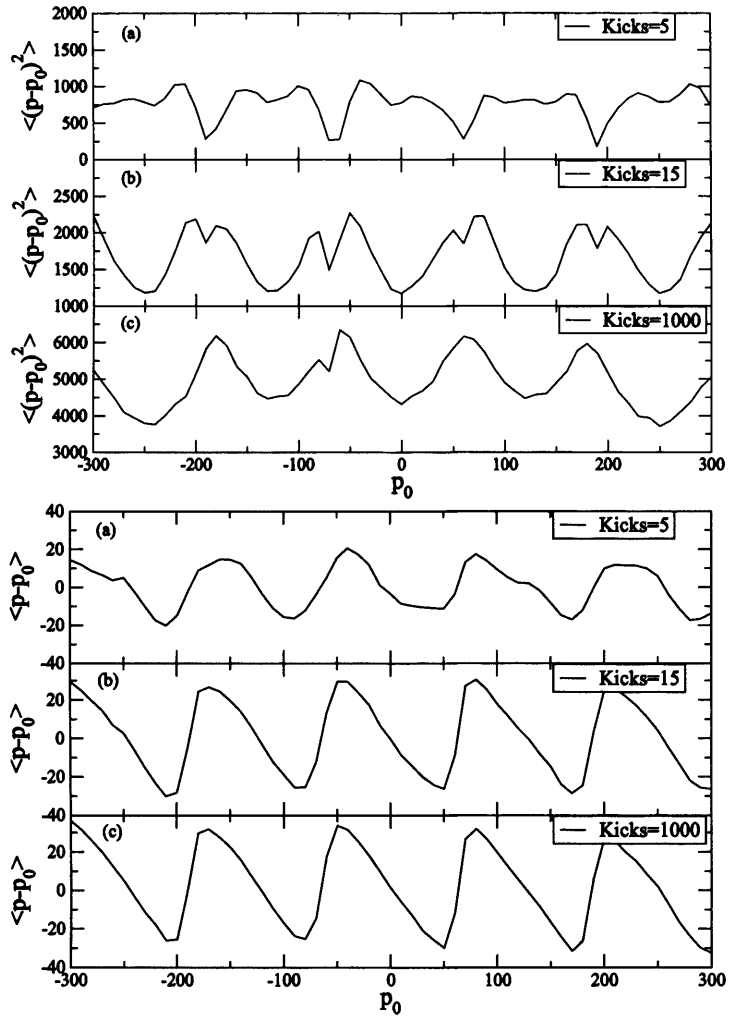

Figure 4.9: Energy absorption and current graphs as a function of initial momentum: K=15, $\hbar$=1, ϵ=0.05 are used in each figure, but the number of kick pairs is different, from 5 to 1,000 kick pairs.

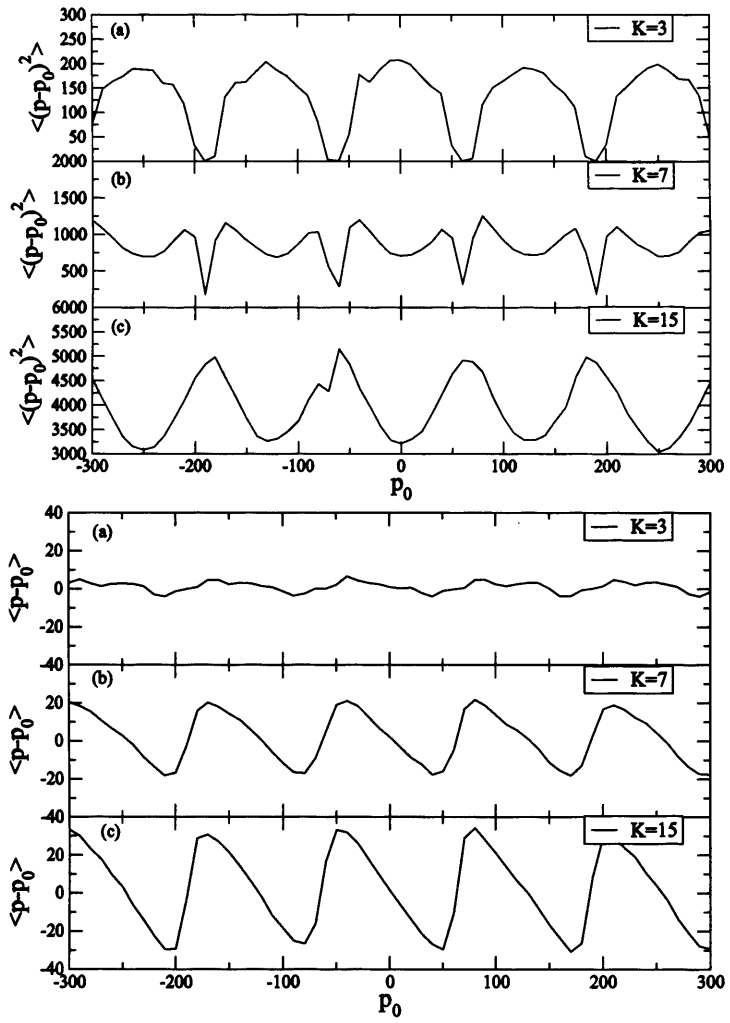

Figure 4.10: Energy absorption and current graphs as a function of initial momentum: $\hbar$=1, ϵ=0.05. The number of kick pairs=150 are used in each figure but the kick strength, K varies with 3, 7 and 15 respectively.

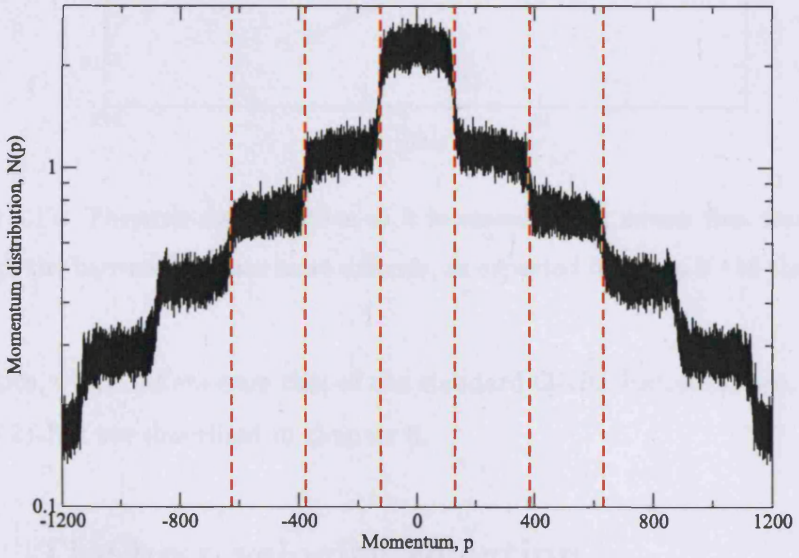

Figure 4.11: Dynamical localisation for the 2δ kick system shows the 'staircase' effect. System parameters are K=14, $\hbar$=0.045, ϵ=0.025.

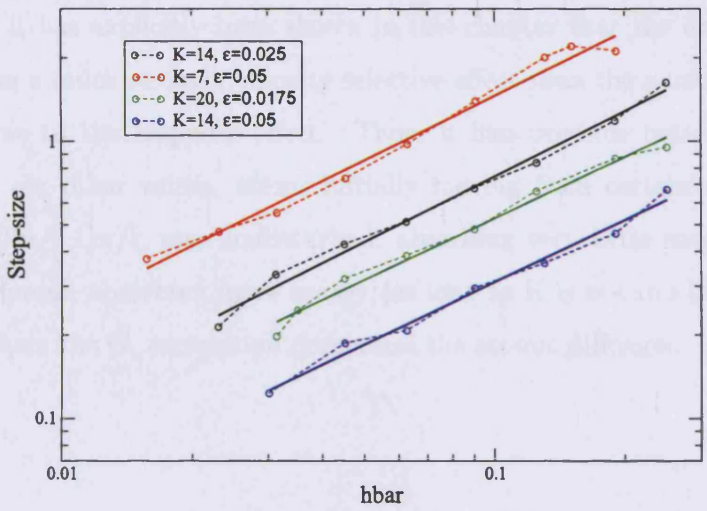

Figure 4.12: The step size increases as $\hbar$ increases. This means that transport through the barriers becomes more difficult, as expected from the KAM theorem.

statistics, which differs from that of the standard QKR. Statistical properties of the 2δ-KR are described in chapter 6.

4.4 The best velocity selection

The conditions for the best velocity selection can be summarised on the basis of analysis from chapters 3 and 4. In chapter 3, a ratchet effect was proposed by introducing a rocking term, $A = \pm\pi/2$ into the perturbed-period KR. This causes two wave packets, initially evolving from $p_0 = \pm\pi/4\epsilon$ to experience different local diffusion constants, dependent on local momentum, producing a sinusoidal dependence on the initial momentum. Thus, the perturbed-period KR system can be used for filtering the momenta of cold atoms in the context of atomic manipulation, such as the 'atomic chips' in [49, 50].

However, it has explicitly been shown in this chapter that the double kick system has a much stronger velocity selective effect than the perturbed kick system due to the trapping effect. Thus, it can produce better velocity selection. In other words, atoms initially moving from certain momenta, $\simeq p_0 = (2n+1)\pi/\epsilon$, pass undisturbed, absorbing very little energy, while others disperse, absorbing more energy (as long as K is not too big), in the regime where the C_1 correlation dominates the atomic diffusion.

CHAPTER 5

Floquet properties

This chapter describes the Floquet theory and the properties of the Floquet states of two systems described in chapters 3 and 4. As will be seen, Floquet analysis provides much insight into the observed ratchet current and variations in the dynamical localisation length. This chapter consists of two main sections: introduction of Floquet theorem and the Floquet properties of the two systems. Hence, the contents of this chapter are:

- Floquet theorem and operator
- Floquet properties of the perturbed-period KR
- local break time obtained from the mean level energy spacing, Δ, versus average momentum $< p >$
- Floquet properties of the 2δ-KR
- effect of altering kicking sequence in the 2δ-KR.

5.1 The Floquet theorem

As we consider the case where the Hamiltonian varies periodically with time, we can apply Floquet theory to its analysis. The Floquet theorem is a temporal version of the Bloch theorem in solid state physics, where the spatial periodicity of the crystal lattice leads to a corresponding relation for the spatial wave function in terms of Bloch states. Details are given below.

To begin with, take the time dependent Schrödinger Equation which is given by

$$i\hbar\frac{\partial\psi(x,t)}{\partial t} = H(x,t)\psi(x,t) \tag{5.1}$$

where the Hamiltonian, H, has a periodic time dependence, $H(t) = H_0+V(t)$ with $V(t+T) = V(t)$. Since H depends on time in each period, the eigenvectors of the system do not have trivial time dependence. It is generally known that when H depends on time, it is not possible to solve the Schrödinger Equation by means of the separation ansatz

$$\psi_n(x,t) = \exp(-\frac{iE_nt}{\hbar})\psi_n(x). \tag{5.2}$$

Although the energy in the time-dependent system is not constant, the Hamiltonian is still invariant against discrete time shifts, T. This means that eigenfunctions of the Schrödinger Equation within each period transform under time translations as

$$\psi_n(x,t+T) = \lambda_n\psi_n(x,t) \tag{5.3}$$

For the solution to be stationary, λ_n must be a pure phase factor.

$$\psi_n(x,t+T) = e^{-i\phi_n}\psi_n(x,t) \tag{5.4}$$

Then, $\psi_n(x,t)$ can be written as

$$\psi_n(x,t) = e^{-i\omega_n t} u_n(x,t), \tag{5.5}$$

where $u_n(x,t)$ is periodic in time, i.e. $u_n(x,t+T) = u_n(x,t)$ and $\omega_n = \phi_n/T$. Hence, by analogy with conservative systems, the quantity $\varepsilon_n = \hbar\omega_n = \frac{\hbar}{T}\phi_n$ can be termed the 'quasi energy'. (For simplicity, in chapter 6 we refer to the ϕ_n as the quasi energy.) They are not exactly the energy levels of the system - the $|u_n>$ are not stationary states of the time evolution, but are periodic - and are called quasi-energy levels. As the Floquet phase ϕ_n is defined only up to integer multiples of 2π, quasi energies are defined only up to integer multiples of h/T.

5.1.1 The Floquet operator

The time evolution operator $U(t)$ can be defined by the following equation

$$\psi(x,t) = U(t)\psi(x,0) \tag{5.6}$$

In the time dependent Schrödinger Equation

$$i\hbar\frac{\partial\psi}{\partial t} = H\psi \tag{5.7}$$

if the Hamiltonian, H, is Hermitian as in our systems, U is unitary, i.e. $U^\dagger U = 1$, hence, if the initial condition is $U(0) = 1$, with $t = T$, $\psi(x,T) = U(T)\psi(x,0)$. So it can be generalised to

$$\psi(x,nT) = [U(T)]^n\psi(x,0) \tag{5.8}$$

$$U(nT) = [U(T)]^n \tag{5.9}$$

It is reasonable to say that the $U(T)$ gives sufficient knowledge for a stroboscopic observation of the system at times nT, where n=0, 1, 2... Thus

the study of periodic systems reduces to the study of the eigenstate of $U(T)$. Eigenstates of $U(T)$ are also eigenstates of the Floquet operator, $\mathcal{H}^{\mathcal{F}}=(H - i\hbar\frac{\partial}{\partial t})$. The Floquet states provide a complete basis. If a quantum state is initially expanded in a plane wave basis, it can subsequently be evolved for each consecutive time-period by the time evolution matrix $U(T)$. Under the condition in which H is periodic in time, $H(t + nT) = H(t)$, a general quantum state can be expressed as

$$\Psi(t) = \sum_n C_n e^{-i\varepsilon_n t/\hbar} u_n(t) \tag{5.10}$$

where C_n are time-independent expansion coefficients and $u_n(t)$ are described as the Floquet states with period of T. It is clear from this expression that the Floquet states and quasi-energies, ε_n, play a similar role for periodically-driven systems to that of energy eigenstates and eigenvalues in the time-independent case. In other words, the eigenvectors of the operator $U(T)$ are Floquet states, and its eigenvalues are related to quasi-energy via $\lambda_n = e^{-i\varepsilon_n T/\hbar}$. The eigenvalues give simple phase shifts which can be obtained by diagonalising the matrix form in the plane-wave basis.

For the QKR, the operator is given by

$$U(T, 0) = e^{-iTp^2/2\hbar} e^{-iK\sin x/\hbar} \tag{5.11}$$

Using a basis of plane wave states, the matrix-elements of this operator can be shown to be

$$U_{m,n}(T, 0) = e^{-iT(m+q)^2\hbar/2} J_{|m-n|}\left(\frac{K}{\hbar}\right) \tag{5.12}$$

where q is the quasi-momentum ($p = (m+q)\hbar$) and J_n is the nth Bessel function of the first kind. It is useful to note that the $J_{|m-n|}(x)$ decreases very rapidly with increasing $|m - n|$ (i.e. $J \sim 0$ if $|m - n| \geq x$), thus giving U an

effectively banded structure. As the system considered here has unequal kicking in one period, the single-period operator can be expressed as the product of two matrices of this form, $U(T,0) = U(T_1+T_2,T_1)U(T_1,0)$, where T_1 and T_2 are the two kick-periods (see also previous section for quantum wave packet evolution operator). We employed a numerical algorithm suitable for banded Hermitian matrices: it can be used to obtain the spectrum of a unitary matrix U by applying it to $H^+ = \frac{1}{2}(U+U^\dagger)$ and $H^- = \frac{1}{2i}(U-U^\dagger)$, where both H^+ and H^- are Hermitian. Then, for the eigenvalues $e^{i\omega}$ of $U(T)$, the eigenvalues of H^+ and H^- are $\cos\omega$ and $\sin\omega$, respectively [51, 52].

5.2 Floquet properties of the perturbed-period KR

5.2.1 Distribution of Floquet states

Having obtained the Floquet states by diagonalising $U(T)$, it now becomes possible to study their properties, particularly the degree of spread in momentum space. This can be done by evaluating the localisation length, L, of each Floquet state. This is in general time dependent. But the time dependence is weak for this perturbed-period KR and we use the initial value (t=0). We shall, however, see a counter-example for the case of the 2δ-KR in the next section. Inasmuch as the Floquet states are not generally exponentially localised in momentum except the standard case, their localisation lengths are calculated by the root mean square deviation from the mean $\sigma_n = \sqrt{< p^2 >_n - < p >_n^2}$ where $< p >_n = \bar{p}_n$ is the mean momentum of the nth Floquet state at $t = 0$, $\bar{p}_n =< \psi(0)|p|\psi(0) >$, and $\overline{p_n^2} =< \psi(0)|p^2|\psi(0) >$. For numerical convenience, we introduce a small but non-zero A in Fig. 5.1

(a), (b) in order to break the spatial symmetry of the eigenstates in momentum space. In the ratchet, the momentum symmetry is broken by having $A = \pi/2$. In other cases, we used $A \simeq 0.01\pi$ to split the symmetry-related pairs of eigenstates.

In Fig. 5.1, we compare the localisation lengths for the standard QKR with those of the perturbed-period KR for $K = 3.4$, $\epsilon = 0.01$. The difference is quite striking; while the standard QKR eigenstates are quite uniform across all regions of phase-space, the perturbed-period localisation lengths oscillate sinusoidally with $\overline{p}$, with a period of π/ϵ. Introducing the additional rocking potential with the accelerated lattice ($A = -\pi/2$) clearly leads to a $\pi/2$ shift in the oscillations. Inspecting Fig. 5.1(c) for $\overline{p} \simeq 0$, we see that at positive momentum $< p > \simeq 78.5$, the localisation lengths L are maximal, while at negative momentum $< p > \simeq -78.5$, the localisation lengths L are minimal. Note the nearly regular row of states for the standard QKR case with $L \simeq 1$. These correspond to states localised on a series of stable islands separated by 2π, due to the momentum periodicity of phase-space in that case.

We chose a parameter range for which $L \ll \pi/\epsilon$: that is, the localisation length of each state is much smaller than the oscillation in $\overline{p}$. Hence, individual Floquet states really do sample 'local' diffusion rates. It is found that if a regime changes to the range where $L \sim \pi/\epsilon$, the conclusions remain valid, but the amplitude of the oscillations is considerably damped. Similarly, if the sign of $J_2(K)$ in the 2-kick correction term changes, so does the sign of the sinusoidal oscillation. Since the asymmetric diffusion term is $2J_2(K)\cos(2p_0\epsilon - A)$, the value K=5, where $J_2(5) \simeq 0$, does not produce asymmetry.

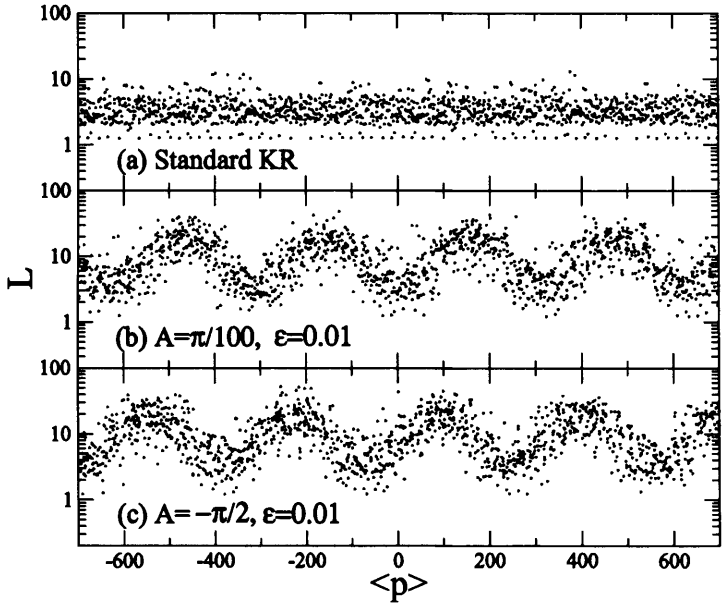

Figure 5.1: The graph shows the localisation lengths L of Floquet states as a function of average momentum $\bar{p}$ (i.e. $\langle p \rangle$) for $K = 3.4$, $\hbar$=1. Results are shown (a) for the standard QKR case, i.e. $A = 0.01\pi$ (a non-zero A was used to break spatial symmetry), $\epsilon = 0$, (b) for $\epsilon = 0.01$, $A = 0.01\pi$ and (c) $\epsilon = 0.01$, $A = -\pi/2$. The graph shows that for the standard kicked rotor the L are distributed within a narrow range in comparison with the other two below. For the rocking case, L oscillates with $\bar{p}$ as expected from the 2-kick correction $2J_2(K)\cos(2p_0\epsilon - A)$; the oscillations of the two lower graphs are shifted relative to each other by a phase $\pi/2$. The density of eigenstates corresponding to average momentum range is roughly the same in all three cases.

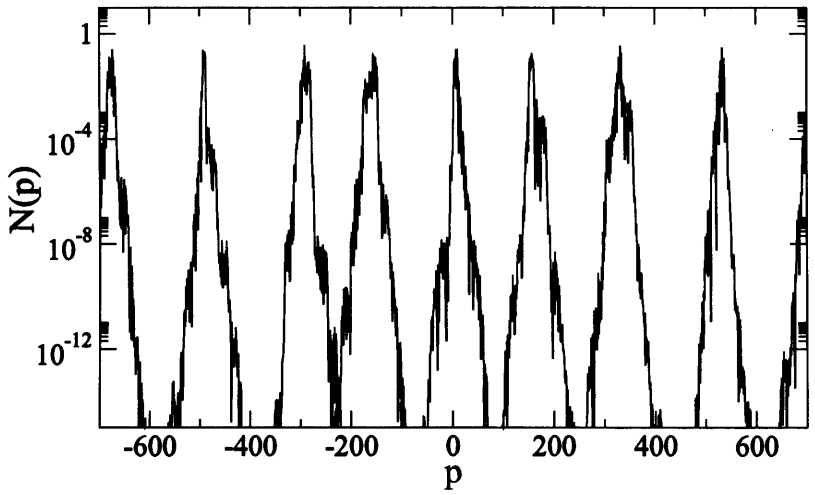

Figure 5.2: Floquet states for the standard QKR, for $K = 3.4$, $\hbar = 1$. As expected, all the states are exponentially localised, giving the characteristic triangular shape of $N(p)$ when plotted on a logarithmic scale. They all have approximately similar localisation lengths.

5.2.2 Floquet states for the perturbed-period KR

We now turn to consider the shape of the Floquet states in detail. Two figures, Fig. 5.2 and 5.3, are presented here. Fig. 5.2 shows the momentum distributions $N(p) = |\psi_n(p)|^2$ for Floquet states of the standard QKR. The distributions (with $N(p)$ on a logarithmic scale) all show the well-known triangular form [1]; the hallmark of dynamical localisation. It may be clearly seen that the localisation lengths vary little from state to state.

In Fig. 5.3, by contrast, the localisation lengths of the Floquet states of the perturbed-period δ-KR display a strong dependence on the mean momentum of the states. Those Floquet states presented are chosen from the Fig. 5.1, which is for the ratchet case; a wave packet evolving with initially

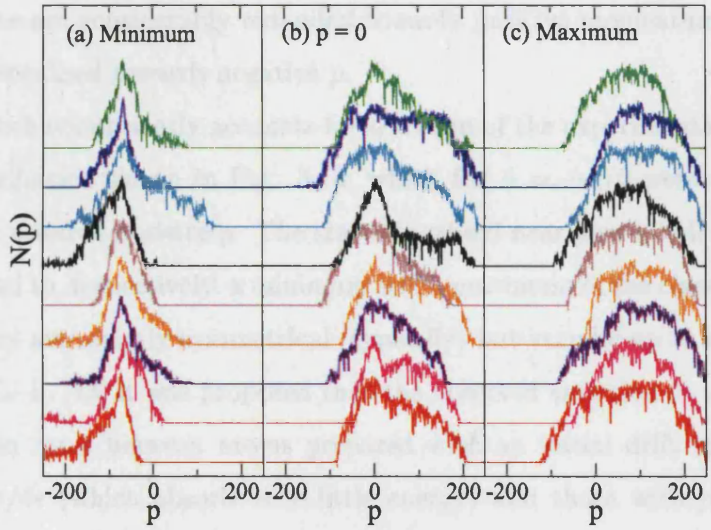

Figure 5.3: Typical form of Floquet states for the perturbed-period KR, $K = 3.4$, $\epsilon = 0.01$, $A = -\pi/2$ and $\hbar$=1. Here, we plot $N(p) = |\psi_n(p)|^2$ as a function of p. Each 9 Floquet states are chosen from Fig. 5.1(c); the Floquet states in (a), (b), (c) were chosen from those Floquet states at $< p > \simeq -78.5, 0, 78.5$ respectively. Those Floquet states are shifted along the y axis and displayed on a logarithmic scale. (a) states with $p \simeq -78$. This corresponds to a minimum of the 2-kick correction $-\cos(2p_0\epsilon + \pi/2)$. The states are narrow but, in general, roughly symmetric. (b) states with $p \simeq 0$. The typical state here is asymmetric (c) states with $p \simeq +78$. This corresponds to a maximum of the 2-kick correction. States here are generally symmetrical, but broad and flat-topped.

p_0=0 ends up with non-zero average momentum $< p >$ after time t due to asymmetric momentum probability distribution. The figure unsurprisingly shows that states localised close to $p = 0$ are remarkably asymmetric. The states are considerably extended towards positive momentum, but are strongly localised towards negative p.

This behaviour neatly accounts for the form of the experimental momentum distribution shown in Fig. 3.10, which for $A = -\pi/2$ were also more extended towards positive p. The states localised near $p \simeq -\pi/4\epsilon$ and $\pi/4\epsilon$ correspond to, respectively, a minimum and a maximum of the classical diffusion. They are roughly symmetrical (typically) but vary by up to a factor of ~ 40 in L. In [43] it was proposed that the observed variation in the energy absorption rates between atoms prepared with an initial drift momentum $p_0 = -\pi/4\epsilon$ (which absorb very little energy) and those with $p_0 = \pi/4\epsilon$ might be exploited to filter traffic of atoms through an optical lattice (see chapter 3).

The form of the underlying Floquet states explains this differential rate of energy absorption. Subsequently, it was found experimentally that the 2δ-KR in fact shows much more pronounced differential absorption rates, without requiring the application of a rocking field A. In the next chapter, we report a study of the Floquet states of this system.

5.2.3 Local break time versus initial momentum for the perturbed-period KR

In [40, 43], it was demonstrated that the diffusion rate is momentum dependent and associated with a corresponding local break time $t^*(p) \simeq D(p)/\hbar^2$. Here, we present the local break time, which oscillates in the same way along

with the initial momentum, obtained by calculating mean energy level spacing of eigenvalues of the Floquet states. This is possible since the break time is related to the mean level spacing, Δ, through $T_H = \frac{2\pi\hbar}{\Delta}$ [42]. (After this time, the quantum system does not follow classical chaotic behaviour, i.e. the diffusive energy stops growing).

The overlap coefficient, $|C_n|^2$, can be obtained by $|C_n|^2 = | < \psi_n|\Phi > |^2$ for the *nth* eigenvector, where ψ_n is the *nth* Floquet state and Φ is the initial wave packet: for the system we consider, the overlap weight was obtained by overlapping the Gaussian wave packet in momentum space with the *n-th* Floquet state. In order to get the value of Δ, we needed the number of eigenstates N, which overlapped with the initial coherent state giving a value of $|C_n|^2 \geq 0.01$. The value of Δ was then obtained from $2\pi/N$, where N is the number of eigenstates obtained above (for one period). This is because the quasi energy, the eigenvalue of the Floquet operator, has modulus of 2π.

Fig. 5.4 shows the result of this calculation with parameter K=3.4, $\hbar$=1, ϵ=0.01 (T_1=1.01, T_2=0.99) in the perturbed kick system. The local break time (solid line) oscillates along with the average momentum of the overlapped initial wave packet with period of $\sim$ 314 (i.e. π/ϵ). Fig. 5.4 shows the break-time in (a) and the corresponding distribution of Floquet states in (b) for comparison. The overall figure is consistent with the numerical results from the evolving wave packet in momentum space, though the break-time at the multiples of π/ϵ (the regular dips) gives a greater value than the one expected. The expected value is $\sim$ 2 - 3 kicks.

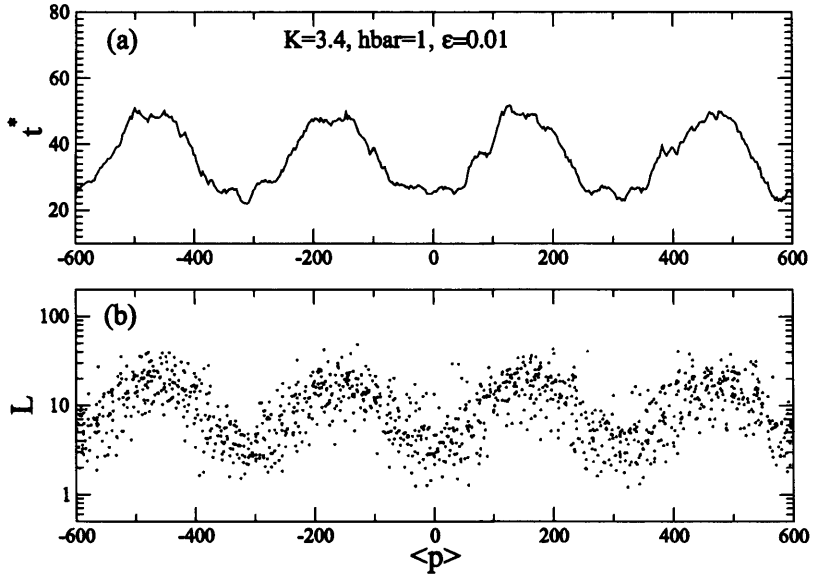

Figure 5.4: Break time for the perturbed-period KR, parameters are K=3.4, $\hbar$=1, ϵ=0.01, $A = 0.01\pi$: break-time in the top panel is obtained by using the formula $t^* = \frac{2\pi\hbar}{\Delta}$ and shown against average momentum $< p >$. The number of eigenstates with $|C_n|^2 \geq 0.01$ are chosen to calculate the mean energy level spacing, Δ, which overlap with the initial wave packet. The bottom panel shows the corresponding distribution of Floquet states.

5.3 Floquet properties of the 2δ-KR

5.3.1 Distribution of Floquet states

Following the description of the 2δ-KR in chapter 4, Floquet states are here shown in three different regimes.

First, the evolution operator for the 2δ-KR is given by

$$\begin{aligned} U_{lm} &= U_l^{free} U_{lm}^{2-kick} \\ &= e^{-\frac{il^2\hbar\tau}{2}} \Sigma_k J_{l-k}(\frac{K}{\hbar}) \times e^{-\frac{ik^2\hbar\epsilon}{2}} J_{k-m}(\frac{K}{\hbar}). \end{aligned} \tag{5.13}$$

As for the perturbed-period KR, the 2δ-KR system is analysed by obtaining Floquet states from diagonalising the time evolution operator for one period, $U(T_1 + T_2, 0)$, where $T_1 = \tau$ and $T_2 = \epsilon$ (the definitions of τ, ϵ are the same as in chapter 4). The 2δ-KR system is also time periodic, implying that we can apply the Floquet theorem described in chapter 4 to this system exactly in the same way. Thus, the numerical methods to obtain the Floquet states are omitted in this section.

Fig. 5.5(a) shows the localisation lengths of the Floquet states in momentum space for a weak kicking-strength, K=1. The other parameters used have values ϵ=0.025 and $\hbar$=0.5. The vertical axis is calculated by the root mean square deviation from $\sqrt{< p^2 >_n - < p >_n^2}$ and the horizontal axis indicates the average momentum, obtained by $\bar{p} =< \psi(0)|p|\psi(0) >$ at t=0. As in the perturbed-period KR case, a small but non-zero rocking term, $A = 0.01\pi$, is introduced into the potential kick in order to desymmetrize the eigenstates in momentum space and remove accidental degeneracies. It can clearly be seen that the localisation varies periodically as a function of momentum, staying within the range $1 \leq L \leq 10$ for the majority of points, with the exception of a series of sharp cusp-like features at which the locali-

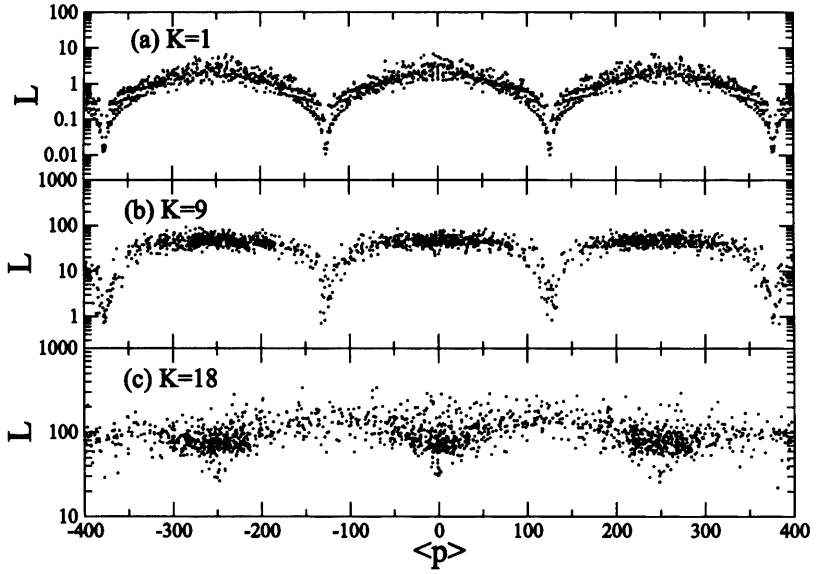

Figure 5.5: The figure shows the localisation lengths of typical states for the double δ-KR($\epsilon = 0.025$, $\hbar = 0.5$). Each figure corresponds to the three classical diffusion regimes investigated in the experiments in [57] (see figure 4.3). The vertical axis is on a logarithmic scale.

sation falls dramatically. The locations of these cusps exactly corresponds to the 'trapping momenta', $p\epsilon = (2n+1)\pi$, predicted from classical arguments in Eqn. 4.8. The Floquet states centred in the trapping regions have widths of $L \simeq 0.01$, much narrower than states localised on stable islands, which are also visible in this figure as regular strings of points at $L \sim 1$.

At the experimental values of $K \simeq 3$ and $\epsilon = 0.01$, a similar behaviour is produced, with the broadest Floquet states having localisation lengths of $L \simeq 60$, while the narrowest have widths of $L \simeq 0.03$, over one thousand times narrower. The effect of increasing the kick-strength is shown in Fig. 5.5(b). In this regime, there is an almost constant localisation length for momenta in between the trapping regions, which are again signalled by sharp cusp-like structures. This indicates that the Floquet states are confined between the classical broken phase barriers in the trapping regions.

Interestingly, the level statistics of the corresponding quasi-energies are not pure Poisson in this regime, as would be the case for the standard QKR. Full details follow in chapter 6. In Fig. 5.5 (c), we see an inversion of the broad momentum modulation in Fig. 5.5 (a), similar to the reversal seen in the experiment. In this regime, the eigenstates localised in the trapping regions near $p\epsilon \simeq (2n+1)\pi$, where n=0, 1, 2.., are typically *broader* than those localised in between.

5.3.2 Floquet states for the 2δ-KR

Some Floquet states shown in Fig. 5.6 are chosen from each corresponding panel in Fig. 5.5. Again, parameter values used are $\epsilon = 0.025$, $\hbar = 0.5$ and kick strength, K, changes from 1 to 18. The behaviour of individual Floquet states can be observed from the figure. In Fig. 5.6(a), the Floquet states

are localised exponentially in momentum space giving the characteristic triangular shape when plotted on a logarithmic scale.

As seen in Fig. 5.5, Fig. 5.6 (a) also shows a periodicity of $2\pi/\epsilon$. Note that two Floquet states at $p = \pm\pi/\epsilon$ are very narrow as undisturbed plane waves. Note also that the profiles of the other Floquet states, which are opposite to each other about $p = \pm\pi/\epsilon$, are symmetric but the individual states show overall asymmetric profiles. As clearly seen, the profiles of those eigenstates drop sharply near the very narrow eigenstates at $p = \pm\pi/\epsilon$. It is important to note that this asymmetry resembles the asymmetric dynamical localisation. This asymmetry becomes stronger towards the narrow states, and thus, leads to the strong current in the region (see Fig. 4.9).

On the other hand, those Floquet states near the regions where $p\epsilon=2n\pi$, are much wider in momentum space and are symmetric. Fig. 5.6(b) reflects the staircase effect with a width of one step of $2\pi/\epsilon$, as was shown in dynamical localisation for the 2δ-KR in Fig. 4.11. The black line shows the eigenstate chosen from near zero average momentum , $< p >= 0$ giving the rough symmetric profile (the figure does not show the exact symmetric profile as the value of $< p >$ is not exactly zero). The other two come from the trapping regions and have small spikes on the top. All of them show the same 'staircase' structure.

Fig. 5.6 (c) demonstrates the hugely extended eigenstates with a big value of kick strength K. Due to the enormous width of each Floquet state, it is difficult to show the reversal of energy spread by looking at the Floquet states from the figure. The staircase effect is still visible but the step-size is reduced to the order of $\sim 10^{-6}$.

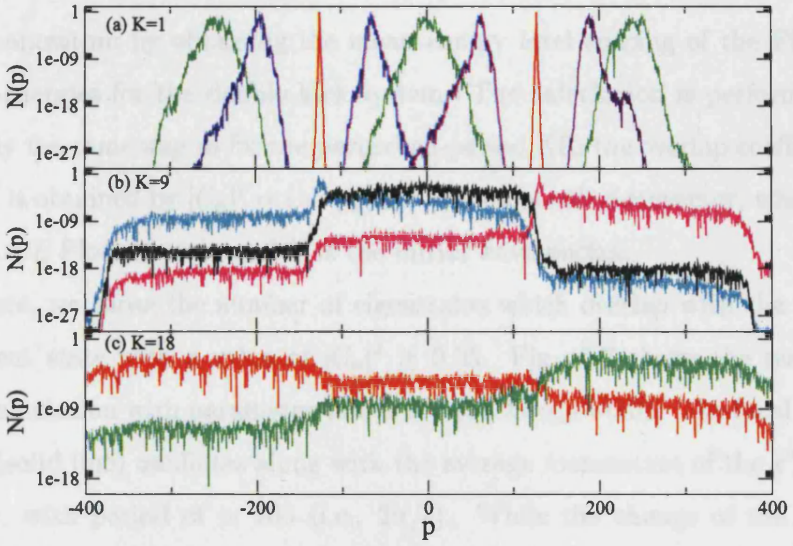

Figure 5.6: Floquet states for the 2δ-KR are exponentially localised in momentum space. $\epsilon = 0.025$, $\hbar = 0.5$. (a): two Floquet states at $p \simeq$ -125, 125 remain as undisturbed plane waves, while others in between are greatly broadened. As the kick strength increases, Floquet states in (b) and (c) dramatically expand in momentum space.

5.3.3 Local break time versus initial momentum for the 2δ-KR

Like the perturbed-period KR, the 2δ-KR also has a momentum dependent diffusion rate, associated with a corresponding local break time $t^*(p) \simeq D(p)/\hbar^2$. Therefore, we can also calculate the local break-time versus initial momentum by obtaining the mean energy level spacing of the Floquet quasi-energies for the double kick system. The calculation is performed in exactly the same way as for the perturbed-period KR: the overlap coefficient, $|C_n|^2$, is obtained by $|C_n|^2 = |<\psi_n|\Phi>|^2$ for the *nth* eigenvector, where ψ_n is the *nth* Floquet state and Φ is the initial wave packet.

Here, we chose the number of eigenstates which overlap with the initial coherent state with a value of $|C_n|^2 \geq 0.05$. Fig. 5.7 shows the result of this calculation with parameter values K=3.4, $\hbar$=1, ϵ=0.06. The local break time (solid line) oscillates along with the average momentum of the Floquet states, with period of $\simeq$ 105 (i.e., $2\pi/\epsilon$). While the change of the break time as the average momentum changes is shown in (a), the corresponding distribution of Floquet states is shown in (b) for comparison. It is clearly seen that the two figures are consistent.

5.4 Short-long vs long-short kick-sequence

As shown in Fig. 5.6, the Floquet states at the tips of the cusps in Fig. 5.5 have such low localisation lengths that they are effectively pure plane-wave states. It is thus unsurprising that the presence of these states corresponds to the classical trapping effect, as a quantum system prepared in such a state

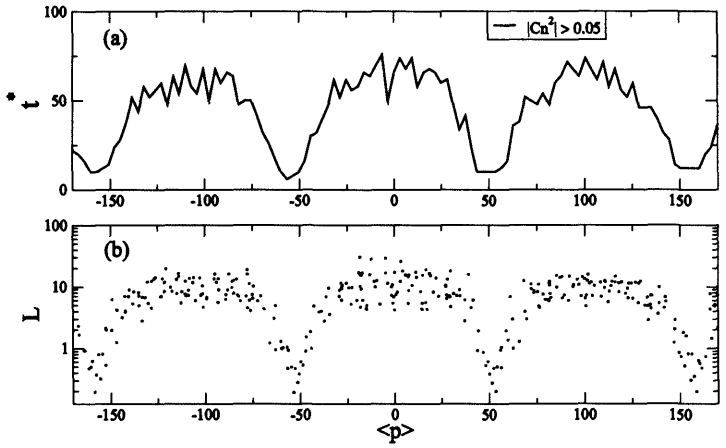

Figure 5.7: Local break time versus initial momentum for the double δ-KR is shown in (a). Parameter values are K=3.4, $\hbar$=1, $A = 0.01\pi$, ϵ=0.06. The number of eigenstates with $|C_n|^2 \geq 0.05$ was used to calculate the mean energy level spacing, Δ, of states that overlap with the initial wave packet. The bottom panel (b) shows the corresponding distribution of the Floquet states.

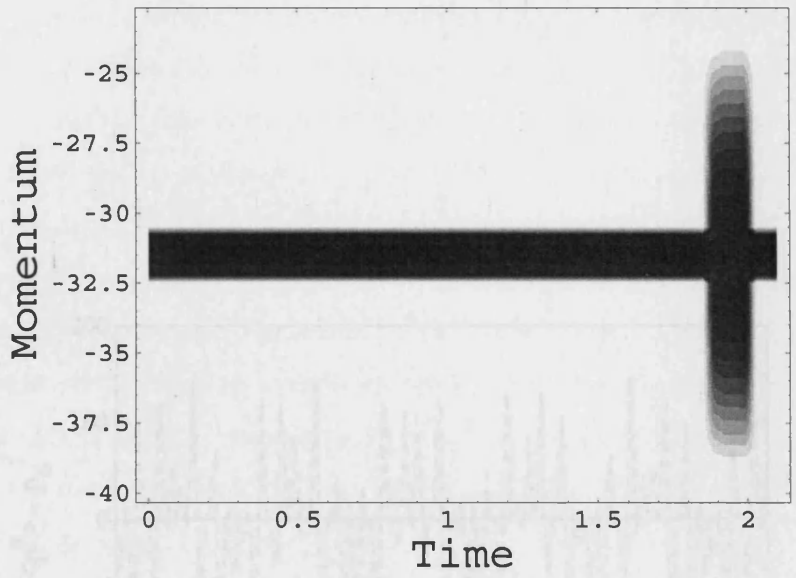

Figure 5.8: Time evolution of a localised Floquet state in momentum space, $N(p,t)$, for physical parameter values: $K = 2$, $\epsilon = 0.1$ and $\hbar = 0.5$. Initially, the Floquet state is sharply peaked at $p = -10\pi$, in the centre of a trapping region. The first kick at $t = 1.9$ causes the state to spread across a much broader range of momentum, until the second kick at $T = 2$ restores the localised state.

will have a vanishingly small overlap with any other state and so will remain frozen (or trapped) in its initial state. It is important to note, however, that this quantum trapping effect depends critically on the *order* of the two kick-periods – that is, whether the system is driven with a short-long kick-sequence or the inverse long-short ordering.

This may appear surprising at first, since the Floquet states are periodic, with the same period $T = \tau + \epsilon$ as the driving, and this period is not altered by interchanging the order of the kicks. Although it is frequently neglected, however, it is important to recall that the Floquet states do have an explicit

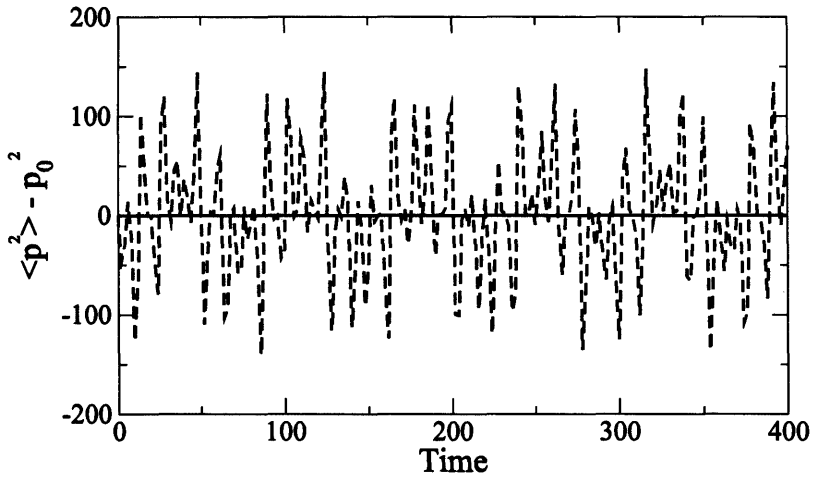

Figure 5.9: Time-evolution of the energy of the 2δ-KR for the same physical parameter values (K=1, $\hbar = 0.5$, $\epsilon = 0.025$) as in Fig. 5.5(a). The solid line shows the evolution of the system under the long-short kicking sequence and shows few features. The dotted line shows the result of the short-long sequence, and exhibits a complicated quasi-periodic behaviour.

time-dependence within each period, and this *is* able to produce substantially different behaviour [70] when the phase of the driving field is altered. Fig. 5.8 illustrates the time-evolution of one of the localised Floquet states, which experiences δ-kicks at times $t = \tau = 1.90$ and $t = T = 2$. As can be seen, the state has only a trivial time-evolution during the first time-interval ($0 \leq t < \tau$), since it is almost a plane wave and is thus approximately an eigenstate of the free Hamiltonian. The first kick at τ causes the wave-packet to spread considerably in momentum space before the second kick restores this broadened state to its original narrow form. Thus, in this brief window of time between the two kicks, even the most localised Floquet states have a considerable spread in momentum.

As a consequence, if the phase of the kicking field is shifted so that the system experiences the short-long kick-sequence, none of the Floquet states is sharply localised in momentum at $t = 0$. In Fig. 5.9, the time-evolution of the system's kinetic energy is shown when it is prepared in a momentum eigenstate in a trapping region. For the long-short kick-sequence, this state projects onto essentially a single Floquet state at $t = 0$, and so its time evolution is trivial and its energy remains constant. For the case of the short-long kick-sequence, however, the initial state projects onto a number of Floquet states (Eqn. 5.10), giving rise to a complicated quasi-periodic behaviour arising from beating between the different quasi-energies.

CHAPTER 6

Statistics of the double δ-kicked system

This chapter describes the eigenvalue statistics for the 2δ-kicked rotor system, which has been examined throughout this thesis. In this thesis, our statistical study of the double δ-kicked system stays within the investigation of the nearest neighbouring energy level spacing distribution and the number variance. The numerical study shows that the (Σ_2) statistics exhibits novel behaviour in terms of the current interest of critical statistics in a chaotic KAM system (introduced in chapter 2.1). Here we find that the number variance statistics have a form analogous to that of the Metal Insulator Transition (MIT) in a disordered system. We managed to obtain a large number of eigenvalues for accurate statistics, with little fluctuation in the presentation of the variance and the nearest neighbour spacing distribution. The contents of this chapter are:

• an introduction to the (band) random matrix theory, some statistical prop-

erties and critical statistics

- numerical methods used to obtain the energy levels and eigenvectors of our system; symmetrisation of wave function, computational methods
- finally, numerical results and summary.

6.1 Nearest neighbour spacing distribution

The $P(s)$ distribution of nearest-neighbour spacings (NNS) is considered to be a tool to observe a fingerprint of chaos in quantum dynamics. If the energy difference between two consecutive levels is $s_i = E_{i+1} - E_i$, $P(s)$ is a probability distribution to find the neighbouring energy level between s and $s + ds$ with conditions,

$$\int_0^\infty P(s)ds = 1, \tag{6.1}$$

$$\int_0^\infty sP(s)ds = 1. \tag{6.2}$$

In a quantum integrable system, neighbouring energy levels do not interact, i.e. they are not correlated with each other, hence they can be considered as independent random variables. Due to the absence of level repulsion, the distribution of spacings shows a Poisson distribution,

$$P(s) = \exp(-s) \tag{6.3}$$

6.1.1 Universality in random matrix theory

On the other hand, for a quantum system whose classical counter-part is chaotic, i.e. non-integrable, the spectral statistics can be predicted by random matrix theory. Random matrix theory was originally developed by Wigner, Dyson, Mehta, and others in nuclear physics in the 1950's and 60's

[71, 72, 73, 74]. Since the famous conjecture by Bohigas, Giannoni and Schmit in [79] and overwhelming evidence from different systems in the following years, RMT now can be applied to the spectra of all chaotic systems. The standard introduction to the theory can be found in [76] among others. According to the theory, depending on their symmetries, there are three different universal classes which asymptotically show the same statistical behaviour (in a measurement of probability). Each class shows a different degree of level repulsion; in terms of a general expression at short range (small s), $P(s) \sim s^{\beta}$, the values of β=1, 2, 4 correspond to linear, quadratic and quartic level repulsion (further details for the case with $\beta = 4$, which is the Gaussian Simplectic Ensemble case, is omitted). For a Hamiltonian with time reversal symmetry, the energy level distribution $P(s)$ agrees well with the Gaussian Orthogonal Ensemble(GOE) predicted by random matrix theory.

$$P(s) = \frac{\pi s}{2} \exp(-\frac{\pi s^2}{4}) \tag{6.4}$$

If time reversal symmetry is broken, the Hamiltonian cannot be written as a real symmetric matrix but rather as a complex Hermitian matrix, and hence one finds the quadratic level repulsion and the spacing distribution is close to the Gaussian Unitary Ensemble(GUE).

$$P(s) = \frac{32}{\pi^2} s^2 \exp(-\frac{4s^2}{\pi}) \tag{6.5}$$

Figure 6.1 shows the nearest neighbour level spacing distribution $P(s)$ corresponding to Poisson, GOE and GUE. Band Random Matrices are required for the localised quantum dynamics, which is described in the following section.

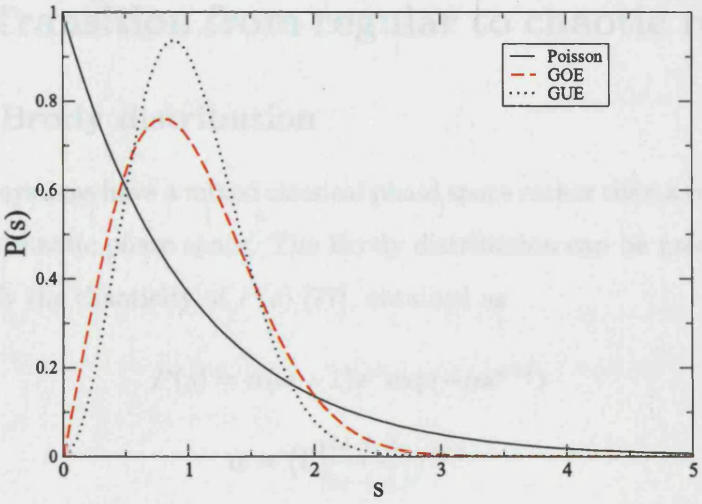

Figure 6.1: The nearest neighbour spacing distribution $P(s)$ of Poisson, GOE and GUE.

6.2 Number variance

Although the nearest neighbour spacing distribution is more popular due to its simplicity, it depends on all correlation functions among the energy levels. The number variance, denoted as $\Sigma_2(L)$ is the variance of the number of levels, contained in an energy interval of length L. The mathematical analysis can be found in [75]. For the statistical study of the 2δ-kicked system, the number variances were obtained numerically by $\Sigma_2(L) =< L^2 > -< L >^2$ and are presented in the section giving numerical results. For integrable systems where the eigenvalues are uncorrelated, $\Sigma_2(L) = L$. In contrast, for the Gaussian ensembles, the level repulsion tends to equalise the distance between neighbouring eigenvalues. Consequently, the number variance increases only logarithmically for large L, $\Sigma_2(L) = \ln(L)$.

6.3 Transition from regular to chaotic regime

6.3.1 Brody distribution

Most real systems have a mixed classical phase space rather than a completely regular or chaotic phase space. The Brody distribution can be used in order to quantify the chaoticity of $P(s)$ [77], obtained as

$$P(s) = \alpha(\omega + 1)s^{\omega} \exp(-\alpha s^{\omega+1}) \tag{6.6}$$

$$\alpha = \left(\Gamma[\frac{\omega + 2}{\omega + 1}]\right)^{\omega+1} \tag{6.7}$$

where ω is the Brody parameter measuring the strength of repulsion between neighbouring energy levels. For $\omega = 0$, the Brody distribution follows the Poisson distribution, and the GOE distribution for $\omega = 1$. The Brody parameter characterises a given system qualitatively without any deeper physical meaning. It is demonstrated in [86] that the Brody distribution shows the wrong value near the GOE distribution (where $\omega = 1$) and large spacings $s \gg 1$ though it gives a correct value near the Poisson distribution ($\omega = 0$). The Brody distribution also is not valid when the repulsion is larger than 1, for the case of GUE and GSE.

6.3.2 Berry-Robnik distribution

In [78], Berry and Robnik calculated the semi-classical level spacing distribution for systems with a mixed phase space, assuming that the spectrum is the superposition of uncorrelated levels from the regular and the chaotic regions: the levels from the regular region have a Poisson distribution and those from irregular region have a Wigner distribution. In the paper, the

Berry-Robnik distribution was obtained as

$$P(s,\rho) = \rho^2 \mathrm{e}^{\rho s}\mathrm{erfc}(\frac{\sqrt{\pi}}{2}\rho s) + (2\rho\bar{\rho} + \frac{\pi}{2}\bar{\rho}^3 s)\mathrm{e}^{-\rho s - \frac{\pi}{4}\bar{\rho}^2 s^2} \tag{6.8}$$

where $\bar{\rho} \equiv 1 - \rho$ and

$$\mathrm{erfc}(x) = \frac{2}{\sqrt{\pi}} \int_x^\infty e^{-t^2} dt \tag{6.9}$$

is the complement of the error function. In the two limiting cases, $\rho = 1$ and $\rho = 0$, the Berry-Robnik distribution reproduces the Poisson and the Wigner distribution (GOE) respectively.

6.4 Statistics for the δ-kicked rotor

6.4.1 Banded random matrix theory

The periodically kicked quantum rotor was found in [80, 82] to have statistics similar to those expected for random band-diagonal Hamiltonians. For example, for quantum motion in a (one-dimensional) random potential in a solid state: the wave functions are localised in space (Anderson localisation) in the way like the quantum kicked rotor localises in energy (dynamical localisation) (see chapter 2). The (classically chaotic) QKR does not display the expected level repulsion in its spectral statistics since the eigenstates of the Floquet operator are exponentially localised in momentum space. Their momentum distributions $N(p) \sim |p - \bar{p}|/L$, where L is the localisation length. Any pair of eigenstates i, j for which $|\bar{p}_i - \bar{p}_j| \gg L$ will not overlap significantly. Hence, the resulting energy level statistics displays a Poissonian distribution. Izrailev in [83] investigated the quasi-energy level spacing distribution $P(s)$ for the simple quantum kicked rotor system whose classical dynamics is chaotic. By using the finite size of the matrix, he showed that

the statistics made a transition from a Poisson distribution for a small kick strength to a Wigner distribution for a large kick strength as the matrix lost its banded character.

As is known, according to the RMT, when $b \ll N$, where b, N is the band half-width and the dimension of the matrix respectively, the matrix is almost diagonal, and shows the Poissonian statistics. However, as $b \to N$, the statistics change to GOE statistics [81, 82, 86]. For the quantum kicked rotor, the band structure appears in a matrix representation of the time evolution operator $U(T, 0)$. As described in chapter 2, the 'kick' term in the matrix elements involves a Bessel function, $J_{l-m}(K/\hbar)$, and this produces the banded character due to the sharply decaying Bessel value as $K/\hbar$ increases, i.e. $J \sim 0$ if $|l - m| \geq K/\hbar$ (illustrated in figure 6.4 later in this chapter).

In [85, 82, 86], the statistics of eigenvalues of Band Random Matrices were found to depend on a scaling parameter $x = b^2/N$. A similar scaling parameter is relevant in the spectral statistics of the kicked rotor on the torus for which the phase space is periodic (bounded) both in position x and momentum p.

In addition, the average localisation length of typical eigenstates divided by the dimension of the matrices, $< l_H > /N$, is a function of b^2/N. Hence, the eigenvalue spacing distribution $P(s)$ reflects the degree of 'filling' of the matrix by a typical eigenstate. In [85, 82], numerical data showed that in the extreme case $b^2/N \ll 1$ (strong localised states), there is little overlap between the eigenstates, so the eigenvalues are uncorrelated (Poissonian). For $b^2/N \gg 1$ (extended chaotic states), the eigenstates overlap strongly so the behaviour is GOE. This scaling parameter found in the eigenstates was confirmed in the kicked rotor model [82], proving the universality of the scaling properties. (For the quantum kicked rotor model, the band size equals

the value of $K/\hbar$, i.e. $b^2/N \sim (K/\hbar)^2/N$.)

Fig 6.2 demonstrates the transition from Poisson to GOE statistics in the standard quantum kicked rotor as the kick strength K increases, for fixed N=2,000. The top figure with small $K/\hbar$ shows Poissonian statistics. The matrix elements are almost diagonal since $J_{l-m}(K/\hbar) \sim 0$ if $|l-m| \geq K/\hbar$. However, the bottom figure with the big $K/\hbar$ is close to a GOE distribution. The matrix has a much wider band than that for the top figure, due to the slower decay of Bessel functions.

6.5 Numerical methods

6.5.1 Symmetrisation of wave function

If a quantum particle is evolved with a kick, $V = K\cos x$, then we have the 'kick' term, $\hat{U}_{kick} = e^{-iK\cos x/\hbar}$ in the time evolution operator. This is even with respect to reflection about $x = 0$.

If our quantum states have a definite symmetry, eigenstates are symmetric or anti-symmetric combinations of plane waves, $|\pm l> = \frac{1}{\sqrt{2\pi}} e^{\pm ilx}$,

$$\psi_l^{\pm} = \frac{1}{\sqrt{2}}[|l> \pm |-l>] \tag{6.10}$$

Quantum states couple only with states of the same symmetry, i.e. $<\psi_n^{\pm}|\hat{U}|\psi_l^{\mp}> = 0$. The system thus decouples into two independent blocks of quantum states. Inasmuch as the size of our eigenvector matrix $\propto N^2$, we need only 1/4 of the RAM, when we diagonalise a matrix of elements of either $<\psi_n^{+}|\hat{U}|\psi_l^{+}>$ or $<\psi_n^{-}|\hat{U}|\psi_l^{-}>$.

In our calculation, $V = K\sin x$ was used. Symmetrisation is shown below:

$$V = K\sin x \equiv K\cos(x + \pi/2) \tag{6.11}$$

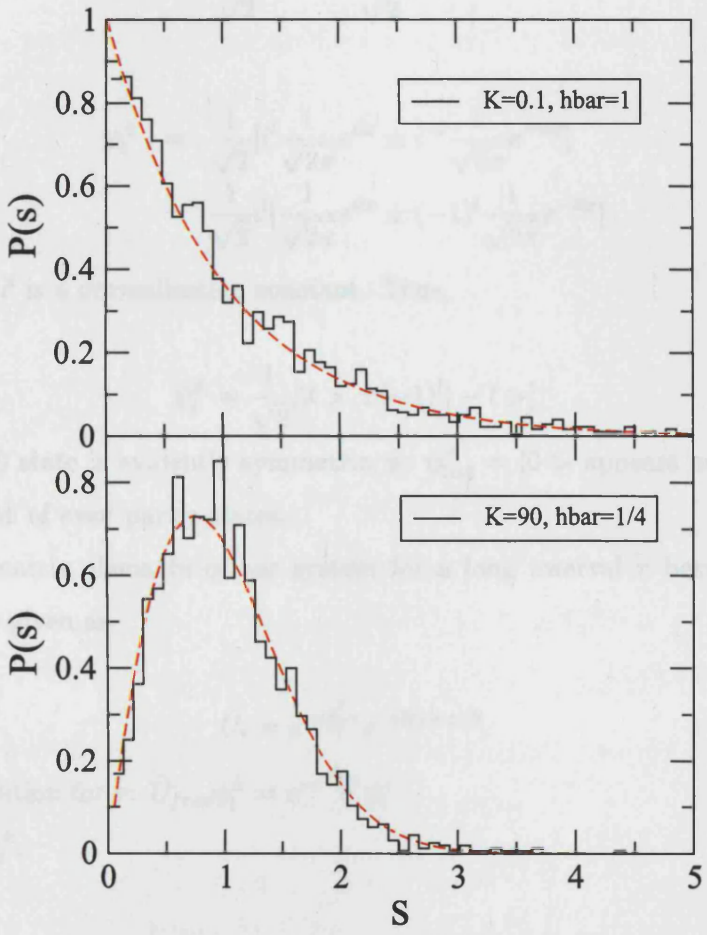

Figure 6.2: The nearest neighbour spacing distribution $P(s)$ for the different values of $K/\hbar$. The top figure shows a Poisson due to the small band size $K/\hbar$, while the bottom figure is close to a GOE distribution (the Brody parameter $\omega \simeq 0.8$) due to the much wider band size of the matrix.

If we set $x' = (x + \pi/2)$

$$\frac{1}{\sqrt{2}} e^{\pm ilx'} = \frac{1}{\sqrt{2}} i^{\pm l} e^{\pm ilx} \tag{6.12}$$

$$\begin{aligned} \psi_l^{\pm} &= \frac{1}{\sqrt{2}} [i^l \frac{1}{\sqrt{2\pi}} e^{ilx} \pm i^{-l} \frac{1}{\sqrt{2\pi}} e^{-ilx}] & (6.13) \\ &= \frac{1}{\sqrt{2}} i^l [\frac{1}{\sqrt{2\pi}} e^{ilx} \pm (-1)^l \frac{1}{\sqrt{2\pi}} e^{-ilx}] & (6.14) \end{aligned}$$

where $\frac{1}{\sqrt{2}} i^l$ is a normalisation constant. Thus,

$$\psi_l^{\pm} = \frac{1}{\sqrt{2}} [|l> \pm (-1)^l |-l>] \tag{6.15}$$

The $l = 0$ state is evidently symmetric, so $\psi_{l=0}^{+} = |0>$ appears only in the calculation of even parity states.

The matrix elements of our system for a long interval τ between kick pairs, are given as

$$\hat{U}_\tau = e^{-i\frac{p^2}{2\hbar}\tau} e^{-iK \sin x/\hbar}. \tag{6.16}$$

Free evolution for τ: $\hat{U}_{free} \psi_l^{\pm} = e^{-i\frac{l^2\hbar\tau}{2}} \psi_l^{\pm}$.

For $\psi_l^{\pm}$,

$$e^{-i\frac{l^2\hbar\tau}{2}} \psi_l^{\pm} = e^{-i\frac{l^2\hbar\tau}{2}} \frac{1}{\sqrt{2}} [|l> \pm (-1)^l |-l>] \tag{6.17}$$

Therefore,

$$< \psi_n^{\pm} | \hat{U}_\tau | \psi_l^{\pm} > = e^{-i\frac{l^2\hbar\tau}{2}} < \psi_n^{\pm} | \hat{U}_{kick} | \psi_l^{\pm} > \tag{6.18}$$

with, for example,

$$\psi_m^{\pm} = \frac{1}{\sqrt{2}} [m > \pm (-1)^m |-m>] \tag{6.19}$$

Then

$$
\begin{aligned}
&< \psi_n^{\pm}|\hat{U}_\tau|\psi_l^{\pm} > \\
&= \frac{1}{2}[\, < n|\hat{U}_\tau|l > \pm(-1)^l < n|\hat{U}_\tau| - l > \pm(-1)^n < -n|\hat{U}_\tau|l > +(-1)^{n+l} < -n|\hat{U}_\tau| - l > \,] \\
&= \frac{1}{2}[\, < n|\hat{U}_\tau|l > \pm(-1)^{n+l} < -n|\hat{U}_\tau| - l > \pm(-1)^l < n|\hat{U}_\tau| - l > +(-1)^n < -n|\hat{U}_\tau|l > \,].
\end{aligned}
\tag{6.20}
$$

Now, we can prove $< \psi_n^{\pm}\hat{U}_\tau\psi_l^{\mp} >= 0$ for all n, l.

$$
< n|\hat{U}_\tau|l >= e^{-i\frac{l^2\hbar\tau}{2}} J_{n-l}(K/\hbar) \tag{6.21}
$$

and $J_{n-l} = J_{-(n-l)}$ for $n-l$ even

$J_{n-l} = (-1)^{n-l}J_{-(n-l)}$ for $n-l$ odd. For example,

$$
\begin{aligned}
< \psi_n^{-}|\hat{U}_\tau|\psi_l^{+} > &= \frac{1}{2}e^{-i\frac{l^2\hbar\tau}{2}}[\, < n|\hat{U}_{kick}|l > +(-1)^l < n|\hat{U}_{kick}| - l > \\
&\quad -(-1)^n < -n|\hat{U}_{kick}|l > -(-1)^{n+l} < -n|\hat{U}_{kick}| - l > \,] \\
&= \frac{1}{2}e^{-i\frac{l^2\hbar\tau}{2}}\big[J_{n-l}(K/\hbar) + (-1)^l J_{n+l}(K/\hbar) \\
&\quad -(-1)^n J_{-(n+l)}(K/\hbar) - (-1)^{n+l} J_{-(n-l)}(K/\hbar)\big].
\end{aligned}
\tag{6.22}
$$

The first and the fourth term cancel, so do the second and the third term: for example, consider the second and the third term

$$
(-1)^l J_{n+l}(K/\hbar) - (-1)^n J_{-(n+l)}(K/\hbar) \tag{6.23}
$$

$$
= (-1)^l\big[(-1)^{(n-l)} J_{-(n+l)} - J_{(n+l)}\big] \tag{6.24}
$$

if n and l have different parity, then $n \pm l$ is odd, while $n \pm l$ is even if n and l have the same parity. The second and the third term cancel in either way. $< \psi_n^{+}|\hat{U}_\tau|\psi_l^{-} >= 0$ can be proved in the same way. Therefore, $< \psi_n^{\pm}|\hat{U}_\tau|\psi_l^{\mp} >= 0$ implying no coupling between states of different parities. This is all for a single kick. For a double kick,

$$
< \psi_n^{-}|\hat{U}_\tau|\psi_l^{+} > \cdot < \psi_{n'}^{-}|\hat{U}_\epsilon|\psi_{l'}^{+} >= 0 \tag{6.25}
$$

6.5.2 Computational methods

A study of the spectral fluctuation for a time-periodic system involves a study of the eigenstates and eigenvalues of the one-period time evolution operator $U(T,0)$. For our statistical study, the eigenvalues were obtained by diagonalising the matrix in a plane wave basis $|l>$ with lmax $\equiv$ lmax (the order of matrix, which is termed here as 'lmax' $= 0 \rightarrow$ 10,000) on the mid-range computer, Ra, at UCL HiperSpace centre.

Ra is a cluster of four Sun Micro-systems V880 servers connected to a Blade 2000. A Ra user actually logs in to the Blade 2000. The maximum RAM for a single job is limited to 32GB. However, in practise, we found that the effective order of the matrix is 10,000, requiring memory $\sim$ 6.5GB RAM, in order to run several jobs securely and simultaneously on Ra. Ra uses a Sun Grid Engine as a resource and queueing system. When each job is submitted via the queueing system, the Grid engine distributes the job across the cluster and executes it. A job is submitted through a script file.

We used the zhbevd routine from the Lapack library on Ra. This routine calculates eigenvalues and eigenvectors for a complex banded Hermitian matrix. Inputs of the routine are the order of the matrix (N=lmax or N=lmax+1 for even or odd parity respectively) and the band width ($b \simeq$ 'nbes' in our code). As shown in Table 6.1, the memory size is significantly changed by the order of the matrix.

For statistics for the 2δ-KR, we calculated a total of eigenvalues between 40,000 and 60,000. These were obtained, however, by diagonalising matrices of dimension $N = 10,000$ only; for example, we can diagonalise first a matrix for 20,000 $\leq l \leq$ 30,000. Then we shift the basis to diagonalise a matrix with 30,000 $\leq l \leq$ 40,000, and so forth. we retain only the subset of well

Dimension N of matrix	Memory (K Bytes)
1000	69,897
2000	267,757
4000	1,047,477
5000	1,629,337

Table 6.1: Matrix size vs memory size. Memory increases as $\sim N^2$.

Band width	Memory (K Bytes)
200	6,626,656
300	6,738,669
350	6,794,675
450	6,906,688

Table 6.2: Band width vs memory size. Memory increases linearly $\sim$ nbes $\times$ 10(MB).

converged eigenvalues. For statistics in the critical regime approximately half of the eigenvalues obtained from each cycle (lmax=10,000) were used. More detailed descriptions for choosing 'good' eigenvalues follow in a later section. As will be seen in the numerical results, this large number of eigenvalues effectively minimised the spectral fluctuations in the plot of $P(s)$. Our time evolution matrix is not Hermitian but unitary. We converted it to a complex Hermitian matrix U_H by constructing $H^+ = \frac{1}{2}(U + U^\dagger)$ (see chapter 5), then the complex banded Hermitian matrix H^+ is fed into the zhbevd routine.

Table 6.1 shows the changes of the memory size for different dimension N of the matrix with the same band width (nbes=50).

Table 6.2 is obtained by changing the band width with the same matrix

basis, lmax=10,000. As our system includes two kicks in one period T, the evolution matrix is given by $U_T = U\epsilon \cdot U\tau$. The band width (nbes) can be estimated by $\sim 2{\times}2K/\hbar$ (the band width of each matrix is given as $\sim 2K/\hbar$).

It can be approximated that the total memory required increases as N^2 from Table 6.1. In contrast, Table 6.2 shows that the total memory increases with nbes linearly, i.e. $\sim$ nbes$\times$10(MB). The calculation time varies from $\sim$ mins for lmax $\sim$ 1000 to $\sim$ 10 hours for lmax $\geq$ 10,000. Keeping lmax=10,000 constant, the calculation times change more slowly with the band width (determined by the value $K/\hbar$).

6.5.3 Effect of size of angular momentum basis

Finite matrices are just an approximation for real infinite-dimensional Hamiltonians and only those statistical properties that do not depend on finite truncation are physically relevant. In numerical calculation, the matrices are obviously of finite order N; therefore, the matrices of large order are required in order to obtain eigenvalues whose corresponding eigenstates are not affected by the truncation of the matrix. For large K, the eigenvalues are selected by the condition that the average momentum $< p >$ is within the localisation length, approximated by $L \sim K^2/\hbar$, from both edges.

Fig. 6.3 shows four eigenvectors with different values of the average momentum $< p >$ in angular momentum space l. The angular basis used runs from 1 to 4000, with parameter values: $\hbar = 1/8$, $K = 7$ and $\epsilon = 0.04$, hence the average momentum ranges from 1 to 500. Fig. 6.3(c) and (d) illustrate two eigenstates near the edges of the angular momentum basis. Both eigenstates are so close to the edges that the probability distributions $|\psi(l)|^2$ are not well described by the basis; in (d) most of the probability lies within an

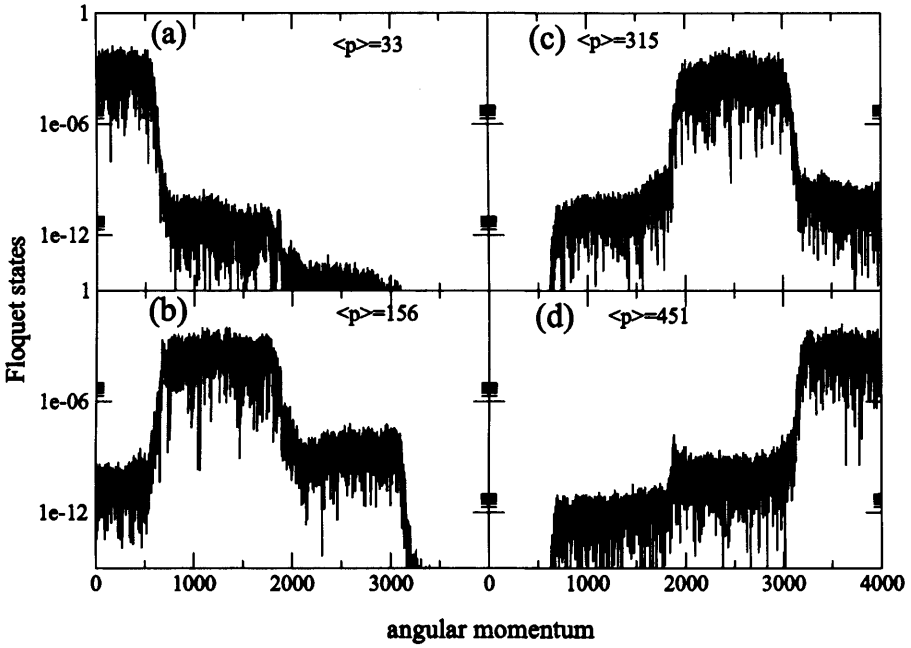

Figure 6.3: The figure shows four eigenstates for K=7, $\hbar$=1/8, ϵ=0.04 in angular momentum space. Each eigenstates has a different average momentum in a different cell. They show a characteristic 'staircase' structure.

incomplete cell. On the other hand, the other two, (a) and (b), show that the probability distribution of the eigenstates are far from the edges. In our calculations, the eigenvalues whose corresponding eigenstates are affected by the finite size of N as seen in (c) and (d) are discarded.

6.6 Statistics for the 2δ-kicked rotor system

6.6.1 Critical statistics

Current interest in critical statistics has arisen in the intermediate region between RMT and Poisson. Critical statistics in that region was extensively investigated in relation to the Metal Insulator Transition(MIT) in a (3-dimensional) disordered system. Critical statistics can be characterised by (i) semi-Poissonian statistics, $P(s) = 4se^{-2s}$ in the nearest neighbouring spacing distribution and (ii) the spectral multifractality. Critical statistics near the MIT in disordered systems has been proved to be universal: at the transition from GOE to Poisson due to Anderson localisation with increasing disorder, the crossover statistics shows that $P(s)$ has small s behaviour resembling the Wigner distribution (GOE) and large s behaviour resembling the Poisson distribution. Bogomolny *et al* [92], based on numerical results, demonstrated that this semi-Poisson statistics is also a good model for pseudo-integrable billiards. Not only have semi-Poisson statistics appeared mainly in studies of disordered (metallic) systems [87, 88], but also in other systems, such as a non-hydrogenic atom in a weak magnetic field [89] and the critical one-dimensional Haper model [94].

On the other hand, for critical statistics an interesting connection has been established between the multi-fractal characteristics of the wave functions and those of the spectral fluctuations [90, 91, 96]: the number variances of the spectra are linear $\Sigma_2(L) \simeq \chi L$ for $L \gg 1$, where χ is the level compressibility,

$$\chi = \Sigma_2(L)/L \simeq \frac{1}{2}(1 - \frac{D_2}{D}). \tag{6.26}$$

The value of χ varies depending on the fractal dimension, D_2, obtained from

the second moment of the wave function of the system considered, and D, the spatial dimension of the system. It is known that for integrable dynamics (Poisson statistics), $\Sigma_2(L) = L$, hence $\chi = 1$, while for chaotic dynamics (GOE), $\Sigma_2(L) \sim \ln L$. It is necessary to note that not all critical statistics has the semi-Poisson distribution, e.g. Varga *et al* [95] found critical statistics in a power-law random matrix ensemble whose spacing distribution deviates significantly from the semi-Poisson distribution.

Furthermore, critical statistics have been seen to be a generic feature of many different types of non-KAM systems: the classical phase space undergoes an abrupt transition from integrable to complete chaotic dynamics as a parameter changes [93]. However, to our knowledge, there has been no example of critical statistics in KAM systems. For these, the transition to chaos occurs gradually as a perturbing parameter increases. KAM systems are ubiquitous in many areas of physics. In the statistical study of the 2δ-kicked rotor, we probed a new spectral behaviour in the energy spacing distribution and compared to the properties shown in critical statistics.

6.6.2 The 2δ-kicked rotor

As shown in the previous chapters, the classical phase space of the 2δ kicked rotor is uniform in the fully chaotic regions divided by the trapping regions. This uniform structure allowed an analytical study of the anomalous classical diffusion without any detailed study of the classical phase space. Statistics in a KAM system is concerned with the phase space structure: the mixed phase statistics [98] is considered in systems for which classical phase space is mixed with stable islands and chaotic regions, while the intermediate statistics holds for most systems whose classical phase space is chaotic (BRMT belongs to

this category). It should be noted that in the 'critical' regime described here, the corresponding classical phase space is almost fully chaotic. Hence, the influence of the stable islands on localisation or delocalisation is negligible.

In a recent paper [99], we reported a new spectral behaviour found in the 2δ-KR. This can be compared with the MIT. The energy level spacing distribution $P(s)$ of our system shows a very interesting feature: it has intermediate statistics between Poisson and GOE, which shows a gradual transition to GOE over the critical regime but returns to Poisson instead of proceeding to GOE. It also shows some other features, different from semi-Poisson, for example, it follows the GOE transition. In the later section, three fits are illustrated in comparison with our NNS results.

To begin with the time evolution matrix for our system, Fig. 6.4 shows the matrix structure of the 2δ-KR in comparison with that of the standard QKR. The Hamiltonians for the standard QKR and the 2δ-KR are described in the previous chapter. Recalling that the time evolution operator is split into two terms,

$$\begin{aligned} U_{lm} &= U_l^{free} \cdot U_{lm}^{kick} \\ &= e^{-il^2T\hbar/2} \cdot J_{l-m}(K/\hbar), \end{aligned} \tag{6.27}$$

the kick terms, $J_{l-m}(K/\hbar)$, since $J_b(K/\hbar) \sim 0$ for $b \gg K/\hbar$, give the narrow banded matrix in the top figure 6.4 (as explained in the BRMT section). For the 2δ-KR, the corresponding matrix elements are given by

$$\begin{aligned} U_{lm} &= U_l^{free} \cdot U_{lm}^{2-kick} \\ &= e^{-il^2\tau\hbar/2} \cdot \Sigma_k J_{l-k}(K/\hbar) J_{k-m}(K/\hbar) e^{-ik^2\epsilon\hbar/2}, \end{aligned} \tag{6.28}$$

where $\tau = T - \epsilon$, τ the long time interval between kick pairs and ϵ the short time interval within a pair as defined in chapter 4. The free evolution

term effectively randomises the relative phases of the plane waves as in the standard QKR. As discussed in chapter 4, the U_{lm} for the 2δ-KR is insensitive to the value $\tau\hbar$. The term in the summation represents the total effect of the kick-pair and the small time interval ϵ. As ϵ is small, the *kth* waves can combine coherently. From the fact that U_{lm}^{2-kick} is invariant if $K\epsilon$ (hereafter K_ϵ) and $\hbar\epsilon$ ($\hbar_\epsilon$) are kept constant, together with the insensitivity of $\tau\hbar$, we can study the system by controlling only two scaled parameters, K_ϵ and $\hbar_\epsilon$ rather than varying K, ϵ and $\hbar$ independently.

As studied in [57], the consecutive kicks cancel for momenta $p \simeq (2n + 1)\pi/\epsilon$ generating momentum trapping regions permeated by cantori. Cantori are the fractal remnants of broken tori. The classical trajectories stick in the trapping regions, forming the fractal classical barriers. The diffusion correlations which control transport through these regions indeed depend only on K_ϵ. Classical phase space is periodic in p and is partly partitioned into equal 'cells' of width $\Delta p = 2\pi/\epsilon$. The corresponding matrix structure is illustrated in the bottom figure 6.4: the band oscillates in width and U is equally partitioned into sub matrices of dimension $N = \frac{2\pi}{\epsilon\hbar}$, corresponding to the momentum cells. At the centre of the cells, classical diffusion rates are of the same order as in the standard KR, so localisation lengths $L_p \sim K^2/\hbar$, for eigenstates well away from the trapping regions.

The couplings between cells which are separated from b/N change with the degree of filling of each cell. We first define a localised limit, where $b \ll N$ and $L_p \ll N\hbar = \frac{2\pi}{\epsilon}$. In this limit, most states feel no confinement and the energy level statistics shows a Poisson distribution. If we increase $K^2/\hbar$, but have negligible coupling between cells, we approach the limit $b/N \to 1$. Then, for all eigenstates, $L_p \to N\hbar$ as the probability for all states gradually fills the cell uniformly. If we increase $K^2/\hbar$ further, we reach another limit,

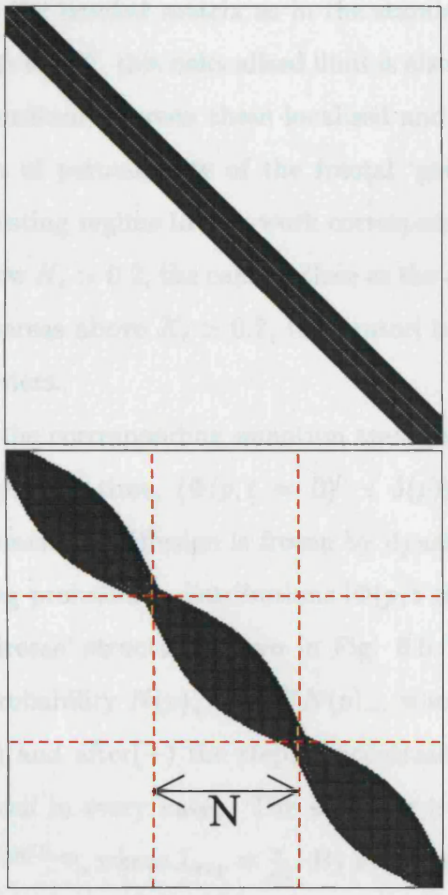

Figure 6.4: The top figure shows the structure of the time evolution matrix $U(T,0)$, for the quantum kicked rotor, in a basis of angular momentum states, exemplifying the structure of a Band Random Matrix (BRM), while the time evolution matrix for the 2δ-KR (bottom) shows the trapping regions (dashed lines) shrinking the band periodically.

i.e. an increasing proportion of eigenstates become delocalised over several cells. As the oscillatory structure of the band is lost, the separated cells become merged into the banded matrix as in the standard QKR in the top figure 6.4. For $N_{tot} \gg b \geq N$, this delocalised limit is also Poissonian. We are interested in the transition between these localised and delocalised Poisson limits, as a function of permeability of the fractal 'gates' (between cells). The classically interesting regime in this work corresponds approximately to $0.2 \leq K_\epsilon \leq 0.7$. Below $K_\epsilon \simeq 0.2$, the cantori close as the classical phase space becomes regular, whereas above $K_\epsilon \simeq 0.7$, the cantori become too 'open' to provide effective barriers.

We investigated the corresponding quantum transport by evolving a set of wave packets $\Phi(p,t)$ in time, $(\Phi(p,t=0) \simeq \delta(p))$ for a range of K_ϵ and $\hbar_\epsilon$, until the momentum diffusion is frozen by dynamical localisation at $t \simeq t_H$. The resulting probability distributions $|\Phi(p,t \gg t_H)|^2 = N(p)$ have a characteristic 'staircase' structure shown in Fig. 6.5. At each step, there is a steep drop in probability $N(p)_+ = e^{-2d}N(p)_-$, where $N(p)_\pm$ represents probability before(-) and after(+) the step, concentrated over the trapping region ($\sim 1/6$ of a cell in every case). The staircase tracks an exponential envelope $N(p) \sim e^{-2|p|/L_{exp}}$, where $L_{exp} = \frac{\pi}{\epsilon d}$. By averaging over several steps, d is obtained as a function of K_ϵ and $\hbar_\epsilon$. Fig. 6.6 shows d is proportional to $\hbar_\epsilon^{0.75}/f(K_\epsilon)$, where $f(K_\epsilon)$ is some function of the scaled kick-strength K_ϵ. The rough estimation is $d \simeq \frac{\hbar_\epsilon^{0.75}}{3.5K_\epsilon^3}$ and is used to place the localisation border. The critical regime with $K_\epsilon > 0.2$ in Fig. 6.6 can be seen between the localisation border ($K_\epsilon^2/\hbar_\epsilon \simeq 2\pi$) shown by the dashed line and the delocalisation border ($d \simeq 2$) shown by the dot-dashed line. The statistical results obtained between these regions are shown in the following section.

A study of $C(t) = \frac{1}{t}\int_0^t | < \Phi(p,t=0)|\Phi(p,t') > |^2 dt'$, the return proba-

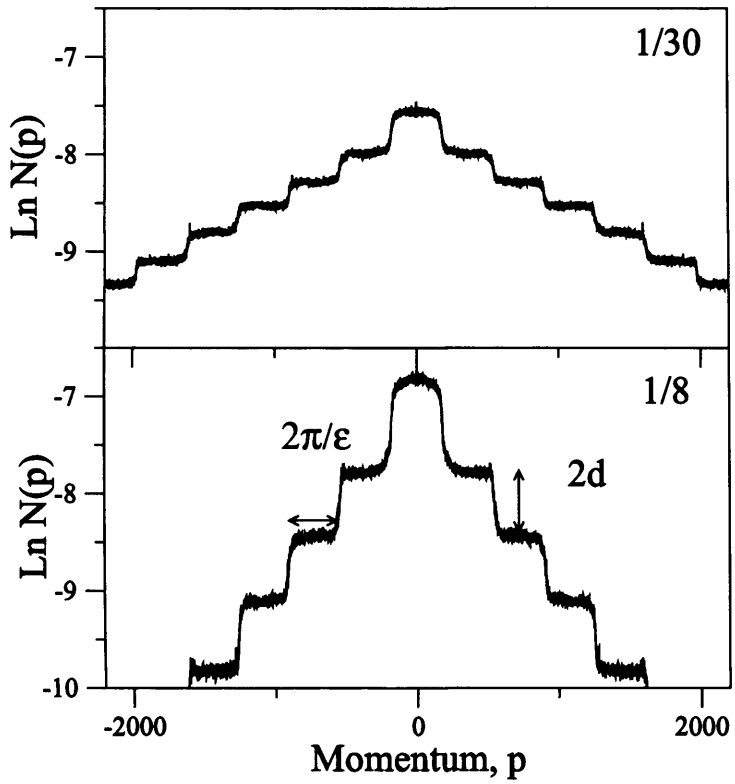

Figure 6.5: Figure shows the momentum distribution for quantum wave packets of the 2δ-KR for K=20, ϵ=0.0175 and $\hbar$=1/8 and 1/30 respectively on a logarithmic scale. $N(P)$ for both eigenstates and wave packets shows a long range tail of staircase form which on average follows the exponential $N(p) \sim e^{-2|p-\bar{p}|/L_{exp}}$, where $L_{exp} = N\hbar/2d$. Since $N\hbar = 2\pi/\epsilon$, the $\hbar$-dependence of L_{exp} is determined by the drop in probability d at each successive set of cantori. The first 1-3 steps can be seen in experiments with optical lattices [57].

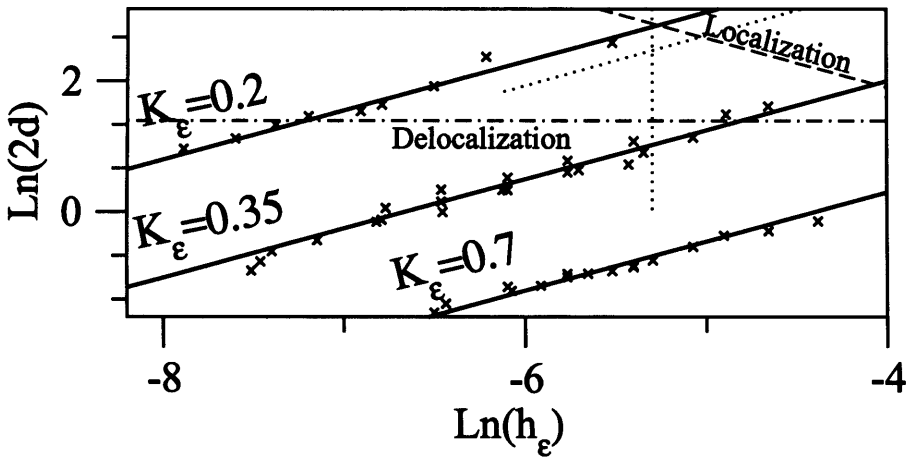

Figure 6.6: Figure shows that $\ln(2d)$ plotted versus $\ln(\hbar_\epsilon)$ lies on straight lines of invariant K_ϵ with constant slope 0.75. Thus, $d \propto \hbar_\epsilon^{0.75}$ and $L_{exp} \propto \hbar^{-0.75}$, different from the well known QKR with $L_{exp} \propto \hbar^{-1}$. The localisation border ($K_\epsilon^2/\hbar_\epsilon \simeq 2\pi$ is shown by the dashed line and the delocalisation border ($d \simeq 2$) is the dot-dashed line. The intermediate statistics can be probed between these borders. The vertical dotted line corresponds to the value $\hbar_\epsilon$=0.005 ($\hbar = 1/8$, ϵ=0.04). The diagonal dotted line corresponds to the value K_ϵ=0.225 (K=9, ϵ=0.025). The statistical results corresponding to those lines are investigated.

bility, shows that if $\Phi(p, t=0) = \delta(p)$, then $C(t) \sim t^{-1}$ for the first few kicks, but subsequently $C(t) \sim t^{-0.75}$ for a much longer time up to $t \sim t_H$. For wave packets started near the trapping regions, i.e. $\Phi(p, t=0) \simeq \delta(p - \pi/\epsilon)$, then $C(t) \sim t^{-0.75}$ from $t = 0$. Either way, the power-law decay law $C(t) \sim t^{-\nu}$ where $\nu = 0.75$ characterises all starting conditions. A relation has been established in [91, 97] between the power law decay exponent and D_2, the exponent which characterises the scaling of $|\psi|^4$ for individual eigenstates, i.e. $\nu = D_2$. Critical statistics in the MIT have shown the relation, $\Sigma_2(L) \simeq \frac{1}{2}(1 - D_2/D)L$ ($D = 1$ in our system).

6.6.3 Statistical results for Σ_2

Now, we illustrate the statistical results obtained for the 2δ-KR. In order to obtain the eigenvalues and eigenvectors for statistical analysis, the evolution operator $U(T, 0)$ was diagonalised in a plane wave basis split into even and odd parity. We found that eigenvalues from both parities are identical at large momentum p, i.e. $< p > \gg 0$ (roughly $\gg K^2/\hbar$), and most results illustrated here are obtained from lmax between 20,000 and 80,000. Thus, the statistics is the same irrespective parity chosen. Due to the large matrix diagonalised, we obtained many cells over different momentum ranges. For small value of $K/\hbar$, the localisation lengths are small, $L_p = \sqrt{< p^2 > - < p >^2} \ll \pi/\epsilon$, well within a single cell. The statistics are Poissonian. However, in the critical regime, typical eigenstates have localisation lengths, $L_p = \sqrt{< p^2 > - < p >^2} \simeq \pi/\epsilon \gg 1$ as most of the probability fills a single cell uniformly. Even though there can be a few eigenstates in cantoral regions with $L_p \ll \pi/\epsilon$, these disappear as the delocalisation border ($d \simeq 2$) is reached. Also those eigenstates make no appreciable effect on the

statistics.

Those eigenvalues obtained from diagonalisation were rearranged according to their average momentum $< p >$ and put in the corresponding cells: the *ith* eigenstate is in the *nth* cell if $(2n+1)\pi/\epsilon \leq < p_i > \leq (2n+3)\pi/\epsilon$. At the onset of delocalisation, states become spread over several cells (see Figure 6.3) and the statistics slowly return to Poissonian from this point. The number of eigenstates in a single cell is given by $\frac{2\pi}{\hbar\epsilon}$. The eigenvalues over several cells obtained for ϵ=0.04 and $\hbar$=1/8 are shown in Table 6.3. The statistics obtained from the eigenvalues, i.e. keeping $\hbar_\epsilon$ constant, show the transition from Poissonian to intermediate statistics and reverting to Poissonian.

We also obtained a number of eigenvalues with constant K=9 and ϵ=0.025 but varying $\hbar$ from 1 to 1/12. As seen in Table 6.4, the number of cells (hence the number of eigenstates) for $\hbar$=1/12 are greatly reduced inasmuch as we had to discard the cells affected by truncation of the matrix. The statistics with $\hbar$ less than this value show large spectral fluctuation in NNS distribution and loses reliability.

Using the data shown in Table 6.3 and 6.4, we first obtained Σ_2 and $P(s)$ for each cell then averaged over the cells. From this procedure, we obtained the statistics with little fluctuation.

The Σ_2 statistics for the data shown in the two tables are presented in Fig. 6.7. The frames present the variances in the spectral number density, $\Sigma_2(L) = < L^2 > - < L >^2$, where we consider a stretch of the spectrum with average $< L >$ levels. We found a linear form $\Sigma_2(L) \simeq \chi L$ in the critical regime for $1 \ll L \ll \frac{2\pi}{\hbar\epsilon}$ (see the top frame in Fig. 6.7). A straight line was fitted to the range $L = 5 \rightarrow 40$ to obtain the slope χ for all points except for the very large values of $\hbar$ from 1 to 1/4, where a fit to the smaller range $L = 5 \rightarrow \frac{2\pi}{30\hbar\epsilon}$ was used. The insets plot the values of χ calculated along the

Kick strength K	Number of cells	Number of eigenstates used
1	8	10,053
2	8	10,053
3	24	30,159
4	24	30,159
5	20	25,132
6	20	25,132
7	20	25,132
8	16	20,106
9	16	20,106
10	12	15,079
11	10	12,561
12	8	10,053
14	8	10,053

Table 6.3: The number of cells and eigenstates obtained. K varies from 1 - 14 with constant $\hbar = 1/8$ and $\epsilon = 0.04$.

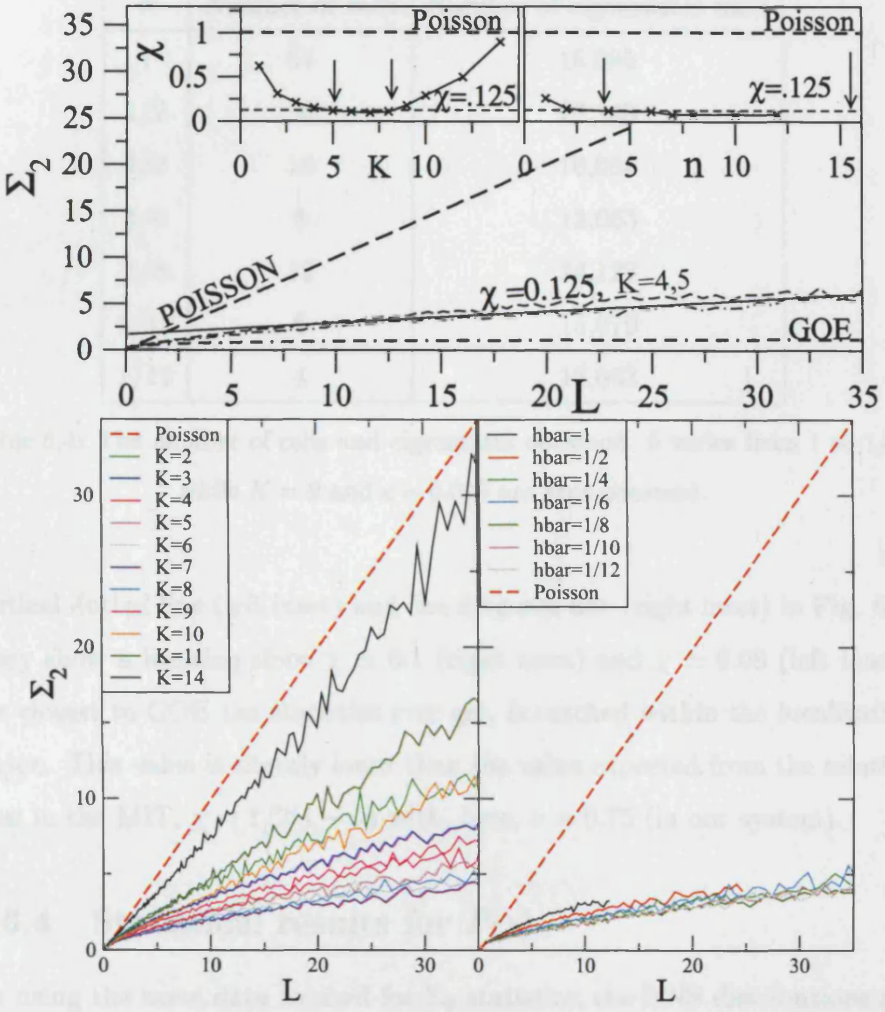

Figure 6.7: The top frame shows the $\Sigma_2(L)$ statistics and the line $\Sigma_2(L) = 0.125L$. The insets plot χ along the dotted line cuts in Fig. 6.6 (the left inset for the vertical dotted line and the right inset for the diagonal line). The arrows indicate the localisation and delocalisation borders respectively. The two bottom frames show Σ_2 for each set of parameter values: K from 2 to 14, $\hbar = 1/8$ and $\epsilon = 0.04$ (left); $\hbar$ from 1 to 1/12, $K = 9$ and $\epsilon = 0.025$ (right).

$\hbar$	Number of cells	Number of eigenstates used
1	64	16,085
1/2	56	28,148
1/4	16	16,084
1/6	8	12,063
1/8	12	24,127
1/10	6	15,079
1/12	4	12,063

Table 6.4: The number of cells and eigenstates obtained. $\hbar$ varies from 1 to 1/12 while $K = 9$ and $\epsilon = 0.025$ are kept constant.

vertical dotted line (left inset) and the diagonal line (right inset) in Fig. 6.6. They show a limiting slope $\chi \simeq 0.1$ (right inset) and $\chi \simeq 0.08$ (left inset), the closest to GOE the statistics ever get, is reached within the localisation region. This value is slightly lower than the value expected from the relation seen in the MIT, $\chi = 1/2(1-\nu)$ with, here, $\nu = 0.75$ (in our system).

6.6.4 Statistical results for $P(s)$

By using the same data as used for Σ_2 statistics, the NNS distributions are shown in this section. Histograms were obtained with the same number of bins (200) throughout the figures. As mentioned earlier, the NNS obtained with constant $\hbar_\epsilon$ ($\hbar = 1/8$, $\epsilon = 0.04$) varying K from 1 to 14 show Poissonian distributions in the limit where $K \leq 1$ or $K > 14$, and intermediate statistics in between. Another set of histograms obtained for constant $K = 9$, $\epsilon = 0.025$ varying $\hbar$ from 1 to 1/12 only shows intermediate statistics in the critical regime; it was difficult to obtain Poissonian statistics using this value K_ϵ

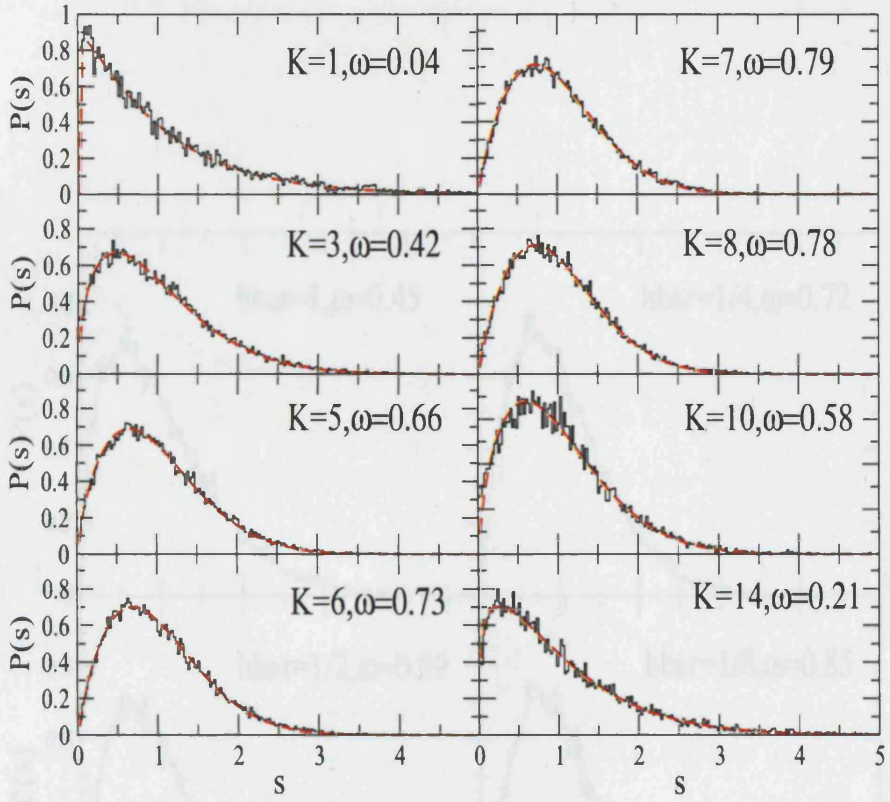

Figure 6.8: The fit to Brody distribution for the various K and constant $\hbar_\epsilon$ gives good agreements with our NNS distributions over all.

inasmuch as it is hard to reach either the localisation or delocalisation border on both ends in Fig. 6.6. The whole range of $\hbar$ from 1 to 1/12 belongs to the critical regime and the numerical results show a good agreement.

Now, we consider the three distributions used to fit our NNS results: Brody, Berry Robnik and the crossover distribution found by Ugajin [100]. As seen in Fig. 6.8 and 6.9, the Brody distribution shows excellent agreements with our NNS plots. In contrast, the Berry-Robnik distribution gives rather poor results at small s, especially, for the case where the NNS distributions

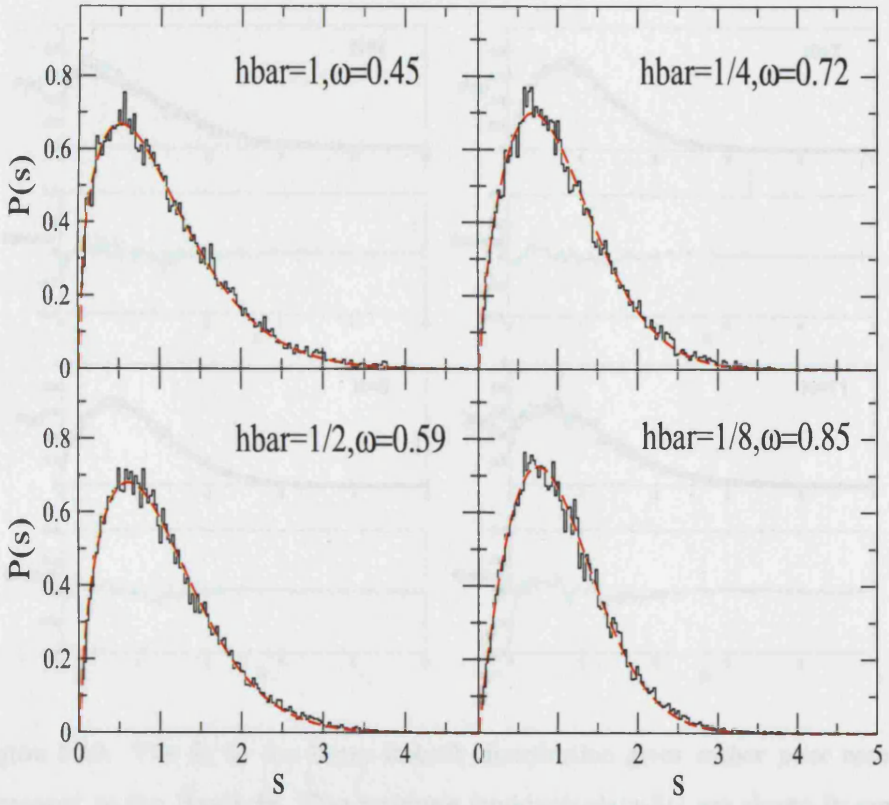

Figure 6.9: The fit to Brody distribution for the various $\hbar$ and constant K_ϵ gives good agreements with our NNS distributions.

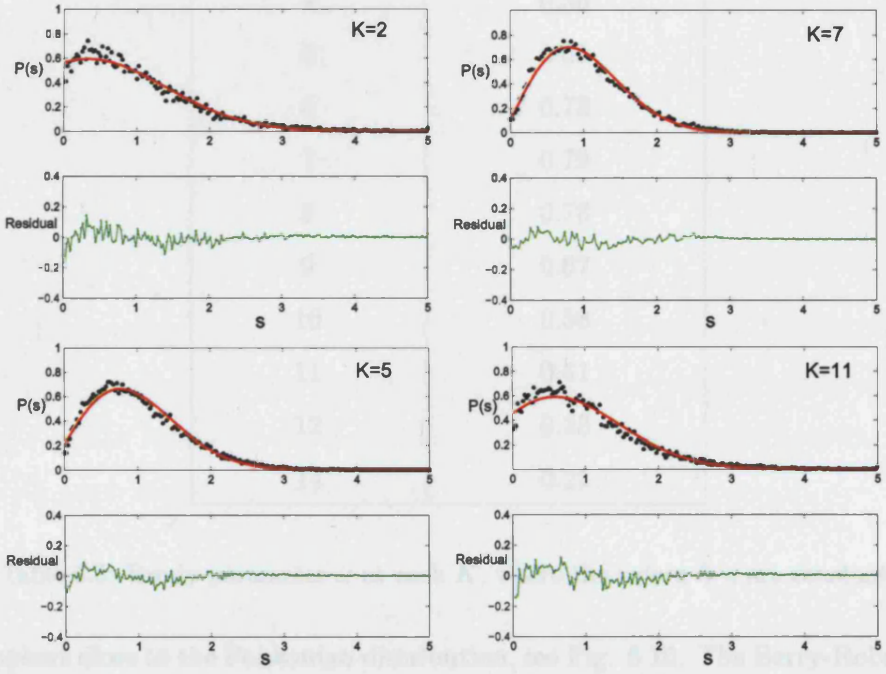

Figure 6.10: The fit to the Berry-Robnik distribution gives rather poor results compared to the Brody fit. The residuals (residual=data-fit) are shown in green colour. Berry-Robnik fits do not especially agree with the NNS at small $s \leq 1$ over all.

Kick strength K	Brody parameter, ω
1	0.03
2	0.31
3	0.42
4	0.56
5	0.66
6	0.73
7	0.79
8	0.78
9	0.67
10	0.58
11	0.41
12	0.33
14	0.21

Table 6.5: Brody parameter ω at each K, where the values $\hbar$, ϵ are constant.

appears close to the Poissonian distribution, see Fig. 6.10. The Berry-Robnik parameter ρ around the maximal chaotic states ($K = 7$ in Figure 6.10) is $\rho \simeq 0.06$ ($\rho = 0$ for GOE) indicating the chaotic fraction in phase space [78].

The Brody parameters obtained for each data set are shown in Table 6.5 and 6.6. The maximal intermediate statistics can be found from the two sets of data: K=7 with constant $\hbar_\epsilon$ and $\hbar$ from 1/8 to 1/12 with constant K_ϵ.

A crossover distribution specified by two parameters is supplementarily introduced for comparison with the Brody distribution. We found that the crossover distribution shows as good agreement with the results as does the Brody distribution and this is shown in Fig. 6.11.

$\hbar$	Brody parameter, ω
1	0.45
1/2	0.59
1/4	0.72
1/6	0.79
1/8	0.84
1/10	0.86
1/12	0.85

Table 6.6: Brody parameter ω at each $\hbar$, where the values K, ϵ are constant.

The crossover distribution was found by Ugajin [100] and demonstrated excellent fitting to the statistics of the system used: a quantum particle in a super-lattice consisting of a disordered layer and a clean layer. The crossover distribution specified by two parameters (ω, η) is given by

$$Q(s;\omega,\eta) = A(\omega,\eta)s^{2\omega}e^{-B(\omega,\eta)s^{1+\eta}} \tag{6.29}$$

with the conditions,

$$\int_0^\infty dsQ(s;\omega,\eta) = 1 \tag{6.30}$$

$$\int_0^\infty dsQ(s;\omega,\eta) = 1. \tag{6.31}$$

The coefficients $A(\omega,\eta)$ and $B(\omega,\eta)$ are given as

$$A(\omega,\eta) = (1+\eta)\frac{\Gamma\left(\frac{2+2\omega}{1+\eta}\right)^{1+2\omega}}{\Gamma\left(\frac{1+2\omega}{1+\eta}\right)^{1+2\omega}} \tag{6.32}$$

and

$$B(\omega,\eta) = \left[\frac{\Gamma\left(\frac{2+2\omega}{1+\eta}\right)}{\Gamma\left(\frac{1+2\omega}{1+\eta}\right)}\right]^{1+\eta}, \tag{6.33}$$

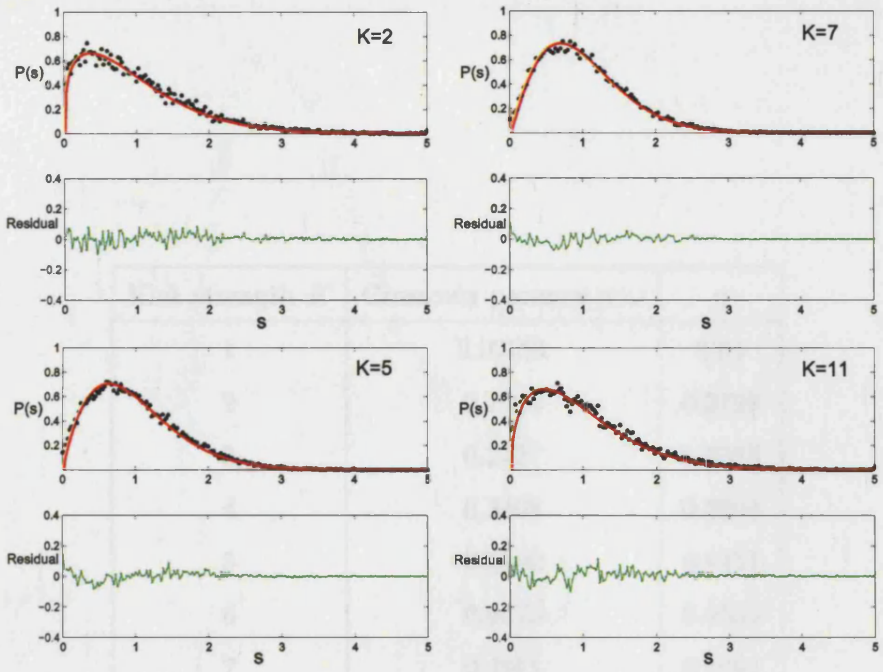

Figure 6.11: Four fits are illustrated for the various K and constant $\hbar_\epsilon$. The crossover distribution shows as good agreement with the results as does the Brody distribution. The residuals (residual=data-fit) are shown in green colour.

where

$$\Gamma(z) = \int_0^\infty t^{z-1} e^{-t} dt \tag{6.34}$$

is the Gamma function. The ω parameter indicates the strength of repulsion between energy levels at small s, while η measures how fast the crossover distribution decays as s increases beyond 1. $Q(s;0,0)$ and $Q(s;1/2,1)$ correspond to Poisson and GOE respectively, whereas $Q(s;1,1)$ corresponds to GUE. Table 6.7 shows the values of two parameters (ω,η), obtained for K from 1 to 14, $\hbar$=1/8 and ϵ=0.04.

For those histograms for constant K_ϵ, both values ω, η change from 0 to

Kick strength K	Crossover parameter ω	η
1	0.02791	0.01
2	0.1404	0.3799
3	0.2427	0.3373
4	0.3408	0.3394
5	0.4102	0.4451
6	0.4475	0.4599
7	0.4971	0.5091
8	0.4874	0.5115
9	0.4091	0.4622
10	0.3452	0.4535
11	0.2143	0.3934
12	0.2041	0.2006
14	0.1504	0.07323

Table 6.7: The crossover parameters, (ω, η) at each K with the constant value of $\hbar = 1/8$, $\epsilon = 0.04$.

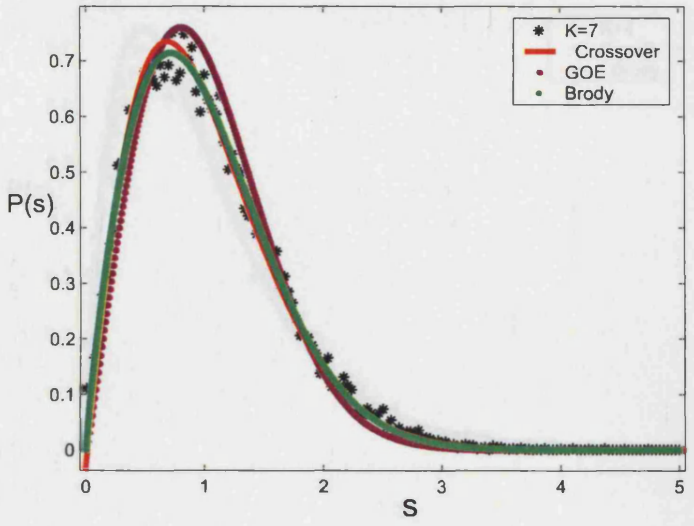

Figure 6.12: The (maximal) intermediate NNS distribution for K=7, $\hbar = 1/8$ and $\epsilon = 0.04$ is shown with the Brody (ω=0.7922), the crossover fit (ω=0.4971, η=0.5091) and GOE for comparison.

0.5 as the kick strength K increases from 1 to 7 then back to 0 as K increases as K increases further to 14.

Fig. 6.12 shows two fits, the Brody and the crossover fit, with our NNS result for K=7, $\hbar = 1/8$ and $\epsilon = 0.04$, which is the closest to GOE in the critical regime. The GOE distribution overlaps for comparison.

Fig. 6.13 illustrates the semi Poisson distribution, $P_{sp}(s) = 4se^{-2s}$, and the NNS result for K=4 with the Brody fit in the critical regime. As far as critical statistics is concerned, our intermediate NNS distributions in the critical regime pass through the point close to the semi Poisson statistics between K=4 and 5 before reaching the maximal intermediate statistics around K=7.

In summary, we found the critical regime from the scaled plot of d against

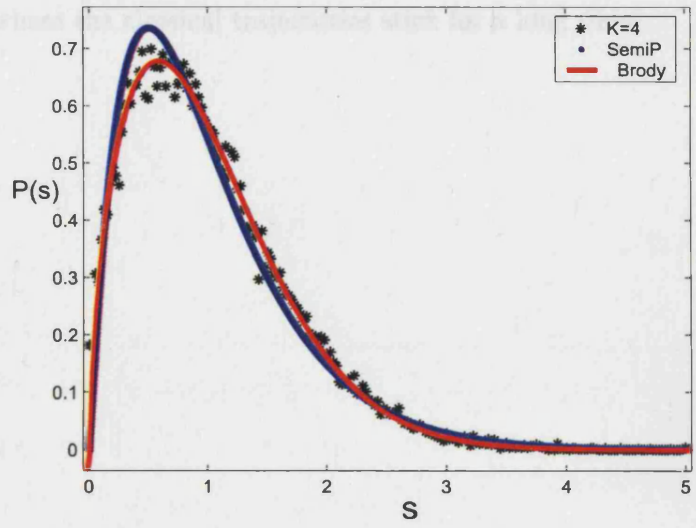

Figure 6.13: The intermediate NNS distribution for K=4, $\hbar = 1/8$ and $\epsilon = 0.04$ is shown with the Brody (ω=0.56) and the semi Poisson curve for comparison.

$\hbar_\epsilon$, and accordingly the existence of critical statistics were speculated by investigating the spectral properties of the 2δ-KR. The Σ_2 statistics and the NNS statistics of our system were investigated in relation to those found at the MIT in disordered metallic systems whose classical dynamics is chaotic. Through the investigation, the critical regime was identified in the transition between the localisation and delocalisation limits. We found that the statical results for the 2δ-KR pass through the point where our statistics resembles the critical statistics (K=4-5 with constant $\hbar = 1/8$, $\epsilon = 0.04$) as proceeding to the maximal intermediate statistics (around K=7). The NNS distribution gradually changes from Poisson to GOE until it reaches the maximal intermediate statistics at the delocalisation border but subsequently returns to Poissonian statistics beyond the critical regime. It can be thought that these intermediate statistics are attributed to the existence of the trapping

regions, where the classical trajectories stick for a long time.

CHAPTER 7

Conclusions

7.1 Overview of the completed work

This thesis investigated two particular Hamiltonian quantum systems, the perturbed-period KR and double-KR. Both of these have classical limits which are chaotic (at large kick strengths). Prior to this work, the ratchet and filtering effect had been investigated using the perturbed-period KR with a rocking potential. It was shown previously that a ratchet effect can be induced in the quantum system in a regime where the corresponding classical phase space is fully chaotic. Previous studies had argued that directed motion would only be possible with a mixed phase space.

As a main presentation in this thesis, the chaotic ratchet and the filter were both further analysed by examining the properties of their Floquet states since the Hamiltonian of the system is time periodic. The eigenstates of the perturbed-period KR show asymmetric momentum probability distributions, qualitatively similar to the asymmetric momentum distributions

seen in wavepackets after dynamical localisation. It has also been shown that the variation of localisation lengths of the eigenstates against the average momentum of each eigenstate is in an excellent agreement with the variation of the classical diffusion correlation $D(p_0)$ as a function of initial momentum.

The numerical simulations for the double KR have been presented and compared with the analytical calculations of the classical diffusion rates as well as the experimental results. One of the remarkable features of the double-KR is the existence of the strong trapping regions, which produces an enhanced filtering effect.

Another important feature seen in the experiments was the reversal of the energy absorption curve as a function of initial momentum, which was shown, in the classical analysis, to result from the global correlation terms. Those quantum numerical results obtained by increasing only the kick strength K while keeping ϵ and $\hbar$ constant also showed the same reversal of the energy curve along with the initial momentum.

The Floquet states corresponding to those quantum results obtained numerically for the double KR have shown similar features, such as the characteristic 'staircase' structure. Keeping ϵ and $\hbar$ constant, the variation of localisation lengths along the average momentum of each eigenstate is also reversed as the kick strength increases, which is analogous to the energy reversal seen in both the classical and experimental results.

The existence of trapping regions has led to other significant findings in the eigenvalue statistics. This investigation was performed by obtaining large number of eigenvalues of the system and this was achieved by running the code in the mid-range computer at UCL. Both the number variance statistics (Σ_2) and the nearest neighbouring spacing distribution were obtained. We found the spectral variances to have an approximately linear

form $\Sigma_2(L) \simeq \chi L$ in a transition regime where the Floquet states delocalise (in other words where they are no longer within a single cell bounded by two trapping regions). The NNS statistics in this localisation- delocalisation border also show a form intermediate between Poisson and GOE.

These results led us to speculate that the eigenvalue statistics for our system are similar to the critical statistics which have been found in a MIT in a disordered system. According to the relation in the MIT, $\Sigma_2(L) \simeq \chi L \simeq \frac{1}{2}(1 - D_2)L$, the expected value of χ for our system is $\Sigma_2(L) \simeq \chi L \simeq 0.125L$, provided the fractal dimension $D_2 \simeq 0.75$. We note that the value 0.75 corresponds very closely to the exponent found for the return probabilities and for the $\hbar$ scaling of our localisation lengths. However, we found that the value of χ in the maximal intermediate statistics is slightly less ($\chi \sim 0.01$). The value of $\chi \simeq 0.125$ is obtained in a transition between the Poisson and the maximal intermediate statistics in the critical regime.

On the other hand, the nearest neighbouring statistics have shown the level spacings distribution to be quite different from the 'semi-Poisson' distribution (which has been found to be in the MIT). The NNS distribution follows the Brody distribution showing good agreement. The NNS distribution also passes the point where the NNS distribution resembles the semi Poisson statistics before reaching the maximal intermediate statistics.

The NNS statistics move from Poisson but do not completely approach GOE. Instead, they show a gradual transition from Poisson to GOE in the critical regimes. These regimes were defined as between the localised and delocalised limits, which were obtained from the relation between the step-size d and the $\hbar\epsilon$. Beyond the two ends of the critical regime, the NNS shows the Poisson distribution. To our knowledge, the statistics in the critical regime presented in this thesis, in particular the relation between the fractal

dimension and the level number statistics, have never been seen in a KAM system.

7.2 Further directions and possible applications

There are many possibilities to extend the work presented in this thesis. The effect of noise, which is known to destroy dynamical localisation, on the ratchet current can be investigated by adding the noise into the rocking ratchet system. Coupling more than two quantum kicked rotors under double kicking, the trapping effect and other possible interactions between them can be explored. By putting the period between kicks T as integer multiples of π, a quantum resonance effect on energy absorption of an atomic cloud will be of interest.

As far as NNS statistics are concerned, analytical calculation to show whether the band structure in the double-KR is at all analogous to the Anderson model in solid state physics might be interesting. The matter of where the exponent 0.75 in the scaling factor of the step-height d as a power-law with $\hbar\epsilon$, $d \simeq (\hbar\epsilon)^{0.75}$ comes from is yet to be understood.

One other possible direction of the study of the double kick system is an exploration of Bose-Einstein condensation by adding a non linear term to the Hamiltonian in order to make atoms interact with each other. This can be simulated by evolving a single eigenstate starting in the trapping region.

The momentum dependence of the diffusion correlations allows a possible application for both the perturbed KR and the double KR system (only in the regime where C_1 correlation is dominant). Since the localisation lengths

in the quantum system are dependent on the local diffusion constant in momentum, both the rate at which energy is absorbed and the length of time the energy is absorbed over are controlled by a particle's initial momentum. This suggests a possible device for filtering the momenta of cold atoms in the context of atomic manipulation, such as an atomic chip. Furthermore, it has explicitly been shown in this thesis that the double kick system demonstrates a much enhanced velocity selective effect due to the existence of the trapping effect. Therefore, the double kick system can produce better velocity selection.

Bibliography

[1] S. Fishman, D. R. Grempel, R. E. Prange, PRL **49**, 509 (1982).

[2] Shmuel Fishman, 'Quantum Localisation', in Lecture notes of the Scottish Summer School (1994).

[3] G. Casati, B. V. Chirikov, Izraelev F. M., and I. Ford in Lecture notes in Physics, Springer, Berlin , **93** , 334 (1979).

[4] B. V. Chirikov, A universal instability of many-dimensional oscillator systems. Phys. Rep. **52** , 263 (1979).

[5] E. Ott, 'Chaos in dynamical systems', Cambridge University Press (1993).

[6] A. B. Rechester, R. B. White, PRL **44**, 1586 (1980) .

[7] A. B. Rechester, M. N. Rosenbluth, R. B. White, PRA **23**, 2664 (1981).

[8] A. J. Lichtenberg, M. A. Lieberman, 'Regular and chaotic dynamics', Springer-Verlag, New York (1992).

[9] R. Blümel, W. P. Reinhardt, 'Chaos in atomic physics', Cambridge University Press (1997).

[10] F. M. Izrailev, D. L. Shepelyanskii, Sov. Phys. Dokl. **24**, 996 (1979).

[11] F. M. Izrailev, D. L. Shepelyanskii, Theor. Math. Phys. **43**, 553 (1980).

[12] D. L. Shepelyansky, PRL **56**, 677 (1986).

[13] D. R. Grempel, R. E. Prange, S. Fishman, PRA **29**, 1639 (1984).

[14] M. Griniasty, S. Fishman, PRL **60**, 1334 (1988).

[15] D. R. Graham, M. Schlautmann and P.Zoller, PRA **45**, R19 (1992).

[16] F. L. Moore, J. C. Robinson, C. F. Bharucha, P. E. Williams, M. G. Raizen, PRL **73**, 2974 (1994).

[17] J. C. Robinson, C. Bharucha, F. L. Moore, R. Jahnke, G. A. Georgakis, Q. Niu, M. G. Raizen, PRL **74**, 3963 (1995).

[18] P. J. Bardroff, I. Bialynicki-Birula, D. S. Krahmer, G. Kurizki, E. Mayr, P. Stifter, W. P. Schleich, PRL **74**, 3959 (1995).

[19] F. L. Moore, J. C. Robinson, C. F. Bharucha, B. Sundaram, and M. G. Raizen, PRL **75**, 4598 (1995).

[20] C. F. Bharucha, J. C. Robinson, F. L. Moore, B. Sundaram, Q. Niu, M.G. Raizen, PRE **60**, 3881 (1999).

[21] B. G. Klappauf, W. H. Oskay, D. A. Steck, M. G. Raizen, PRL **81**, 1203 (1998).

[22] V. Milner, D. A. Steck, W. H. Oskay, M. G. Raizen, PRE **61**, 7223 (2000).

[23] D. A. Steck, V. Milner, W. H. Oskay, M. G. Raizen, PRE **62**, 3461 (2000).

[24] D. A. Steck, W. H. Oskay, M. G. Raizen, PRL **88**, 120406 (2002).

[25] W. H. Oskay, D. A. Steck, M. G. Raizen, Chaos, Solitons and Fractals **16**, 409-416 (2003).

[26] J. Ringot, P. Szriftgiser, J. C. Garreau, D. Dalande, PRL **85**, 2741 (2000)

[27] B. G. Klappauf, W. H. Oskay, D. A. Steck, M. G. Raizen, PRL **81**, 4044 (1998).

[28] W. H. Oskay, D. A. Steck, V. Milner, B. G. Klappauf, M. G. Raizen, Optics Commun. **179**, 137-148 (2000).

[29] D. A. Steck, W. H. Oskay, M. G. Raizen, Science **293**, 274 (2001)

[30] M. K. Oberthaler, R. M. Godun, M. B. D'Arcy, G. S. Summy, K. Burnett, PRL **83**, 4447 (1999).

[31] R. M. Godun, M. B. D'Arcy, M. K. Oberthaler, G. S. Summy, K. Burnett, PRA **62**, 013411 (2000).

[32] M. B. D'Arcy, R. M. Godun, M. K. Oberthaler, D. Cassettari, G. S. Summy, PRL **87**, 074102 (2001).

[33] S. Schlunk, M. B. D'Arcy, S. A. Gardiner, G. S. Summy, PRL **90**, 124102 (2003).

[34] S. Schlunk, M. B. D'Arcy, S. A. Gardiner, D. Cassettari, R. M. Godun, G. S. Summy, PRL **90**, 054101 (2003).

[35] R. D. Astumian, Scientific American **56**, July (2001).

[36] R. P. Feynman, R. B. Leighton, M. Sands, The Feynman lectures on Physics, Addison-Wesley, Reading (1963).

[37] P. Reimann, PRL **86**, 4992 (2001).

[38] R. D. Astumian, Science **276**, 917 (1997).

[39] P. Reimann, Phys. Rep. **361**, 57 (2002).

[40] T. S. Monteiro, P. A. Dando, N. A. C. Hutchings and M. R. Isherwood, PRL **89**, 194102 (2002).

[41] N. A. C. Hutchings, M. R. Isherwood, T. Jonckheere, T. S. Monteiro, PRE **70**, 036205 (2004).

[42] D. Delande, 'Quantum chaos in atomic physics', Coherent Atomic Matter Waves V. XXII (Proceedings).

[43] T. Jonckheere, M. R. Isherwood and T. S. Monteiro, PRL **91**, 253003 (2003).

[44] T. Cheon, P. Exner, P. Seba, *cond-mat/0203241.*

[45] P. H. Jones, M. Goonasekera, H. E. Saunders-Singer, T. S. Monteiro and D. R. Meacher *physics/0504096*

[46] T. Dittich, R. Ketzmerick, M. F. Otto, H. Schanz, Ann.phys. (Leipzig)**9**, 1 (2000).

[47] H. Schanz, M. F. Otto, R. Ketzmerick, T. Dittich, PRL **87**, 070601 (2001).

[48] S. Flach, O. Yevtushenko, Y. Zolotaryuk, PRL **84**,2358 (2000).

[49] E. Hinds, C. J. Vale, M. G. Boshier, PRL **86**, 1462 (2001).

[50] W. Hänsel, P. Hommelhoff, T. W. Hänsch, J. Reichel, Nature (London) **413**, 498 (2001).

[51] J. H. Shirley, Phys. Rev. **138** B979 (1965).

[52] R. Ketzmerick, K. Kruse, T. Geisel, Physica D **131**, 247 (1999).

[53] G. Hur, C. E. Creffield, P. H. Jones, T. S. Monteiro, PRA **72**, 013403 (2005).

[54] D. R. Meacher, Contemp. Phys. **39**, 329 (1998).

[55] G. Grynberg, C. Mennerat-Robilliard, Phys. Rep. **355**, 335 (2001).

[56] P. H. Jones, M. Goonasekera, H. E. Saunders-Singer, D. R. Meacher, *quant-phys/0309149*

[57] P. H. Jones, M. Stocklin, G. Hur, T. S. Monteiro, PRL **93**, 223002 (2004)

[58] M. Stocklin, T. S. Monteiro, *physics/0408088/*

[59] M. Stocklin, Ph.D. thesis in preparation (2006).

[60] T. W. Hänsch, A. L. Schawlow, Optics. Commun. **13**, 68 (1975).

[61] K. Husimi, Proc. Phys. Math. Soc. Jpn. **22**, 264 (1940).

[62] E. Prugovecki, Ann. Phys. (New York) **110**, 102 (1978).

[63] M. Goonasekera 'Symmetry breaking and directed transport of cold atoms in optical lattices', Ph.D thesis, University College London (2004).

[64] Laser Cooling Group at University College London. (http://lasercooling.phys.ucl.ac.uk/).

[65] B. G. Klappauf, W. H. Oskay, D. A. Steck, M. G. Raizen, Physica D **131**, 78 (1999).

[66] P. H. Jones, M. Goonasekera, H. E. Saunders-Singer, D. R. Meacher, manuscript in preparation.

[67] D. A. Steck, 'Quantum chaos, transport and decoherence in atom optics', Ph.D thesis, University of Texas at Austin (2001).

[68] M. Isherwood 'Theory of chaotic Hamiltonian ratchets', Ph.D thesis, University College London (2004).

[69] D. A. Steck, 'Classical and Quantum Chaos', in Lecture notes for Los Alamos Summer School (2002).

[70] C. Creffield, Europhys. Lett. **66**, 631 (2004).

[71] E. Wigner, Ann. Math. **62**, 548 (1955).

[72] E. Wigner, Ann. Math. **65**, 203 (1957).

[73] (edited by) C. E. Porter, 'Statistical Theories of Spectra', Academic, New York (1965).

[74] M. L. Mehta, 'Random Matrices and the Statistical Theory of Energy Levels', Academic, New York (1967).

[75] H-J Stöckmann, 'Quantum Chaos *an Introduction*', Cambridge (1999).

[76] Fritz Haake, 'Quantum signatures of chaos', Springer-Verlag (1992).

[77] T. A. Brody, T. Flores, J. B. French, P.A. Mello, A. Pandy, S. S. M. Wong, Rev. Mod. Phys. **53**, 385 (1981).

[78] M. V. Berry, M. Robnik, J. Phys. A **17**, 2413 (1984).

[79] O. Bohigas, M. J. Giannoni, C. Schmit, PRL **52**, 1 (1984)

[80] M. Feingold, S. Fishman, D. R. Grempel, R. E. Prange, PRB **31**, R6852 (1985).

[81] F. M Izrailev, PRL **134A**, 13 (1988).

[82] F. M Izrailev, Phys. Rep. **196**, 299 (1990).

[83] F. M Izrailev, PRL **56**, 541 (1986).

[84] G. Casiti, B. V. Chirikov, I. Guarneri, F. M. Izrailev, PRE **48**, R1613 (1993).

[85] G. Casiti, F. M. Izrailev, L. Molinari, PRL **64**, 1851 (1990).

[86] G. Casiti, F. M. Izrailev, L. Molinari, J. Phys. A:Math. Gen. **24**, 4755 (1991).

[87] B. I. Shklovskii, B. Shapiro, B.R. Sears, P. Lambrianides, H. B. Shore, PRB **47**, 11487 (1993).

[88] D. Braun, G. Montambaux, M. Pascaud, PRL **81**, 1062 (1998).

[89] T. Jonckeere, B. Grémaud, D. Delande, PRL **81**, 2442 (1998).

[90] J. T. Chalker, I. V. Lerner, R. A. Smith, PRL **77**, 554 (1996).

[91] B. Huckestein, L. Schweitzer, PRL **72**, 713 (1994).

[92] E. B. Bogomolny, U. Gerland, C. Schmidt, PRE **59**, R1315 (1999).

[93] A. M. Garcia-Garcia, J.J.M. Verbaaschot, PRE **67** , 046104 (2003).

[94] S. N. Evangelou, J. L. Pichard, PRL **84**, 1643 (2000).

[95] I. Varga, D. Braun, PRE **61**, R11859 (2000).

[96] V. E. Kravtsov, K. A. Muttalib, PRL **79**, 1913 (1997).

[97] R. Ketzmerick, G. Petschel, T. Geisel, PRL **69**, 695 (1992).

[98] R. Ketzmerick, L. Hufnagel, F. Steinbach, M. Weiss, PRL **85**, 1214 (2000).

[99] C. Creffield, G. Hur, T. S. Monteiro, *physics/0504074*.

[100] R. Ugajin, PRE **68**, 16219 (2003).

Appendix A

Papers

Three papers are presented in this appendix:

Atoms in Double-delta-Kicked Periodic Potentials: Chaos with Long-Range Correlations.
P. H. Jones, M. M. Stocklin, G. Hur, T. S. Monteiro
Phys. Rev. Lett. 93, 223002 (2004)

Chaotic quantum ratchets and filters with cold atoms in optical lattices: Analysis using Floquet states.
G. Hur, C. E. Creffield, P. H. Jones, T. S. Monteiro
Phys. Rev. A 72, 013403 (2005)

Localisation-delocalisation transition in a system of quantum kicked rotors.
C. E. Creffield, G. Hur, T. S. Monteiro
physics/0504074 (to appear in PRL in 2006)

PRL 93, 223002 (2004) PHYSICAL REVIEW LETTERS week ending 26 NOVEMBER 2004

Atoms in Double-δ-Kicked Periodic Potentials: Chaos with Long-Range Correlations

P. H. Jones, M. M. Stocklin, G. Hur, and T. S. Monteiro
Department of Physics and Astronomy, University College London, Gower Street, London WC1E 6BT, United Kingdom
(Received 30 April 2004; published 22 November 2004)

We report an experimental and theoretical study of the dynamics of cold atoms subjected to pairs of closely spaced pulses in an optical lattice. For all previously studied δ-kicked systems, chaotic classical dynamics shows diffusion with short-time (2- or 3-kick) correlations; here, chaotic diffusion combines with new types of long-ranged global correlations, between all kick pairs, which control transport through trapping regions in phase space. Correlations are studied in the classical regime, but the diffusive behavior observed in experiment depends on the quantum dynamical localization.

DOI: 10.1103/PhysRevLett.93.223002 PACS numbers: 32.80.Pj, 05.45.Mt, 05.60.-k

The "δ-kicked particle" (δ-KP) is one of the most studied experimental and theoretical paradigms of classical Hamiltonian chaos. Of particular interest in recent years has been the theoretical [1,2] and experimental [3] investigations of the suppression of the classical diffusive process in its quantum counterpart, the quantum δ-kicked particle (δ-QKP). This phenomenon is generally termed "dynamical localization" (DL). A broad range of further interesting physical regimes was subsequently investigated experimentally with cold atoms in optical lattices: controlled decoherence [4], "quantum accelerator modes" [5,6], and delocalization induced by nonperiodic kicking [7].

In a usual realization of the δ-KP, an ensemble of particles all with initial momenta P_0, is kicked periodically, with period T, by a sinusoidal potential $V(x,t) = -K\cos x\sum_N \delta(t - NT)$. The momentum of a given particle changes with time by means of a series of impulses $\Delta P_N = \sum_{i=1}^{N} K\sin x_i$. The average energy of the ensemble grows diffusively; $\langle (P_N - P_0)^2\rangle = \langle (\Delta P_N)^2\rangle = DN$, where D is the momentum diffusion rate. In the corresponding quantum system (like the cold atom experiments), the diffusion is arrested by dynamical localization after a time scale $t^* \sim D/\hbar^2$ [8] and the average momenta "freeze" at a value $\langle (\Delta P_N)^2\rangle \sim Dt^*$.

If we neglect all correlations between kicks, we can approximate D by the well-known value $D_0 = \frac{K^2}{2}$. However, the chaotic diffusion is not entirely uncorrelated [9,10]: the average $\langle (\Delta P_N)^2\rangle$ is clearly affected by correlations between the impulse at kick i and the impulse at a later kick; one can evaluate averages like $C_k = 2K^2\langle \sin x_i \sin x_{i+k}\rangle$ and correct the diffusion rate so $D = D_0 + \sum_k C_k$ [9,10]. There are experimentally observed effects [11] in cold atom experiments due largely to 2-kick and 3-kick correlations (C_2 and C_3, respectively). In [12] it was further shown that, if the pulses are unequally spaced, the 2-kick correlations yield a local correction to the diffusion, i.e., $D \equiv D(P_0, t)$: D depends on both time and P_0. But in all these experiments, unsurprisingly, for strong chaos only *short-ranged* (i.e., 2- or 3-kick) correlations contribute appreciably.

Here we report the first experimental and theoretical study of the 2δ-kicked particle (2δ-KP): a cloud of cesium atoms is exposed to a periodic sequence of *pairs* of closely spaced kicks. At the outset, one might expect that the diffusive behavior here could be analyzed within the framework used in [11,12], of diffusion with correlations between short sequences of two or three kicks, whether local or otherwise. However, this approach fails to explain the experimental results. Further investigation showed that the chaotic diffusion was rather different from that seen in all previously studied kicked systems. Here, we find new corrections, which appear in families correlating all kicks. These corrections are individually very weak, but accumulate with time to eventually dominate the diffusive process. Moreover, these "global" correlations can be associated with specific physical phenomena, namely, the escape from and through momentum "trapping" regions observed in the experiment. The experimental results depend on which classical regime is dominant when quantum localization arrests the diffusion.

The classical behavior of the 2δ-KP is given by iterating a 2-kick map:

$$x_{j+1} = x_j + p_j\tau, \qquad p_{j+1} = p_j + K\sin x_{j+1},$$
$$x_{j+2} = x_{j+1} + p_{j+1}\epsilon, \qquad p_{j+2} = p_{j+1} + K\sin x_{j+2}, \tag{1}$$

where ϵ is a very short-time interval between two kicks in a pair and τ is a much longer time interval between the pairs.

The experimental apparatus has been described in [13] and consists of a cloud of cesium atoms collected in a standard 6-beam magneto-optical trap (MOT) and cooled in an optical molasses to a temperature of 6 μK. The sinusoidal potential $V(x,t)$ is formed by two counterpropagating laser beams incident on the cloud with parallel polarizations. These are derived from a titanium sapphire laser, have an intensity of $4 \times 10^3 I_{\mathrm{sat}}$ ($I_{\mathrm{sat}} = 1.12\ \mathrm{mW\,cm^{-2}}$, the saturation intensity) in each beam and are detuned 2000Γ ($\Gamma = 2\pi \times 5.22$ MHz, the natural

linewidth) below the D2 transition on cesium. The potential is switched on using acousto-optic modulators (AOMs) to create pulses ("kicks") as short as $t_p = 300$ ns, and each beam is controlled by a separate AOM so that a frequency difference Δf may be imposed upon the two beams and the potential moves with constant velocity in the laboratory frame. In this way we may explore the momentum dependence of the diffusion constant, as in the rest frame of the potential the atomic momentum distribution has a nonzero mean value $P_0 \propto \Delta f$.

Kicks are applied at times nT and $nT + \Delta$ (for integer n) where $T = 9.47$ μs, while values of $\Delta = 0.45$ to 1.5 μs were used. Variables were rescaled as usual for these experiments [3] with the minor difference that time was rescaled by the time between kick pairs, T, rather than the time between kicks as in [3]. Hence scaled kick intervals are $\epsilon = \Delta/T \simeq 0.047$ to 0.16 and $\tau = 1 - \epsilon$. For these parameters and with intensity and detuning as above, we have an effective value of $\hbar = 1$ while the kick strength, $K = 3.3$ ($\pm$ 10% due mainly to the uncertainty in measuring the intensity in the laser beams). Up to $N = 100$ kicks were applied before the cloud of atoms was allowed to evolve freely in the dark for 15 ms. A pair of near-resonant imaging beams were then switched on and the fluorescence imaged on a charge-coupled device (CCD) camera. From the spatial distribution of the fluorescence the momentum distribution was extracted and $\langle (P_N - P_0)^2 \rangle$ calculated.

It is instructive to consider what happens to atoms for which $\pm \epsilon P_0 = (2m + 1)\pi$, $m = 0, 1, \ldots$; these particles experience an impulse $K \sin x$ followed by another at $\simeq K \sin(x + \pi)$ which in effect cancels the first. Conversely, for $\pm \epsilon P_0 = 2m\pi$, a series of near-identical kicks produces initially rapid energy growth. Figure 1 shows surface of section (SOS) diagrams for $K = 7$, $\epsilon = 0.05$.

The experimental results are shown in Fig. 2. It may be seen in Fig. 2(a) that atoms prepared in the momentum-trapping regions with $\pm P_0 \simeq (2m + 1)\pi/\epsilon$ absorb essentially no energy; for $\pm P_0 \simeq 2m\pi/\epsilon$, they absorb about twice the energy of the standard δ-KP. However, in Fig. 2(c), we see a reversal of this behavior; atoms prepared in the fast-diffusion regions with $\pm P_0 \simeq 2m\pi/\epsilon$ absorb the least energy, while those prepared near the trapping regions absorb the most energy. This counterintuitive result motivates a closer look at the chaotic classical transport for this system.

To calculate the classical diffusion rate, D, where $D(t)t = \langle (\Delta P_t)^2 \rangle$, our starting point is a similar expression to that obtained in 1980 by Rechester and White [10],

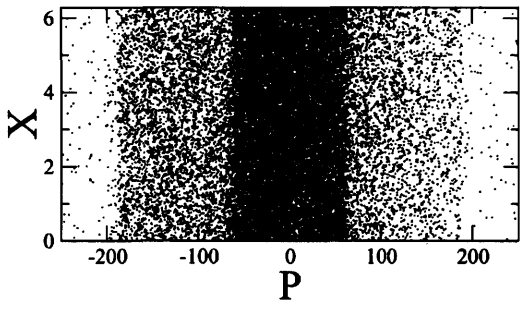

FIG. 1. Classical surface of section plots for a cloud of particles prepared initially with $P_0 = 0$. The SOS illustrates the trapping of trajectories in phase space regions for which the momenta $p\epsilon \simeq \pm(2m + 1)\pi$.

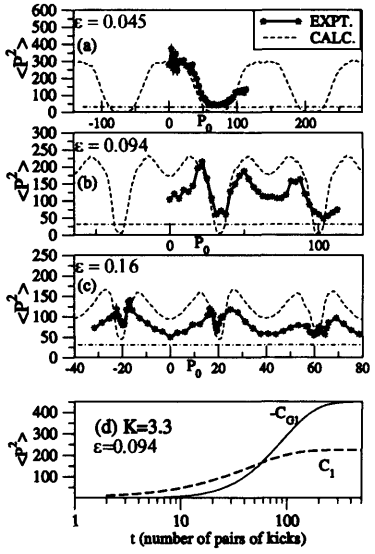

FIG. 2. (a)–(c) Experimental results for 2δ-KP realization with cesium atoms. Graphs show energy absorbed after dynamical localization ($K = 3.3$, $\hbar_{\text{eff}} = 1$) by clouds of atoms with different initial average momentum P_0 (relative to the optical lattice). In every case, the atom cloud initially had $\langle p^2_{t=0} \rangle \simeq 30$ (dot-dashed line). The dashed lines represent a classical simulation for similar parameters. With increasing ϵ, the minima (maxima) in the energy flip into maxima (minima). (a) Here, the quantum break time $t^* \ll 1/(K\epsilon)^2$. Atoms prepared near the momentum-trapping regions [$P_0 \simeq (2m + 1)\frac{\pi}{\epsilon}$] absorb no energy; those with $P_0 \simeq 2m\frac{\pi}{\epsilon}$ absorb about twice as much as the standard δ-KP. (b) Trapping now occurs only very close to the resonant condition [$P_0\epsilon = (2m + 1)\pi$]. (c) $t^* > 1/(K\epsilon)^2$. Experiments show a near reversal of the behavior in (a): atoms prepared near trapping regions have absorbed the most energy; atoms prepared farthest from trapping regions absorb *the least* energy. (d) With an increasing number of kicks, the kick-to-kick correction C_1 [which is dominant in (a)] is overtaken by the global long-ranged correlation C_{G1} [which dominates the graph in (c)]. At short times, C_1 grows linearly, while C_{G1} grows quadratically.

for the ordinary standard map:

$$\langle(\Delta P_t)^2\rangle = \sum_{m_t^{(1,2)}=-\infty}^{\infty} \cdots \sum_{m_1^{(1,2)}=-\infty}^{\infty} \int_0^{2\pi} \frac{dx_t^{(1,2)}}{2\pi} \cdots \int_0^{2\pi} \frac{dx_1^{(1,2)}}{2\pi} (\Delta P_t^{(2)})^2 \prod_{j=1}^{t} e^{im_j^{(2)}[x_j^{(2)} - x_j^{(1)} - \epsilon(P_0 + \Delta P_j^{(1)})]} e^{im_j^{(1)}[x_j^{(1)} - x_{j-1}^{(2)} - \tau(P_0 + \Delta P_{j-1}^{(2)})]}. \tag{2}$$

Here, however, we introduce superscripts (1) and (2) to differentiate the first and the second kicks in the pair (see [14] for details). The $2t$ sets of m_j coefficients arise from the 2π periodicity in position space and t denotes the number of pairs of kicks. Note that since the duration of each 2-kick cycle, in scaled units, equals $\tau + \epsilon$, the actual (scaled) time after t kick pairs corresponds to $t(\tau + \epsilon)$. In our experiment, $\tau + \epsilon = 1$; hence t is also the scaled time. Physical time (in μs) is tT, where $T = 9.47$ μs. The calculation above simplifies considerably once we realize that only terms with $|m_j| < 2$ give a contribution. The random walk term $D_0 = K^2/2$ can be recovered from setting all $m_j = 0$, but due to our definition of time in kick pairs, the uncorrected energy $\langle(P - P_0)^2\rangle \simeq K^2 t$. If we set any one of the $m_j^{(2)}$ coefficients to ± 1 (all others to zero) and consider the $2K^2 \sin x_j^{(2)} \sin x_j^{(1)}$ term in $(\Delta P_t^{(2)})^2 = K^2 \sum_{i,j} \sin x_i \sin x_j$ we easily obtain a kick-to-kick correlation, C_1 [14].

$$C_1(t, P_0) = K^2 \cos P_0\epsilon [J_0(K\epsilon) - J_2(K\epsilon)] \times \sum_{j=1}^{t} (J_0(K\epsilon))^{2j-2} \tag{3}$$

This is zero for all previously studied δ-kicked systems. Note that C_1 is a function of t, ϵ, and K but is independent of τ. This is the case with all important correlations.

To correct the energy, we simply evaluate $\langle(P_t - P_0)^2\rangle = Dt = K^2 t + C_1(t, P_0)$. For short times, C_1 grows linearly with time and can be approximated to $C_1 \simeq K^2 t \cos\epsilon P_0$, while for longer times it saturates to a constant value of $\frac{1}{1-J_0^2}$, after a time $t_1 \sim \frac{10}{(K\epsilon)^2}$. The experimental data of Fig. 2(a) are the most straightforward to understand: here, $t_1 \sim 200$ kick pairs and $t^* \simeq 20$ kick pairs, so quantum localization arrests the diffusion in a regime where C_1 is linear and dominant over other correlations. Figure 2(a) approximately follows the formula $\langle(P_t - P_0)^2\rangle \simeq K^2 t(1 - \cos\epsilon P_0)$. If we take $t \simeq 20$ kick pairs we get a cosine oscillation of amplitude $\simeq 200$; Fig. 2(a) shows a cosine oscillation of order $\simeq 150$.

However, the experiment in Fig. 2(c) shows a reversal of this behavior, which cannot be explained by the 2δ-KP kick-to-kick correlation. Looking once again at Eq. (2) with a single $m_j^{(2)} = \pm 1$, we find that the *whole* collection of terms $\sum_{j,k} 2K^2 \sin x_j^{(2)} \sin x_k^{(r)}$ in the $(\Delta P_t^{(2)})^2$ summation ($r = 1, 2$, $k < j$ but otherwise arbitrary) gives small but nonzero contributions [14]. For each $x_k^{(r)}$ we obtain a correction of the form $2K^2 \cos P_0\epsilon J_1^2(K\epsilon) \times \sum_j (J_0(K\epsilon))^{2j-3}$. Each term is negligibly small [$O(K\epsilon)^2$ relative to C_1]. But since we sum over all $x_k^{(r)}$, their numbers accumulate with time and the net contribution of this global correlation family is

$$-C_{G1}(t, P_0) = 2K^2 \cos(P_0\epsilon) J_1^2(K\epsilon) \sum_{j=1}^{t} (2j - 2)(J_0(K\epsilon))^{2j-3}. \tag{4}$$

Though negligible at short times, this term grows quadratically at small t and eventually overtakes the kick-to-kick correlation to saturate at a value twice that of C_1. It has opposite sign to C_1; we interpret it as a term which reflects the gradual dephasing of the resonant effects of C_1 at $P_0\epsilon \sim (2m + 1)\pi$. At long times the behavior is dominated by C_{G1}, and hence the energy absorption is *maximal* for particles prepared near $P_0\epsilon \simeq \pm(2m + 1)\pi$.

Figure 2(b) corresponds to a particularly interesting regime, where $C_1 \sim C_{G1}$. The $\cos P_0\epsilon$ correction is mostly canceled, exposing a series of narrow dips in the energy. The origin of these dips is in a series of terms $C_{Pn} \propto \cos nP_0\epsilon$, $n = 2, 3, 4, \ldots$. When summed, these produce behavior reminiscent of the Poisson-sum formula $\sum_n (-1)^n \cos nP_0\epsilon = \sum_m \delta(P_0\epsilon - (2m + 1)\pi)$. The amplitudes of the C_{Pn} terms vary with time, and only a finite number of harmonics contributes at any given time. Hence we get a series of broadened peaks. The Poisson terms are obtained from setting more than one $m_j^{(2)}$ coefficient to ± 1. The total sum of $m_j^{(2)}$ coefficients gives the Poisson order n of $\cos nP_0\epsilon$ terms. These terms come in two families analogous to C_1 and C_{G1}, depending on which type of sine product is considered. Reference [14] contains details.

$$C_{Pn}(t, P_0) \propto K^2 \cos(nP_0\epsilon) F_n(t) \prod_m J_1^2(mK\epsilon). \tag{5}$$

$F_n(t)$ is a time function which grows as $\sim t^n$ for C_{Pn} and $\sim t^{n+1}$ for C_{Pn}^G. C_{Pn} are $O(K\epsilon)^{2n-2}$ and contribute when $t^n(K\epsilon)^{2n-2} \sim 1$. C_{Pn}^G are $O(K\epsilon)^{2n}$ and contribute when $t^{n+1}(K\epsilon)^{2n} \sim 1$. For each n the global correlation always dominates at long times.

In Fig. 3 we compare numerical (classical) calculations at $K = 7$, $\epsilon = 0.05$, with the behavior predicted by the correlations. In Fig. 3(a) we look at short times and see that we can model the energy absorption by including only the three lowest order diffusive corrections, i.e., those which increase linearly or quadratically in time

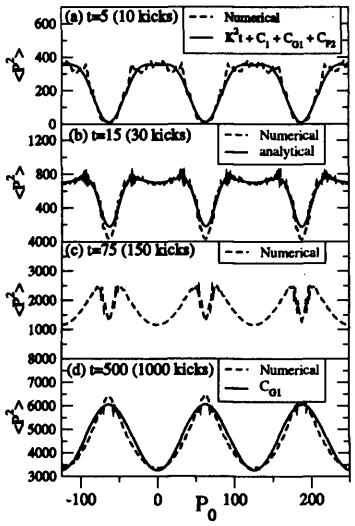

FIG. 3. The energy absorbed by an ensemble of 100 000 classical particles, all with $p = P_0$ at $t = 0$, as a function of initial momentum (dashed line). These numerics are superposed with analytical formulas obtained for the diffusion (solid line). $K = 7$, $\epsilon = 0.05$, in every figure, but the number of kick pairs (t) varies. Note the behavior in the trapping region $P_0 \simeq \pi/\epsilon \simeq 60$: the energy absorbed is a minimum at short times but turns into a maximum at long times. (a) Results at short time (10 kicks), dominated by the 1-kick correlation C_1. (b) Results at a time for which C_1 competes with the global dephasing family C_{G1}. This exposes the "Poisson-sum-formula" corrections: a family of corrections of the form $C_{Pn} \propto \cos nP_0\epsilon$ ($n \geq 2$) combine to give a series of inverted peaks in the trapping regions. (c) All three corrections C_P, C_1, and C_{G1} compete. (d) At $t > 500$ the longest lived correction, C_{G1}, dominates. The Poisson corrections have changed sign: the inverted peaks of (c) (indicating trapping) have "flipped over" to give a series of positive peaks.

(C_1, C_{G1}, C_{P2}). At later times we must include all the terms up to order $\sim J_1^{10}$ and $n = 4$: the inverted peaks corresponding to the trapping regions are quite well reproduced in Fig. 3(b). At even later times such as in Fig. 3(c) higher-order terms are needed for good agreement. At extremely long times, shown in Fig. 3(d), we obtain good results simply from the leading global family C_{G1}. It is found that while the C_{Pn} Poisson terms contribute to increasing the size of the downward peaks in all cases and thus favor trapping of the atoms, their global partners always act to oppose this and thus the peaks invert at long times. If $\tau \gg \epsilon$, any τ dependent correlations are negligible. We have tested the insensitivity of the classical diffusion to the value of τ by repeating the numerical calculation in Fig. 3 with $\tau = (1 - \epsilon)$, $(2 - \epsilon)$, and $(10 - \epsilon)$. The changes are of order 10%–20%.

In conclusion, we have presented and analyzed an experimental realization of a 2δ-KP and shown that it corresponds to a type of classical diffusion quite different from the standard map. The transport investigated here does not resemble previously studied examples of correlated transport. It is quite generic and is unusual in combining strong chaotic diffusion with very long-ranged correlations. A number of questions remain open; certain aspects of the interactions and lifetimes of the different types of classical correlations are not yet well understood.

The dynamical localization determines in what diffusive regime the kick system is arrested. The key features of this experiment can be modeled qualitatively in Fig. 2 by adjusting the number of kicks in the classical numerics. However, the quantum behavior of the 2δ-KP is not fully understood. Further investigation of the DL in this system is necessary: its Floquet states are localized, like in the standard δ-KP. But in the latter, localization lengths, L, are quite uniform with exponential localization and $L \sim \frac{D}{\hbar}$, while in the 2δ-KP, values of L can vary by about 3 orders of magnitudes for the parameters considered here.

The authors thank Thibaut Jonckheere for helpful discussions. This work was supported by the EPSRC.

[1] G. Casati, B.V. Chirikov, F.M. Izraelev, and J. Ford, in *Lecture Notes in Physics* Vol. 93 (Springer, Berlin, 1979), p. 334.
[2] S. Fishman, D.R. Grempel, and R.E. Prange, Phys. Rev. Lett. **49**, 509 (1982).
[3] F.L. Moore, J.C. Robinson, C.F. Bharucha, B. Sundaram, and M.G. Raizen, Phys. Rev. Lett. **75**, 4598 (1995).
[4] B.G. Klappauf, W.H. Oskay, D.A. Steck, and M.G. Raizen, Phys. Rev. Lett. **81**, 1203 (1998).
[5] M.B. d'Arcy, R.M. Godun, M.K. Oberthaler, D. Cassettari, and G.S. Summy, Phys. Rev. Lett. **87**, 74102 (2001).
[6] S. Wimberger, I. Guarneri, and S. Fishman, Phys. Rev. Lett. **92**, 084102 (2004).
[7] P. Szriftgiser, J. Ringot, D. Delande, and J.-C. Garreau, Phys. Rev. Lett. **89**, 224101 (2002).
[8] D.L. Shepelyansky, Phys. Rev. Lett. **56**, 677 (1986).
[9] D.L. Shepelyansky, Physica (Amsterdam) **28D**, 103 (1987).
[10] A.B. Rechester and R.B. White, Phys. Rev. Lett. **44**, 1586 (1980).
[11] B.G. Klappauf, W.H. Oskay, D.A. Steck, and M.G. Raizen, Phys. Rev. Lett. **81**, 4044 (1998).
[12] T. Jonckheere, M.R. Isherwood, and T.S. Monteiro, Phys. Rev. Lett. **91**, 253003 (2003).
[13] P.H. Jones, M. Goonasekera, H.E. Saunders-Singer, and D. Meacher, quant-phys/0309149.
[14] M. Stocklin, G. Hur, and T.S. Monteiro, physics/0408088.

PHYSICAL REVIEW A 72, 013403 (2005)

Chaotic quantum ratchets and filters with cold atoms in optical lattices: Analysis using Floquet states

G. Hur, C. E. Creffield, P. H. Jones, and T. S. Monteiro
Department of Physics and Astronomy, University College London, Gower Street, London WC1E 6BT, United Kingdom
(Received 11 November 2004; published 6 July 2005)

Recently, cesium atoms in optical lattices subjected to cycles of unequally spaced pulses have been found to show interesting behavior: they represent an experimental demonstration of a Hamiltonian ratchet mechanism, and they show strong variability of the dynamical localization lengths as a function of initial momentum. The behavior differs qualitatively from corresponding atomic systems pulsed with equal periods, which are a textbook implementation of a well-studied quantum chaos paradigm, the quantum δ-kicked rotor (δ-QKR). We investigate here the properties of the corresponding eigenstates (Floquet states) in the parameter regime of the recent experiments and compare them with those of the eigenstates of the δ-QKR at similar kicking strengths. We show that by studying the properties of the Floquet states we can shed light on the form of the observed ratchet current, as well as variations in the dynamical localization length.

DOI: 10.1103/PhysRevA.72.013403 PACS number(s): 32.80.Pj, 05.45.Mt, 05.60.−k

I. INTRODUCTION

Periodically kicked quantum systems, such as the δ-kicked rotor (δ-KR), have long played a central role in studies of quantum chaos and the correspondence between quantum behavior and the underlying classical dynamics [1,2]. Advances in the manipulation of cold atoms have permitted the experimental realization of these systems in pulsed optical lattices [3]. Experiments with sodium and cesium atoms have demonstrated the phenomenon of "dynamical localization" (DL)—the quantum suppression of classical chaotic diffusion—and established the suitability of these systems as an arena for the study of effects arising from quantum chaos.

When treating conservative quantum systems it is frequently useful to study the system's energy eigenstates, and for periodically driven systems the appropriate generalization of these states is given by the Floquet states. This approach has provided extensive insight into the properties of the standard quantum KR (QKR), and has shown, for example, that DL arises directly from the exponential localization of the system's Floquet states [2]. Observed momentum oscillations associated with chaos-assisted tunneling, in experiments using periodically driven cold atoms [4] and Bose-Einstein condensates [5] have also been analyzed with Floquet theory; it was found that the oscillation period is determined by the splittings of the Floquet phases of a pair of symmetry-related eigenstates. The statistics of the QKR Floquet quasienergy spectrum have been studied extensively (see, e.g., [6]) and compared with the predictions of random matrix theory. Notably, though, the δ-QKR has Poissonian statistics (which are typically associated with integrable dynamics) even for very large values of K, where the dynamics is fully chaotic. This has been shown to be a further consequence of DL [6].

However, a series of recent theoretical [7,8] and experimental [9–11] studies of cold atom systems subjected to repeating cycles of unequally spaced kicks revealed dynamics rather different from that found in the corresponding standard QKR systems. Two types of unequally δ-kicked systems were investigated. The first [8,9] consists of a δ-KR with small perturbations made to the kick period. We term it the perturbed-period KR. In the second system [11], the system is periodically subjected to *pairs* of closely spaced kicks. This is referred to as the double δ-KR or 2δ-KR.

In a theoretical study, the perturbed-period KR was found to yield a ratchet current even in the chaotic regime [7,8]. This was unexpected in a chaotic Hamiltonian system, since to date only mixed phase-space ratchet mechanisms had been investigated [12,13]. A simple definition of a ratchet is a spatially periodic device which produces a current without net bias (i.e., the time- and space-averaged forces are zero). Most of the extensive ratchet literature deals with dissipative or Brownian ratchets [14] and comparatively little theoretical work has been undertaken on Hamiltonian ratchets, which are dissipation and noise-free.

In Refs. [9,10] a momentum distribution with a nonzero average (constant in time) was obtained experimentally from an atomic cloud with initial zero average momentum. We are unaware of any other experimental studies of Hamiltonian quantum ratchets: all implementations to date have been of dissipative or Brownian ratchets. Hence the results from [10] and also reproduced here represent the only experimental realization of a Hamiltonian quantum ratchet, whether chaotic or mixed phase space, to our knowledge. In Ref. [8] it was also proposed that the chaotic diffusive properties of the perturbed-period KR could be exploited to filter cold atoms according to their momenta, by controlling the dynamical localization.

For the second system, the 2δ-KR, a theoretical and experimental study [11] revealed that the diffusion is dominated by long-ranged correlations which control escape from well-defined momentum trapping regions. This combination of strong chaotic diffusion and long-ranged correlations is unusual, since strong chaos is generally associated with rapidly decaying correlations.

It is clear that Floquet theory is central to the analysis of chaotic, time-periodic quantum systems. The need to under-

stand further the chaotic Hamiltonian ratchet as well as the 2δ-KR motivated this study of the Floquet states of these systems. The paper is organized as follows. In the next section we review the well-known δ-KR, then introduce the perturbed δ-KR and the double δ-KR systems. In Sec. III we give a brief review of the Floquet approach. In Sec. IV we compare the results with recently obtained experiments on these systems. Finally in Sec. V we give our conclusions.

II. INTRODUCTION TO δ-KICKED SYSTEMS

The Hamiltonian for the usual δ-KR can be written as

$$H=\frac{p^2}{2}+K\sin x\sum_n \delta(t-nT) \tag{2.1}$$

where K is the kick strength and T is the kick period. It is usual, in both experimental and theoretical studies, to work in a system of rescaled units, where for instance, time is measured in units of T (see, for example, [10,16] for details). Without loss of generality, here we take $T=1$.

Consider the evolution of an ensemble of particles with a Gaussian momentum distribution centered on p_0, $N(p)=\exp[-(p-p_0)^2/\Delta p^2]$. The classical dynamics depends only on the parameter K, and for values larger than $K\simeq 1$, the chaotic diffusion is not bounded by classical barriers. In this regime the ensemble will diffuse in momentum space, its average energy growing linearly with time as $\langle p^2\rangle=Dt$, where, to lowest order, the diffusion rate is given by $D_0=K^2/2$. The distribution will thus remain Gaussian, although its width will increase with time as $\Delta p(t)=\sqrt{Dt}$.

In contrast, the quantum system only follows this behavior up to a time scale $t^*\simeq D/\hbar^2$ [15], after which diffusion in momentum space is suppressed—dynamical localization. Such a system will asymptotically evolve toward a characteristic exponential momentum distribution, $N(p)\sim\exp[-|p-p_0|/\Delta p_Q]$, with constant width $\Delta p_Q\sim\sqrt{Dt^*}\sim D/\hbar$, which thus acts as an experimental fingerprint for DL [3]. As DL is a wave-coherent effect, the quantum system must preserve coherence over at least the time scale t^* for this effect to be observable. Indeed, it has been verified experimentally [16] that the DL profile does not survive the presence of noise or dissipation, and that with decoherence a more Gaussian profile for $N(p)$ is produced.

In both classical and quantum cases the behavior of the standard δ-KR is essentially independent of p_0 since, even for modest values of K, the effects of small fluctuations in the structure of phase-space are on negligible scales relative to Δp_Q. Even if there are small stable islands, they are of size $\Delta p\sim 1$ so have little effect on the general form of $N(p)$, since typically $\Delta p_Q\gg 1$.

The classical dynamics of the δ-KR is obtained by iterating the well-known standard map. For the perturbed-period and double δ-kicked systems, on the other hand, the dynamics is given by a two-kick map:

$$x_j=x_{j-1}+p_jT_1,$$

$$p_{j+1}=p_j-V'(x_j),$$

$$x_{j+1}=x_j+p_{j+1}T_2,$$

$$p_{j+2}=p_{j+1}-V'(x_{j+1}).$$

For the perturbed-period KR, the lengths of the two kicking periods are $T_1=1+\epsilon$ and $T_2=1-\epsilon$, where $\epsilon\ll 1$. The perturbation thus consists of slightly altering the kicking period about its mean. For the double δ-KR we take $T_1=2-\epsilon$, $T_2=\epsilon$, although we shall also show the effect of interchanging the two kick periods. It should be noted that these systems are *time periodic*, with period $T_{\rm tot}=T_1+T_2$, and are thus quite distinct from the recent interesting study of two independent kicking sequences, which can be nonperiodic and hence nonlocalizing [17].

As in the standard map, we consider a sinusoidal potential. However, to obtain a ratchet current in the case of the perturbed-period KR, we need to break the spatiotemporal symmetries, and so we add an additional "rocking" linear potential of strength A. In this case the form of the potential is

$$V(x)=[K\cos x+Ax(-1)^j], \tag{2.2}$$

where j is the kick number. In experimental implementations of this system, the rocking linear term was obtained by means of an accelerated lattice [9]. Clearly, setting $T_1=T_2=1$ and $A=0$, we recover the standard map.

We first consider in general terms how the introduction of the second time scale ϵ modifies the classical behavior of the standard map. If we neglect all correlations, the standard map has a constant momentum diffusion rate $D_0\simeq K^2/2$—this is what one would expect if the momenta at consecutive kicks are uncorrelated and so evolve as a random walk. However, unless K is exceedingly large, the time evolution of the standard map will contain some short-range (two- and three-kick) correlations. Including these corrections yields a modified diffusion constant $D=(K^2/2)\{1-2J_2(K)-[J_1(K)]^2\cdots\}$. Of particular interest is the $J_2(K)K^2$ term, representing correlations $\langle V'(x_j)V'(x_{j+2})\rangle$ between nearest-but-one kicks (the two-kick correlation).

For the modified systems it is also possible to obtain the important correlations analytically [8,11]. For instance, for the perturbed-period system the corrected diffusion is given by

$$D\simeq\frac{K^2}{2}\{1-2J_2(K)\cos(2p_0\epsilon-A)-[J_1(K)]^2\cdots\}. \tag{2.3}$$

We see that the modified two-kick correlation now *oscillates* as a function of the initial momentum p_0. This effect is clearly most significant for values of K such that $2J_2(K)\sim 1$.

The key point is that perturbing the kick spacings T by a small amount can result in large scale (relative to $\Delta p_Q\sim D/\hbar$) variations in the classical momentum diffusion, and that these are present even in fully chaotic regimes (we take this to mean the absence of visible stable structures on the Poincaré surface of section). For the analysis of experiments, one must now consider a *local* diffusion rate $D(p_0)$, which

depends on the initial relative momentum between the atoms and the optical lattice.

In [9], the perturbed-period system was implemented experimentally with a cloud of cesium atoms for the case $A=0$. It was verified that the energy absorbed by the cloud after dynamical localization $\langle (p-p_0)^2\rangle \propto \cos(2p_0\epsilon)$ as expected. However, $A=0$ corresponds to a symmetric potential. The case $A=\pi/2$ in the perturbed-period system is particularly interesting since then the momentum diffusion is asymmetric about $p_0=0$. This implies that atoms with positive momenta will absorb kinetic energy at different rates from those with momenta of the same magnitude but moving in the opposite direction. This asymmetric momentum diffusion represents a type of fully chaotic *momentum* ratchet: in other words, roughly equal numbers of particles will diffuse to the left or to the right, but those diffusing to the right, on average, move faster.

In a further experimental study of the perturbed-period KR [10], the rocking potential was implemented by means of an accelerated lattice. It was found that an atomic cloud prepared initially with a Gaussian momentum distribution centered on $p_0=0$ evolved into a distribution with nonzero, but constant, $\langle p\rangle$ which persisted even beyond the break time t^*, as expected from the theory [7]. This type of chaotic directed motion was first identified in a slightly different system: a kicked asymmetric double-well potential [7]. However, the latter potential gives rise to a rather more complicated diffusive behavior, and also has proved much harder to implement experimentally. For these reasons here we do not consider the case of the asymmetric double-well ratchet, but note that our Floquet analysis of the perturbed-period KR can be carried over to the system investigated in [7].

The second system we consider explicitly in this work, the double δ-KR, has diffusive behavior which is qualitatively different to both the standard map and perturbed-period KRs. While for these other kicked systems we can analyze the diffusion as an uncorrelated term, $K^2/2$, corrected by short-ranged correlations (typically only two- or three-kick correlations for $K\simeq 3$), for the double δ-KR, we find that the diffusion at long times is dominated by families [11] of long-ranged "global" correlations ("global" in the sense that they correlate all kicks up to the time under consideration). At short times, the diffusion is dominated by a one-kick correlation not present in other kick systems. At longer times, the global diffusion terms, though weak, accumulate and eventually become dominant.

The method of correlations provides a generic and accurate way of interpreting experimental data for this system [11]. There is also a simple physical picture. For particles subjected to kicks of form $K\sin x$, consecutive kicks will be out of phase and will hence cancel if $p_0\epsilon \simeq (2n+1)\pi$ where $n=0,1,2\ldots$. In other words, an impulse $V'(x_j)=K\sin x_j$ will be immediately followed by another which cancels it, since $V'(x_{j+1})=K\sin x_{j+1}\simeq K\sin(\pi+x_j)$. This cancellation means that particles become trapped at these momenta. In contrast, particles for which $p_0\epsilon \simeq 2n\pi$ will experience enhanced diffusion.

It was shown in [11] that the types of global families of correlations described there control the escape from, and through, these "trapping regions." An unexpected feature of the classical calculations (and also seen in experiment) was the observation that particles initially prepared in the trapping regions will eventually gain more energy than those initially prepared in regions of enhanced diffusion, after a time scale $t \gg 1/(K\epsilon)^2$ [11].

III. QUANTUM DYNAMICS AND FLOQUET STATES

If a Hamiltonian has a T-periodic time dependence, $H(t+nT)=H(t)$, then the Floquet theorem implies that solutions to the time-dependent Schrödinger equation can be written in the form

$$\psi(t)=\exp(-i\epsilon t/\hbar)\phi(t) \tag{3.1}$$

where $\phi(t)$ is a T-periodic function called a Floquet state, and ϵ is a quantity with dimensions of energy, termed a quasienergy. This type of relation is familiar in the context of solid-state physics, where a Hamiltonian's invariance under discrete shifts of *spatial* position (typically arising from a lattice structure) allow solutions to be written analogously in terms of Bloch states and quasimomenta. The Floquet states provide a complete basis, and thus the time-evolution of a general quantum state under periodic driving can be expressed as

$$\Psi(t)=\sum_n c_n \exp(-i\epsilon_n t/\hbar)\phi_n(t), \tag{3.2}$$

where $\{c_n\}$ are *time-independent* expansion coefficients. It is clear from this expression that the Floquet states and quasienergies play a similar role for periodically driven systems to that of energy eigenstates and eigenvalues in the time-independent case.

The time-evolution operator $U(t_2,t_1)$ may be used to evolve a quantum state from time $t=t_1$ to time $t=t_2$. For a time-periodic system, the single-period propagator $U(T,0)$ allows a quantum system to be evolved "stroboscopically" at intervals separated by the period T with great efficiency, by defining the quantum map $\Psi(nT)=[U(T,0)]^n\Psi(0)$. In terms of Floquet states, it is straightforward to show that the time-evolution operator is given by

$$U(t_2,t_1)=\mathcal{T}\exp\left(-\frac{i}{\hbar}\int_{t_1}^{t_2} H(t')dt'\right) \tag{3.3}$$

$$=\sum_n e^{-i\epsilon_n t/\hbar}|\phi_n(t_2)\rangle\langle\phi_n(t_1)|, \tag{3.4}$$

where $\mathcal{T}$ is the time-ordering operator, and thus it can be seen that the quasienergies and Floquet states can be conveniently obtained by simply diagonalizing the one-period propagator. The eigenvectors of this operator are the Floquet states, while its eigenvalues are related to the quasienergies via $\lambda_n=\exp(-i\epsilon_n T/\hbar)$.

Obtaining an explicit form for this propagator is normally a complicated procedure, as in general the driving field does not commute with the static Hamiltonian. For the case of δ kicking, however, the problem is simplified considerably

which allows an analytic form for the propagator to be written. For the QKR [Eq. (2.1)] the propagator is given by

$$U(T,0)=\exp(-iT\hat{p}^2/2\hbar)\exp[-i(K/\hbar)\sin\hat{x}]. \quad (3.5)$$

Since the kicking potential is invariant under spatial translations of 2π, Bloch's theorem permits the eigenvalues of $\hat{p}$ to be decomposed into the form $p_m=(m+q)\hbar$, where m is an integer and q is a fraction lying in the interval $[-0.5,0.5)$, termed the "quasimomentum." A true kicked rotor system, as distinct from a kicked particle, would be obtained by setting the quasimomentum $q=0$. Using this basis, the matrix elements $\langle m+q|U(T,0)|n+q'\rangle$ of the propagator can easily be shown to be

$$U_{m,n}(T,0)=\exp[-iT(m+q)^2/2\hbar]J_{m-n}(K/\hbar)\delta(q-q'), \quad (3.6)$$

where J_n is the nth Bessel function of the first kind. For practical purposes it is useful to note that $|J_{m-n}(x)|$ decreases extremely rapidly with increasing $|m-n|$, thus giving U an effectively banded structure.

The one-kick propagators $U(T_1,0)$ and $U(T_2,0)$, where T_1 and T_2 are the two kick periods, take a slightly different form from Eq. (3.6) if we include a ratchet potential (i.e., $A\neq 0$). Nevertheless in all cases the two-kick (full-period) propagator can be expressed as the product $U(T_{tot},0)=U(T_1+T_2,T_1)U(T_1,0)$. Note that for $A\neq 0$, however, although the single-kick propagators do not conserve quasimomentum, their product does. As a consequence, the evolution of an ensemble of noninteracting particles, which can be modeled by the evolution of a superposition of states with different quasimomenta, represents a computationally efficient procedure: since $U(T_{tot},0)$ is block diagonal in q, we can consider each quasimomentum component separately and diagonalize the smaller submatrices.

The matrix representation for the full-period propagator, in its most general form, has elements

$$U_{l,n}(T,0)=i^{n-l}e^{-iT_1(l+q)^2\hbar}\sum_j e^{-iT_2(j+qa)^2\hbar} \times J_{l-j+ka}\left(\frac{K}{\hbar}\right)J_{j-n-ka}\left(\frac{K}{\hbar}\right), \quad (3.7)$$

where $ka=\mathrm{int}(A)$ and $qa=A-ka$. To obtain the form appropriate for the 2δ-KR, it is simply necessary to set $A=0$, $T_1=2-\epsilon$, and $T_2=\epsilon$.

Having obtained the Floquet states by diagonalizing the full-period propagator, it is useful to analyze their structure, particularly their spread in momentum space. We do this by evaluating a localization length, L of each Floquet state at $T=0$. We note that in this case we cannot assume that the Floquet states have the usual exponential momentum distribution $N(p)\sim\exp(-|p-p_0|/L)$, of the usual δ-KR. Hence we take L to be simply the root mean square deviation from the mean, $L=\sqrt{\overline{p^2}_n-\bar{p}_n^2}$. In this expression $\bar{p}_n$ is the mean momentum of the nth Floquet state at $t=0$, $\bar{p}_n=\langle\phi_n(0)|\hat{p}|\phi_n(0)\rangle$, and $\overline{p^2}_n=\langle\phi_n(0)|\hat{p}^2|\phi_n(0)\rangle$. If the Floquet states do not have a strong time dependence, such as for the standard or even the perturbed-period KR, this is adequate to quantify the degree of spreading in momentum space. We shall see, however, that for the case of the double δ-KR it is not sufficient to measure the localization at just a single time, due to the extremely strong time dependence of the Floquet states.

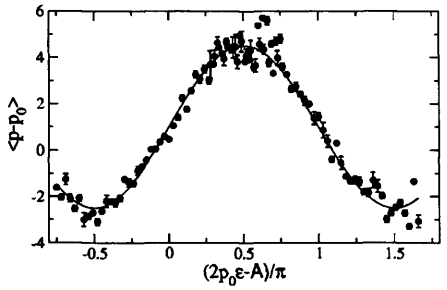

FIG. 1. Experimental values of the ratchet current $I=\langle p-p_0\rangle$, for the perturbed-period KR, obtained with cold cesium atoms in a pulsed optical lattice for $K=2.6$, $\epsilon=1/16$. The solid line is a best fit to the data, showing that the current oscillates sinusoidally as $I\propto\sin(2p_0\epsilon-A)$.

IV. RESULTS

A. Perturbed-period KR: Experimental realization of a chaotic ratchet

Figure 1 shows a plot of the experimental ratchet current obtained in [10] using distributions of cold cesium atoms with $p_0=0$, in an optical lattice pulsed with unequal periods. The momentum distribution is essentially unchanged after about 60 kicks; the plotted values correspond to about $T=200$ kicks, hence well after dynamical localization. Full details are given in [9,10], but by employing an accelerated lattice, the experiment was able to simulate an effective rocking potential with a given value of A. The current (the first moment of each localized momentum distribution $I=\langle p-p_0\rangle$) was then calculated, and is plotted as a function of A in Fig. 1.

Figure 1 shows that the ratchet current oscillates sinusoidally, i.e., $I\propto\sin(2p_0\epsilon-A)$. This can be qualitatively understood from the form of the classical two-kick momentum-diffusion correction [Eq. (2.3)] $C_2=-K^2J_2(K)\cos(2p_0\epsilon-A)$. If we set $p_0=0$, as in the experiment, then for a very small momentum displacement δp, the differential absorption of energy for particles moving to the left $\delta p<0$ or right $\delta p>0$ is proportional to the gradient $\partial C_2/\partial p_0\propto K^2\sin(2p_0\epsilon-A)$. An analytical form for the classical current was derived previously [8]. An asymptotic (small-ϵ) approximation for the ratchet current is given by $I\simeq[J_2(K)/\epsilon]\sin(2p_0\epsilon-A)$, implying the maximal classical current is $I_{max}\sim J_2(K)/\epsilon$.

The results in Fig. 1 correspond to $K=2.6$, $\epsilon=1/16$, and $\hbar=1$ (note that in rescaled units $\hbar=8\omega_R T$, where ω_R is the Rabi frequency). This effective value of Planck's constant may be varied: in the experiments, the range $\hbar\simeq 1/4\rightarrow 1$ was investigated. For these values of K and ϵ, we estimate $I_{max}\sim J_2(K)/\epsilon\simeq 8$, about twice the observed value. This is

not unreasonable as $\epsilon=1/16$ is not so small and we neglect higher-order corrections to the classical current. The experiments in [10] indeed indicate that halving ϵ almost doubles the maximal current. Note that changing the sign of ϵ implies a current reversal.

At this stage it may be unclear to the reader what the significance of altering the sign of ϵ in the experiment might be, since after all, the rocking potential involves alternating impulses $-V'(x)=K\sin x\pm A$. In fact the distinction (as may be ascertained when calculating correlations) is between the case where an impulse $-V'(x)=K\sin x+A$ follows free evolution for the longer time interval $T_1=1+\epsilon$ [and the impulse $-V'(x)=K\sin x-A$ follows free evolution for the shorter time interval $T_2=1-\epsilon$] and the *separate* experimental case where an impulse $-V'(x)=K\sin x-A$ follows evolution for a time interval $T_1=1+\epsilon$ and so forth (which corresponds to an current of identical magnitude but of opposite sign).

Of course, it is clear that a nonzero and persistent constant ratchet current is also obtained classically. It was found in [7] that asymmetric diffusion accumulates only on a time scale $t_r\sim 1/(K\epsilon)^2$ (termed the "ratchet time" in [7]). Note that $I_{max}\sim J_2(K)/\epsilon$ implies that $I_{max}\to\infty$ as $\epsilon\to 0$, but in that case $t_r\sim\infty$ and so the final value of the current is never reached. For the (unbounded) chaotic system studied here, the acquired momentum asymmetry is never lost. For a bounded ("compact phase-space") system, such asymmetries would vanish on a long time scale, since the distribution of a fully chaotic system would eventually become uniform. For this reason, until recently, it was argued that a fully chaotic system could not generate directed motion. So, although as shown in [7], the fully chaotic classical system can keep a constant current for long times, practical implementation is ultimately less interesting since the average kinetic energy of the ensemble grows linearly with time and without limit. Hence, this type of chaotic ratchet is of most interest as a *quantum* rather than a *classical* ratchet since in the quantum case DL halts the diffusion and "freezes in" the asymmetry, without the need for classical barriers like tori.

In Fig. 2 we reproduce two experimental momentum distributions for $K\simeq 3$ obtained with cesium atoms in Ref. [10], for $A=\pm\pi/2$. We clearly see that the origin of the nonzero current is the asymmetric momentum distribution. As expected, Fig. 2 shows that changing the sign of A reverses the asymmetry and produces a current reversal, in an analogous fashion to the way that altering the sign of ϵ also reverses the current.

Note that the experimental range of $K\simeq 2.6$–3.4 does correspond to a classical surface of section with some islands. However, we note that classical quantities such as the average energy are very accurately given by diffusion rates (with two- and three-kick corrections). The essential mechanism is asymmetric chaotic diffusion: similar behavior was found at larger K in [7] in regimes where there are no visible classical islands (but for which experiments are not available); hence, in the analysis of this type of ratchet, the presence (or otherwise) of small stable islands is immaterial. What is important, though, is that since the asymmetric diffusion term is $2J_2(K)\cos(2p_0\epsilon-A)$, we need $J_2(K)\neq 0$. Thus the much studied (for the standard map) parameter value $K=5$ does *not* produce asymmetry, since $J_2(5)\simeq 0$. Values of $K\simeq 2.5$–3.5, $\hbar=1/4$–1, on the other hand, turned out to be experimentally convenient and produced the strongest asymmetries.

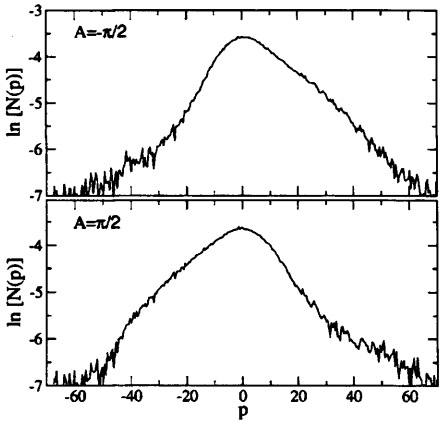

FIG. 2. Experimental momentum distributions $N(p)$ for the perturbed-period KR obtained with cold cesium atoms in a pulsed optical lattice for $K\simeq 3$, $\epsilon=1/16$. The distributions have localized, and hence remain essentially constant with time. The results show clearly that the origin of the net nonzero value of $\langle p\rangle$ obtained at long times is in the asymmetry of the DL profiles. As expected, the asymmetry is reversed by changing the sign of A, the amplitude of the rocking potential.

B. Perturbed-period KR: Floquet states

We now examine the form of the underlying Floquet states. In Fig. 3 we compare the localization lengths for the standard QKR, with those of the perturbed-period KR for $K=3.4$, $\epsilon=0.01$. The difference is quite striking; while the standard QKR eigenstates are quite uniform across all regions of phase space, the perturbed-period localization lengths oscillate sinusoidally with $\bar{p}$, with a period of π/ϵ. Introducing the additional rocking potential with the accelerated lattice ($A=-\pi/2$) clearly leads to a $\pi/2$ shift in the oscillations. Inspecting Fig. 3(c) for $\bar{p}\simeq 0$, we see that for positive momenta the localization lengths are increasing, while for negative momenta, the localization lengths decrease. Note the nearly regular row of states for the standard QKR case with $L\simeq 1$. These correspond to states localized on a series of stable islands separated by 2π, due to the momentum periodicity of phase-space in that case.

We have chosen a parameter range for which $L\ll\pi/\epsilon$: that is, the localization length of each state is much smaller than the oscillation in $\bar{p}$. Hence individual Floquet states really do sample "local" diffusion rates. We found that if we move toward a regime where $L\sim\pi/\epsilon$, the conclusions remain valid, but the amplitude of the oscillations is considerably damped. Similarly, if the sign of $J_2(K)$ changes, so does the sign of the sinusoidal oscillation.

We now consider the shape of the Floquet states in detail. In Fig. 4 we show the momentum distributions $N(p)$

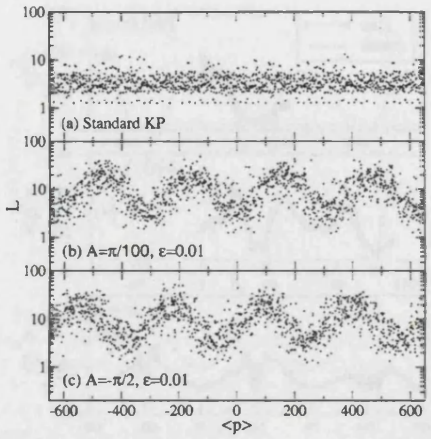

FIG. 3. The graph shows the localization lengths L of Floquet states as a function of average momentum $\bar{p}$ (i.e., $\langle p \rangle$) for $K=3.4$, $\hbar=1$. Results are shown (a) for the standard QKR case, i.e., $A=\pi/100$ (a small but nonzero A was used to break spatial symmetry), $\epsilon=0$, (b) for $\epsilon=0.01$, $A=\pi/100$, and (c) for $\epsilon=0.01$, $A=-\pi/2$. The graph shows that for the standard kicked rotor the L are distributed within a narrow range in comparison with other two below. For the rocking case, L oscillates with $\bar{p}$ as expected from the two-kick correction $2J_2(K)\cos(2p_0\epsilon-A)$; the oscillations of the two lower graphs are shifted relative to each other by a phase $\pi/2$. The density of eigenstates corresponding to average momentum range is roughly the same in all three cases.

$=|\phi_n(p)|^2$ for Floquet states of the standard QKR. The distributions (with $N(p)$ on a logarithmic scale) all show the well-known triangular form [2]—the hall-mark of dynamical localization. It may be clearly seen that the localization lengths vary little from state to state.

In Fig. 5, by contrast, the localization lengths of the Floquet states of the perturbed-period δ-KR display a strong dependence on the mean momentum of the states. In addition, the figure shows that states localized close to $p=0$ are markedly asymmetric. The states are considerably extended toward positive momentum, but are strongly localized to-

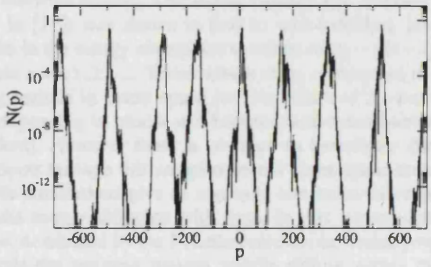

FIG. 4. Floquet states for the standard QKR, for $K=3.4$, $\hbar=1$. As expected, all the states are exponentially localized, giving the characteristic triangular shape of $N(p)$ when plotted on a logarithmic scale. They all have approximately similar localization lengths.

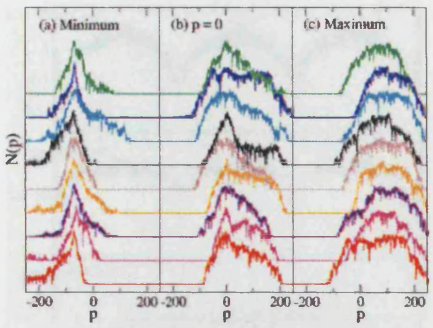

FIG. 5. (Color online) Typical form of Floquet states for the perturbed-period KR, $K=3.4$, $\epsilon=0.01$, $A=-\pi/2$ and $\hbar=1$. Here we plot $N(p)=|\phi_n(p)|^2$ on a logarithmic scale as a function of p. (a) States with $p=-78$. This corresponds to a minimum of the two-kick correction (2.3)—$\cos(2p_0\epsilon+\pi/2)$. The states are narrow, but in general roughly symmetric. (b) States with $p=0$. The typical state here is asymmetric. (c) States with $p=78$. This corresponds to a maximum of the two-kick correction. States here are generally symmetrical, but broad and flat-topped.

wards negative p. This behavior neatly accounts for the form of the experimental momentum distribution shown in Fig. 2, which for $A=-\pi/2$ were also more extended toward positive p. The states localized near $p\simeq-\pi/4\epsilon$ and $\pi/4\epsilon$ correspond to, respectively, minima and maxima of the classical diffusion. They are roughly symmetrical (typically) but vary by up to a factor of ~ 40 in L. In Ref. [8] it was proposed that the observed variation in the energy absorption rates between atoms prepared with an initial drift momentum $p_0=-\pi/4\epsilon$ (which absorb very little energy) and those with $p_0=\pi/4\epsilon$ might be exploited to filter traffic of atoms through an optical lattice. The form of the underlying Floquet states explains this differential rate of energy absorption.

Subsequently, it was found experimentally that the double δ-KR in fact shows much more pronounced differential absorption rates, without requiring the application of a rocking field A. We next report a study of this system.

C. Double δ-KR: Experimental realization

A study of the experimental and classical behavior of the double δ-KR was carried out in [11]. The classical dynamics is very different to that of the perturbed-period KR. At very short times, the chaotic diffusion comprises an uncorrelated diffusion term $K^2/2$ and one dominant one-kick correction. It was found in [11] that one can approximate the growth in the mean energy with time t, by the simple expression $\langle p^2 \rangle \simeq K^2 t[1+\cos p_0\epsilon]$. In Fig. 6(a) we show experimental results for cesium atoms which localized in this regime. The experiment measured the energy of a series of clouds of $\sim 10^6$ atoms moving through the pulsed optical lattice with varying average drift momenta p_0. For Fig. 6(a), the simple expression given above gives an excellent fit to the experiment, if we take $t\sim t^*$, where t^* is the break time. This regime corresponds to $t^*\ll 1/(K\epsilon)^2$.

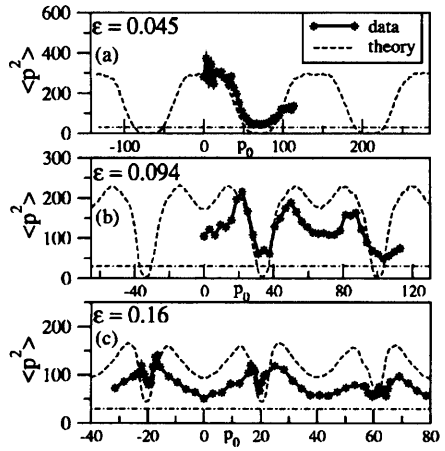

FIG. 6. Experimental results for double δ-KR realization with cesium atoms (see [11] for details). Each data point (star) shows the energy absorbed (after 100 kicks, $K=3.3$, $\hbar=1$) by a cloud of atoms with average momentum $p=p_0$ (relative to the optical lattice) at initial time $t=0$. With increasing ϵ, we see the minima (maxima) in the energy flip into maxima (minima) as a long-ranged family of classical correlations gradually overtakes the one-kick classical correlation. The dashed lines represent a classical simulation using 100 000 particles, all with momenta p_0 at $t=0$, and K within the range $3.3\pm10\%$. (a) $t^* \ll t_1 \simeq 1/(K\epsilon)^2$. Regime where a one-kick correlation is the dominant correction to the classical diffusion. Here, atoms prepared near the trapping regions $(p_0\epsilon \sim (2n+1)\pi)$ remain trapped. Results follow closely the formula $\langle p^2\rangle \simeq K^2 t(1+\cos p_0\epsilon)$. (b) $t^* \sim 1/(K\epsilon)^2$. Regime showing the inverted peaks of the Poisson correlation terms analyzed in [11], which determine the momentum trapping very close to the resonant condition $(p_0\epsilon = (2n+1)\pi)$. (c) $t^* > 1/(K\epsilon)^2$. Regime dominated by correlation family C_{G1}, but sharp inverted peaks due to the Poisson correlations are still visible.

However, a more detailed study of the classical correlations showed that for later times, a new type of correction appeared. Families of long-ranged, or "global," correlations which coupled *all* kicks appeared. These corrections are individually very weak, but accumulate to eventually dominate the diffusive process. One family (termed the "Poisson family" in [11]) was shown to lead to well-localized, inverted peaks in the energy absorption at values of $p_0 \simeq (2n+1)\pi/\epsilon$, where $n=0,1,2,\ldots$. These values of p_0 correspond to trapping regions in phase space (at low values of K, structures corresponding to islands and broken phase-space barriers are evident). However there is no need to investigate detailed transport through this complex mixed phase-space structure, as the correlations give us a generic and quantitative handle on the energy diffusion with time. In this intermediate regime, dominated by the Poisson correlations, atoms prepared outside the trapping regions rapidly diffuse across the regions between them. Particles prepared in the trapping regions remain there. This regime occurs for $t^* \sim 1/(K\epsilon)^2$ and corresponds approximately to the experimental results shown in Fig. 6.

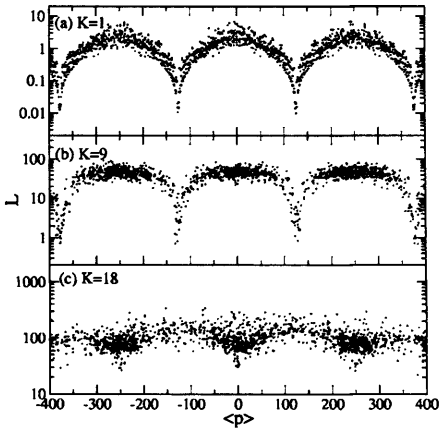

FIG. 7. Localization lengths of typical states for the double δ-KR ($\epsilon=0.025$, $\hbar=0.5$) corresponding to the three classical diffusion regimes investigated in the experiments in [11].

Finally, at the longest time scales, there is the C_{G1} correction investigated in [11], which is a long-ranged global-correlation family. C_{G1} results in an oscillation of the form $-\cos p_0\epsilon$ and becomes dominant at the longest timescales. The oscillation is of the same period as the one-kick correlation, but is of opposite sign. This means that at the longest time scales, the minima in energy absorption shown in Fig. 6(a) become maxima in energy absorption; and vice versa: the maxima become minima. Figure 6(c) shows experiments tending toward this regime. The inverted peaks of the Poisson family are still in evidence, but a $-\cos p_0\epsilon$ oscillation is clearly superposed. This is a somewhat counterintuitive result since it implies that atoms initially prepared in the momentum trapping regions are the ones which at long times, for $t^* \gg 1/(K\epsilon)^2$, will absorb the most energy (there are no further reversals of this behavior at even longer times).

D. Double δ-KR: Floquet states

The classical analysis thus reveals that there are three distinct classical diffusive regimes occurring at three time scales. We can expect that the corresponding *quantum* behavior will depend on which regime is dominant when dynamical localization arrests the quantum momentum diffusion. To investigate this, we now investigate how the form of the Floquet states varies in these different regimes.

In Fig. 7(a) we show the localization lengths of the Floquet states for a weak kicking strength. It can clearly be seen that the localization varies periodically as a function of momentum, staying within the range $1 \leq L \leq 10$ for the majority of points, with the exception of a series of sharp cusplike features at which the localization dramatically falls. The location of these cusps exactly corresponds to the "trapping momenta" $p\epsilon=(2n+1)\pi$, predicted from classical arguments. The Floquet states centered in the trapping regions have widths of $L \simeq 0.01$, much narrower than states localized on stable islands, which are also visible in this figure as regular

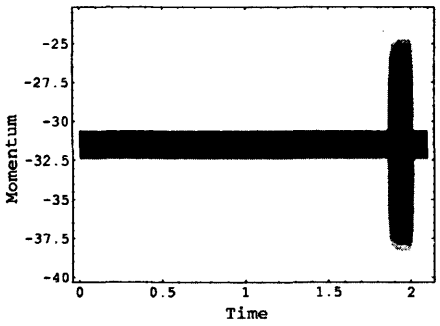

FIG. 8. Time evolution of a localized Floquet state in momentum space, $N(p,t)$, for physical parameters $K=2$, $\epsilon=0.1$, and $\hbar=0.5$. Initially the Floquet state is sharply peaked at $p=-10\pi$, in the center of a trapping region. The first kick at $t=1.9$ causes the state to spread across a much broader range of momentum, until the second kick at $T=2$ restores the localized state.

strings of points at $L\sim 1$. At the experimental values of $K\simeq 3$ and $\epsilon=0.01$ a similar behavior is produced, with the broadest Floquet states having localization lengths of $L\simeq 60$, while the narrowest have widths of $L\simeq 0.03$, over one thousand times narrower.

The Floquet states at the tips of the cusps have such low localization lengths that they are effectively pure plane-wave states (this can be further corroborated by evaluating the inverse participation ratio for these states, which indeed takes a value of almost unity). It is thus unsurprising that the presence of these states corresponds to the classical trapping effect, as a quantum system prepared in such a state will have a vanishingly small overlap with any other state and so will remain frozen (or trapped) in its initial state. It is important to note, however, that this quantum trapping effect depends critically on the *order* of the two kick periods—that is, whether the system is driven with a short-long kick sequence or the inverse long-short ordering.

This may appear surprising at first, since the Floquet states are periodic, with the same period T_{tot} as the driving, and this period is not altered by interchanging the order of the kicks. Although it is frequently neglected, however, it is important to recall that the Floquet states do have an explicit time-dependence within each period, and this *is* able to produce substantially different behavior [18] when the phase of the driving field is altered. To illustrate this, we show in Fig. 8 the time evolution of one of the localized Floquet states, which experiences δ kicks at times $t=T_1=1.90$ and $t=T_{tot}=2$. As can be seen, the state has only a trivial time evolution during the first time interval $(0\leq t<T_1)$, since it is almost a plane wave and is thus approximately an eigenstate of the free Hamiltonian. The first kick at T_1 causes the wave packet to spread considerably in momentum space, before the second kick restores this broadened state to its original narrow form. Thus in this brief window of time between the two kicks, even the most localized Floquet states have a considerable spread in momentum. As a consequence, if the phase of the kicking field is shifted so that the system experiences the short-long kick sequence, none of the Floquet states are

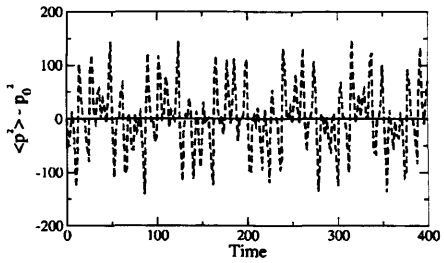

FIG. 9. Time evolution of the energy of the double δ-KR, for the same physical parameters as in Fig. 7(a). The solid line shows the evolution of the system under the long-short kicking sequence, and shows few features. The dotted line shows the result of the short-long sequence, and exhibits a complicated quasiperiodic behavior.

sharply localized in momentum at $t=0$. We show in Fig. 9 the time evolution of the system's kinetic energy when it is prepared in a momentum eigenstate in a trapping region. For the long-short kick sequence this state projects onto essentially a single Floquet state at $t=0$, and so its time evolution is trivial and its energy remains constant. For the case of the short-long kick sequence, however, the initial state projects onto a number of Floquet states [Eq. (3.2)], giving rise to a complicated quasiperiodic behavior arising from beating between the different quasienergies.

In Fig. 7(b), we see the effect of increasing the kick strength. In this regime we find there is an almost constant localization length for momenta in between the trapping regions, which are again signaled by sharp cusplike structures. This indicates that the Floquet states are confined between the classical broken phase barriers in the trapping regions. Early studies indicate that the level statistics of the corresponding quasienergies are not pure Poisson in this regime, as would be the case for the standard QKR.

In Fig. 7(c), we see an inversion of the broad momentum modulation in Fig. 7(a), similar to the reversal seen in the experiment. In this regime, the eigenstates localized in the trapping regions near $p\simeq(2n+1)\pi/\epsilon$ are typically *broader* than those localized in between.

V. CONCLUSIONS

We have presented a study of the Floquet states of δ-kicked particles pulsed with unequal periods, and used them to analyze experimental data on these systems. We conclude that the chaotic ratchet effect proposed in [7] and observed experimentally in [9] is associated with asymmetric Floquet states localized around $p=0$. We conclude also that the behavior of the localization lengths of the Floquet states for the double δ-kicked rotor broadly accompany the transitions between the three distinct classical diffusion regimes investigated experimentally in [11].

ACKNOWLEDGMENTS

We would like to thank Mischa Stocklin for useful discussions, and the EPSRC for financial support.

[1] G. Casati, B. V. Chirikov, F. M. Izraelev, and J. Ford, in *Stochastic Behavior in Classical and Quantum Hamiltonian Systems*, edited by G. Casati and J. Ford, Lecture Notes in Physics Vol. 93 (Springer, Berlin, 1979), p. 334; B. V. Chirikov, Phys. Rep. **52**, 263 (1979).

[2] S. Fishman, D. R. Grempel, and R. E. Prange, Phys. Rev. Lett. **49**, 509 (1982).

[3] F. L. Moore, J. C. Robinson, C. F. Bharucha, Bala Sundaram, and M. G. Raizen, Phys. Rev. Lett. **75**, 4598 (1995).

[4] D. A. Steck, W. H. Oskay, and M. G. Raizen, Phys. Rev. Lett. **88**, 120406 (2002).

[5] W. K. Hensinger, H. Häffner, A. Browaeys, N. R. Heckenberg, K. Helmerson, C. McKenzie, G. J. Milburn, W. D. Phillips, S. L. Rolston, H. Rubinsztein-Dunlop, and B. Upcroft, Nature (London) **412**, 52 (2001).

[6] F. M. Izraelev, Phys. Rep. **196**, 299 (1990).

[7] T. S. Monteiro, P. A. Dando, N. A. C. Hutchings, and M. R. Isherwood, Phys. Rev. Lett. **89**, 194102 (2002).

[8] T. Jonckheere, M. R. Isherwood, and T. S. Monteiro, Phys. Rev. Lett. **91**, 253003 (2003).

[9] P. H. Jones, M. Goonasekera, H. E. Saunders-Singer, and D. R. Meacher, quant-phys/0309149.

[10] P. H. Jones, M. Goonasekera, H. E. Saunders-Singer, T. S. Monteiro, and D. R. Meacher, physics/0504096.

[11] P. H. Jones, M. M. Stocklin, G. Hur, and T. S. Monteiro, Phys. Rev. Lett. **93**, 223002 (2004);M. Stocklin, G. Hur, and T. S. Monteiro, physics/0408088.

[12] T. Dittrich, R. Ketzmerick, M.-F. Otto, and H. Schanz, Ann. Phys. (Leipzig) **9**, 1 (2000); H. Schanz, M.-F. Otto, R. Ketzmerick, and T. Dittrich, Phys. Rev. Lett. **87**, 070601 (2001).

[13] S. Flach, O. Yevtushenko, and Y. Zolotaryuk, Phys. Rev. Lett. **84**, 2358 (2000).

[14] P. Reimann, Phys. Rep. **361**, 57 (2002).

[15] D. Ł. Shepelyansky Phys. Rev. Lett. **56**, 677 (1986).

[16] B. G. Klappauf, W. H. Oskay, D. A. Steck, and M. G. Raizen, Phys. Rev. Lett. **81**, 1203 (1998).

[17] J. Ringot, P. Szriftgiser, J. C. Garreau, and D. Delande, Phys. Rev. Lett. **85**, 2741 (2000).

[18] C. E. Creffield, Europhys. Lett. **66**, 631 (2004).

Localization-delocalization transition in a system of quantum kicked rotors

C.E. Creffield, G. Hur and T.S. Monteiro
Department of Physics and Astronomy, University College London, Gower Street, London WC1E 6BT, United Kingdom
(Dated: December 7, 2005)

The quantum dynamics of atoms subjected to pairs of closely-spaced δ-kicks from optical potentials are shown to be quite different from the well-known paradigm of quantum chaos, the single δ-kick system. We find the unitary matrix has a new oscillating band structure corresponding to a cellular structure of phase-space and observe a spectral signature of a localization-delocalization transition from one cell to several. We find that the eigenstates have localization lengths which scale with a fractional power $L \sim \hbar^{-.75}$ and obtain a regime of near-linear spectral variances which approximate the 'critical statistics' relation $\Sigma_2(L) \simeq \chi L \approx \frac{1}{2}(1-\nu)L$, where $\nu \approx 0.75$ is related to the fractal classical phase-space structure. The origin of the $\nu \approx 0.75$ exponent is analyzed.

PACS numbers: 05.45.Mt, 05.60.-k, 72.15Rn, 32.80.Pj

The δ-kicked quantum rotor (QKR) is one of the most studied paradigms of quantum chaos. Its implementation using cold atoms in optical lattices [1] provided a convincing demonstration of a range of quantum chaos phenomena including Dynamical Localization [2], the quantum suppression of chaotic diffusion. Recently, an experimental study [3] of cesium atoms subjected to *pairs* of δ-kicks (2δ-KR) showed surprisingly different behavior. The classical phase-space is chaotic but is made up fast diffusing regions which are partly separated by slow-diffusing 'trapping regions', where the classical trajectories stick; the classical analysis revealed a regime of anomalous diffusion corresponding to long-lived correlations between kicks.

Further details are given in [4] but we show here that the 2δ-KR has some unexpected *quantum* properties. We show that there is a cellular phase-space structure which arises from a novel oscillatory band structure of the corresponding unitary matrix. One consequence is a new type of localization-delocalization transition not seen in the QKR, where states delocalize from single to multiple-cell occupancy; we show it has a clear spectral signature. We have also found scaling behavior of the localization lengths associated with a *fractional* exponent, i.e. $L \sim \hbar^{-0.75}$, whereas for the well-studied QKR, $L \sim \hbar^{-1}$. A similar exponent is found for the decay of return probabilities in the trapping regions, $P(t) \sim t^{-0.75}$. We argue that the exponent 0.75 corresponds closely to the value obtained for the dominant exponent of the golden ratio cantorus [5, 6]. We show that the spectral fluctuations (both the nearest-neighbor statistics (NNS) and spectral variances) show important differences with the QKR in regimes where the delocalization of eigenstates is hindered by cantori bordering the cells. We find a regime approximating the form found in 'critical statistics': the number variances of the spectra are linear $\Sigma_2(L) \simeq \chi L$ for $L \gg 1$, where $\chi \simeq 1/2(1-\nu) < 1$ and $\nu \simeq 0.75$.

The term 'critical statistics' arose originally in relation to the Metal Insulator Transition (MIT) in systems with disorder [7, 8]. A new universal form of the distribution of nearest-neighbor eigenvalue spacings, termed 'semi-Poisson', $P(s) \sim s\exp -2s$ was associated with the MIT [7]. For critical statistics a very interesting connection has been established between the multifractal characteristics of the wavefunctions and those of the spectral fluctuations [8]: the number variances of the spectra are linear $\Sigma_2(L) \simeq \chi L$ for $L \gg 1$. The slope, $\chi \simeq 1/2(1 - D_2/D) < 1$, was shown to be related to a fractal dimension D_2 obtained from the second moment of the wavefunction and to D, the spatial dimension of the system. For integrable dynamics, in contrast, $\Sigma_2(L) = L$ while for a GOE, $\Sigma_2(L) \sim Ln(L)$. There is much current interest in so-called 'critical' statistics in non-KAM billiards (typically systems where the dynamics would be integrable were it not for a discontinuity in the potential) [9], which show multifractal scalings and linear variances related to D_2. Below we apply the term 'critical statistics' in this broader sense, rather than the MIT critical point. Multifractal behavior has been demonstrated for Cantor spectra [10] where the level density itself is not smooth. However, until now, critical statistics have not been seen – and were not thought to be relevant to – KAM systems. These are systems, ubiquitous in many areas of physics, where the transition to chaos as a perturbing parameter is increased is quite gradual.

The Hamiltonian of the 2δ-KR is $H(x,p) = \frac{p^2}{2} + K\cos x \sum_n \delta(t-nT) + \delta(t-nT+\epsilon)$; there is a short time interval ϵ between the kicks in each pair and a much longer time $\simeq T$ between the pairs themselves. In experiments $\epsilon \sim 0.01 - 0.1 \ll T$ and $\hbar \simeq 2 - 1/4$ in the usual re-scaled units [3].

A study of the spectral fluctuations of a time-periodic system involves a study of the eigenstates and eigenvalues of the one-period time-evolution operator $U(T,0)$. For the QKR, the matrix representation, in an angular momentum basis $|\, l\rangle$, has elements $U_{lm} = U_l^{free}.\, U_{lm}^{kick} = \exp -il^2T\hbar/2\,.\, J_{l-m}(\frac{K}{\hbar})$. The 'kick' terms, $J_{l-m}(\frac{K}{\hbar})$ are

Bessel functions and give the matrix the banded form illustrated in Fig.1(a). Since $J_{l-m}(x) \simeq 0$ if $|l-m| > x$ we define the usual bandwidth $b = K/\hbar$. The resulting statistics are approximated by those of Band Random Matrix Theory (BRMT) [11] rather than of RMT: i.e. if the dimension of the $U(T,0)$ matrix is N_{tot}, the statistics are *Poissonian* for $N_{tot} \gg b$; the eigenstates of the BRM are exponentially localized in l, with a localization length in momentum ($p = l\hbar$) which equals $L_p \sim K^2/\hbar$, so states separated in p by $\gg L_p$ will be largely uncorrelated.

For the 2δ-KR, the corresponding matrix elements are:

$$U_{lm} = e^{-il^2(T-\epsilon)\hbar/2} \cdot \sum_k J_{l-k}\left(\frac{K}{\hbar}\right) J_{k-m}\left(\frac{K}{\hbar}\right) e^{-i\frac{k^2}{2}\hbar\epsilon}. \tag{1}$$

As the $U(T,0)$ matrix is quite insensitive to $(T-\epsilon)$ the quantum dynamics largely depends only on two scaled parameters $K_\epsilon = K\epsilon$ and $\hbar_\epsilon = \hbar\epsilon$, rather than on K, ϵ and $\hbar$ independently: the remainder of the matrix is invariant if K_ϵ and $\hbar_\epsilon$ are kept constant.

An analytical form for the bandwidth of $U(T,0)$ was obtained in [4]: the bandwidth oscillates sinusoidally between a maximum value $b_{max} = 2K/\hbar$ for angular momenta $l \simeq 2n\pi/(\hbar\epsilon)$ and a minimum value $b_{min} \approx 0$ for $l \simeq (2n+1)\pi/(\hbar\epsilon)$. These minima correspond to the trapping momenta $p = l\hbar \simeq (2n+1)\pi/\epsilon$ seen in experiment. The corresponding band-structure of U is illustrated in Fig.1(b): the band oscillates, and U is approximately partitioned into sub-matrices of dimension $N = \frac{2\pi}{\epsilon\hbar}$ corresponding to separate momentum cells.

The key to our work is our ability to vary the *transport* between the cells (by opening/closing the classical fractal 'gates' between them) separately from the degree of *filling* of each individual cell. We begin by introducing a 'filling factor' R where

$$R = \frac{K^2}{N\hbar^2} = \frac{K_\epsilon^2}{2\pi\hbar_\epsilon} \tag{2}$$

measures the degree of filling of a cell by a typical state in the absence of confinement. Clearly, if there is no transport between cells the states simply fill the cell uniformly

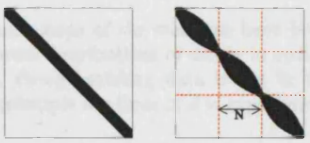

FIG. 1: Left: Structure of time-evolution matrix $U(T,0)$, for the Quantum Kicked Rotor (QKR), in a basis of momentum states, exemplifying the typical band-structure of a Band Random Matrix (BRM). Right: $U(T,0)$ for our system, the 2δ-KR, showing the new form with oscillating bandwidth. Before delocalization, eigenstates are confined within a single 'momentum cell' of dimension N.

and even if $R \gg 1$, the localization lengths $L_p \sim N\hbar$. We begin by defining a *localized* limit, where $R \ll 1$ and $L_p \ll N\hbar \sim \frac{2\pi}{\epsilon}$; typical states are insensitive to the boundary conditions of the cell and this limit is Poissonian. At the other extreme, if we allow strong coupling between cells, we move to an opposite limit as an increasing proportion of eigenstates become delocalized over several cells.

We now investigate the transport. A classical analysis [4, 12] shows that if we take $K\epsilon \ll 1$ and expand initial momenta of the $j-th$ trajectory about the trapping values $p_j = (2n+1)\pi/\epsilon + \delta p_j$, we can show that much of the trapping region is given by a classical map quite similar to the well-known Standard Map:

$$p_{j+2} \simeq p_j - K^2\frac{\epsilon}{2}\sin 2x_j - K\delta p^j\,\epsilon\cos x_j \tag{3}$$

$$x_{j+2} \simeq x_j + p_{j+2}T. \tag{4}$$

Over much of the trapping region, the second term in Eq.3 is dominant, for parameter regimes of interest. Then the kick impulse has a $\pi/2$ phase relative to the full map (the 2-kick map gives a pair of $V'(x) = -\sin x$ type impulses) and a momentum dependent effective kick strength $K' = K\epsilon\delta p_j$. A detailed study of classical phase-space [12] shows that at low K' the resonance structure is locally quite similar to the Standard Map. Hence, in the regime $K\epsilon\delta p_j \sim 1$ we expect the 'golden ratio' cantori, which result from the last invariant manifold of a KAM system, to provide the strongest barrier to transport [13]. Though we want $K\epsilon$ to be small, if $K\epsilon < 0.1$ phase space becomes too regular. Hence here we find that the regime of interest is within the interval $0.1 \leq K_\epsilon \leq 0.7$.

We investigated the corresponding quantum transport by evolving a set of wavepackets $\Phi(p,t)$ in time, (where $\Phi(p,t=0) = \delta(p)$) for a range of K_ϵ and $\hbar_\epsilon$, until the momentum spreading is arrested by dynamical localization at $t \simeq t_H$. The resulting probability distributions $|\Phi(p, t \gg t_H)|^2 = N(p)$ have a characteristic 'staircase' structure, shown in Fig.2(a). At each step there is a steep drop in probability:

$$N(p)_+ = e^{-2d}N(p)_- \tag{5}$$

(where $N(p)_\pm$ represent probabilities before(-) and after(+) the step) concentrated over the trapping region ($\sim 1/6$ of a cell in every case [4]). The staircase tracks an exponential envelope $N(p) \sim \exp -2|p|/L_{exp}$, where $L_{exp} = \frac{\pi}{\epsilon d}$. We average over several steps, to obtain d as a function of K_ϵ and $\hbar_\epsilon$. In Fig.2(b) we show that, quite accurately, $d \propto \hbar_\epsilon^{0.75}/f(K_\epsilon)$ where $f(K_\epsilon)$ is some function of the scaled kick-strength, K_ϵ. We estimate

$$d \approx \frac{3.5\hbar_\epsilon^{0.75}}{K_\epsilon^3}. \tag{6}$$

The parameter d (defined by Eq.5) quantifies the transport between the cells and complements the filling factor

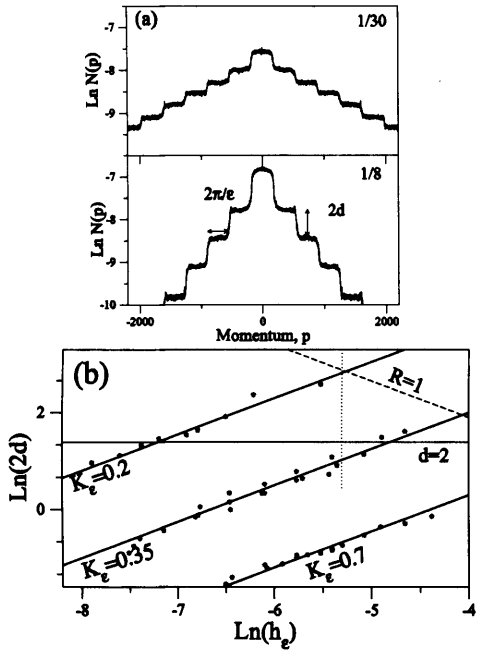

FIG. 2: **(a)** Final ($t \to \infty$) momentum distributions, $N(p)$, (slightly smoothed) for quantum wavepackets of the 2δ-QKR for $K = 20$, $\epsilon = 0.0175$ and $\hbar = 1/8$ and $1/30$ respectively. $N(p)$ for both the eigenstates and wavepackets shows a long-range 'staircase' form which on average follows the exponential $N(p) \sim \exp -2(p-\bar{p})/L_{exp}$ where $L_{exp}/2 = 2\pi/\hbar\epsilon$; the $\hbar$-dependence of L_{exp} is determined by the drop in probability, d, at each step. **(b)** shows that $Ln(2d)$ plotted against $Ln(\hbar\epsilon)$ lies on straight lines of invariant $K_\epsilon = K\epsilon$, with constant slope 0.75. Hence $d \propto (\hbar\epsilon)^{0.75}$ and $L_{exp} \propto \hbar^{-0.75}$ – in contrast to the well-known QKR result $L_{exp} \propto \hbar^{-1}$. The $R = 1$ border is shown: for $R > 1$ (below the line) eigenstates fill much of a single cell. The *delocalization* border is shown at $d \simeq 2$: for $d > 2$ (above the line), over 98% of the probability of typical eigenstates is confined to a single cell; for $d < 2$, eigenstates begin to occupy multiple cells. Statistics are presented later in Fig.3 for points corresponding to the dotted line.

R. The inner steps of the staircase have been seen in the momentum distributions of atoms in optical lattices [3, 14]; so, though existing data is not in the critical regime, in principle the form of d is experimentally verifiable.

We are unaware of another KAM system where a single power-law exponent is so dominant. Typically, power-law behavior is associated with mixed phase space behavior, where many competing exponents are found [10]. We note also that the value 0.75 coincides closely with one of the scaling exponents found in [5] for the golden ratio cantori: these were $\sigma \approx 0.65$ (in the most unstable part of the cantori) and $\sigma \approx 0.76$ (most stable regions). There have been previous studies of transport in a region near golden ratio cantori. These have found $L \sim \hbar^{+0.66}$ [15] but only in a momentum band region 'local' to the cantori. We note that the $L \sim \hbar^{+\sigma}$ dependence is associated with the physical process termed 'retunnelling' [6] associated with cantori which are classically 'open' but for which $\hbar$ is too large to permit free quantum transport. An abrupt change to an $L \sim \hbar^{-\sigma}$ is observed when the cantori 'open' for quantum transport and L is determined instead by localization. It has been argued that the reason all previous studies have found $L \sim \hbar^{+0.66}$ [6] is that the retunnelling transport favors the unstable direction. To our knowledge ours is the only example corresponding to the dominant exponent of the golden ratio cantori; we attribute this to the fact that we are always in a dynamical localization regime, and localization will select the most stable parts of the fractal cantori regions, where at low K, elliptic fixed points are found.

We can now investigate the statistics as a function of the filling factor R and the inter-cell transport parameter d. Full details are given in [4], but in brief: we considered two types of boundary conditions (BCs). (1) Periodic BCs, i.e. solving the problem on a 'torus' in momentum space, a well-known procedure for the QKR [11]. (2) Open BCs, where we diagonalize $U(T,0)$ with $N_{tot} = 10,000$, but $N \approx 1000$; we then assigned the $i-th$ eigenstate to the $n-th$ cell if $(2n+1)\pi/\epsilon \leq \langle p_i \rangle \leq (2n+3)\pi/\epsilon$ and calculated statistics for each cell. In both cases we averaged over ≈ 20 cells to improve significance. For periodic BCs, eigenstates cannot escape from a single cell of width $N\hbar$. For open BCs, however, they can delocalize onto neighboring cells.

In Fig.3(a), the $\Sigma_2(L)$ statistics are presented. These represent the variances in the spectral number density, $\Sigma_2(L) = \langle L^2 \rangle - \langle L \rangle^2$, where we consider a stretch of the spectrum with an average $\langle L \rangle$ levels. A fit to the best straight line in the range $L \simeq 5 - 40$ yields an estimate of the slope χ. In Fig.3(b) we show the nearest neighbor $P(S)$ statistics. We quantify the deviation of $P(S)$ from $P_P(S)$ and $P_{GOE}(S)$, its Poisson and GOE limits respectively, with a parameter Q [16]:

$$1 - Q = \frac{\int_0^{S_0} (P(S') - P_{GOE}(S')dS')}{\int_0^{S_0} (P_P(S') - P_{GOE}(S'))dS'}. \qquad (7)$$

Hence $Q = 0$ indicates a Poisson distribution, while $Q = 1$ signals a GOE distribution. We take $S_0 = 0.3$.

The results of Fig.3 demonstrate that the statistics are not too sensitive to boundary conditions for $d > 2$ (see also [4]). However, for $d \leq 2$, while the states with periodic BCs (effectively restricted to a matrix of dimension N) move gradually to the GOE limit, for the open BCs, at delocalization the statistics tend back to the Poisson limit. This initially surprising behavior occurs because, after delocalization, one finds increasing numbers

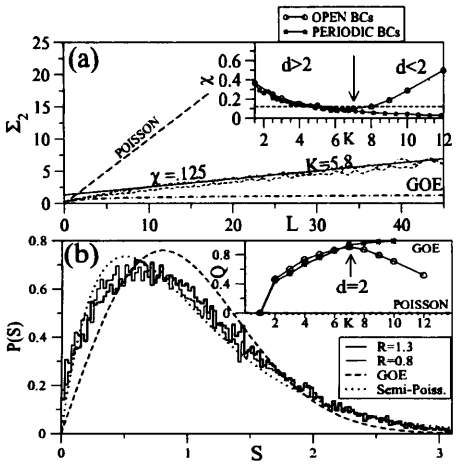

FIG. 3: (a) shows the $\Sigma_2(L)$ statistics for the $2\delta - KR$. Approximately linear variances, with slope $\chi \approx 0.125$ are found in the intermediate regime. Solid line indicates the line $\Sigma_2(L) = 0.125L + c$ corresponding to the 'critical statistics' slope $\chi \approx 1/2(1-\nu)$ where $\nu \simeq 0.75$ is the fractional exponent obtained previously. (b) shows corresponding nearest neighbor statistics for $R = 0.8$ and $R = 1.3$ of an intermediate form, which is compared with the Semi-Poisson and GOE forms. The insets show the effect of the boundary conditions. Before delocalization ($d > 2$) the results are insensitive to boundary conditions. If $d < 2$, for periodic BCs (points indicated by asterisks) the statistics make a transition to GOE; for open BCs (points indicated by circles), the statistics tend to Poissonian behavior. The arrows indicate the $d = 2$ border.

of states for which $\langle p_i \rangle$ assigns them to the $n-th$ cell, but for which much of the state's probability is actually found in neighboring cells [4]. Hence states within each spectrum of N eigenvalues become progressively uncorrelated. This apparent failure of the procedure of assigning states to a given cell, in fact provides a rather good 'marker' for the onset of delocalization, and yields a clear 'turning point' in both the NNS and $\Sigma_2(L)$ behavior. A detailed study of the multi-cell regime remains to be undertaken; models of the statistics for chaotic systems with non-uniform rate of exploration of phase-space [17] may be relevant here.

Of further interest here is an intermediate regime, found for both boundary conditions for $R \approx 1$ and $d > 2$. Over a wide range of parameters and different cell sizes [4], we find approximately linear variances, for $L \gg 1$ and $L \ll N$, with slope $\chi \approx 0.125$. The inset of Fig.3(a) plots the values of χ calculated along the vertical dotted line of Fig2(b) for periodic and open boundary conditions. We note that a study of the decay of return probabilities obtained $P(t) = |\langle \psi(t=0)|\psi(t)|\rangle|^2 \sim t^{-0.75}$ for wavepackets started in the trapping regions (see [4]). The value of $\chi \approx 0.125$ corresponds to the value which would be obtained from the MIT relation, $\chi \approx 1/2(1-D_2)$ if $D_2 \approx 0.75$; in the MIT, return probabilities with $P(t) \sim t^{-D_2}$ were similarly found. We suggest that this represents a KAM analogue of behavior associated with 'critical statistics'.

In summary, we have shown that the behavior of the 2δ-kicked system is rather different from the standard QKR. We have identified a spectral signature of the novel localization-delocalization transition that the system exhibits. We have also identified signatures of the fractal phase-space structure of the cell borders. The trapping regions may have applications in atom optics experiments, as a means of manipulating the momentum distribution of the atomic cloud.

This work was supported by the EPSRC. We thank Shmuel Fishman and Antonio Garcia-Garcia for helpful comments and advice.

[1] F.L. Moore, J.C. Robinson, C.F. Bharucha, B. Sundaram, M.G. Raizen, Phys. Rev. Lett. **75**, 4598 (1995).
[2] G. Casati, B.V. Chirikov, F.M. Izraelev, J. Ford, in "Lecture notes in Physics", Springer, Berlin, **93** , 334 (1979); S. Fishman, D.R. Grempel, R.E. Prange, Phys. Rev. Lett. **49**, 509 (1982).
[3] P.H. Jones, M.M. Stocklin, G. Hur, T.S. Monteiro, Phys. Rev. Lett. **93**,223002 (2004).
[4] C.E. Creffield, S. Fishman, T.S. Monteiro, physics/0510161.
[5] S. Fishman, D.R. Grempel, R.E. Prange, Phys. Rev. A.**36**, 289 (1987).
[6] N.T. Maitra and E. J. Heller, Phys. Rev. E.**61**, 3620 (2000).
[7] B.I. Shklovskii et al, Phys. Rev. B.**47**, 11487 (1993)
[8] J.T. Chalker, I.V. Lerner, R.A. Smith, Phys. Rev. Lett. **77**, 554 (1996); V.E. Kravtsov and K.A. Muttalib, Phys. Rev. Lett. **79**, 1913 (1997); D. Braun, G. Montambaux and M. Pascaud, Phys. Rev. Lett.**81**, 1062 (1998) F. Evers and A.D. Mirlin, Phys. Rev. Lett.**84**, 3690 (2000).
[9] E.B. Bogomolny, U. Gerland and C. Schmit, Phys. Rev. E.**59**, R1315 (1999); A.M. Garcia-Garcia and J.J.M. Verbaarschot, Phys. Rev. E.**67**, 046104 (2003); E. Bogomolny and C. Schmit, Phys. Rev. Lett. **92**, 244102 (2004). A.M. Garcia-Garcia and J. Wang, Phys. Rev. Lett. **94**, 244102 (2005).
[10] R. Ketzmerick, G. Petschel, T. Geisel, Phys. Rev. Lett.**69**, 695 (1992).
[11] M. Feingold et al, Phys. Rev. B **31**, R6852 (1985); F.M. Izraelev, Phys. Rep. **196**, 299 (1990).
[12] M. Stocklin, PhD. thesis in preparation.
[13] E. Ott, 'Chaos in dynamical systems', Cambridge University Press (1993).
[14] K. Vant, G. Ball, H. Ammann, N. Christensen. Phys. Rev. E **59**, 2846 (1999).
[15] T. Geisel, G. Radons and J. Rubner, Phys. Rev. Lett.**57**, 2883 (1986).

[16] C. Mejia-Monasterio, G. Benenti, G.G. Carlo, and G. Casati, quant-ph/0410246 (2004).
[17] O. Bohigas, S. Tomsovic, D. Ullmo, Phys. Rep. **232**, 43 (1993).